A Search for Sterile Neutrinos at the NOνA Far Detector

A DISSERTATION PRESENTED
BY
GARETH KAFKA
TO
THE DEPARTMENT OF PHYSICS

IN PARTIAL FULFILLMENT OF THE REQUIREMENTS
FOR THE DEGREE OF
DOCTOR OF PHILOSOPHY
IN THE SUBJECT OF
PHYSICS

HARVARD UNIVERSITY
CAMBRIDGE, MASSACHUSETTS
MAY 2016

Thesis advisor: Professor Gary Feldman Gareth Kafka

A Search for Sterile Neutrinos at the NOνA Far Detector

Abstract

NOνA is the current United States flagship long-baseline neutrino experiment designed to study the properties of neutrino oscillations. It consists of two functionally identical detectors each located 14.6 mrad off the central axis from the Fermilab NuMI neutrino beam. The Near Detector is located 1 km downstream from the beam source, and the Far Detector is located 810 km away in Ash River, Minnesota. This long baseline, combined with the ability of the NuMI facility to switch between nearly pure neutrino and anti-neutrino beams, allows NOνA to make precision measurements of neutrino mixing angles, potentially determine the neutrino mass hierarchy, and begin searching for CP violating effects in the lepton sector. However, NOνA can also probe more exotic scenarios, such as oscillations between the known active neutrinos and new sterile species.

This thesis showcases the first search for sterile neutrinos in a $3 + 1$ model at NOνA. The analysis presented searches for a deficit in the rate of neutral current events at the Far Detector using the Near Detector to constrain the predicted spectrum. The comparison between the observed and predicted spectra is translated into a measurement of the expanded PMNS mixing matrix elements, $|U_{\mu 4}|^2$ and $|U_{\tau 4}|^2$, assuming a value of $\Delta m^2_{41} \sim O(1\text{ eV}^2)$. This analysis was performed using data taken between February 2014 and May 2015 corresponding to 3.52×10^{20} protons on target. The best fit values for the matrix elements were $|U_{\mu 4}|^2 = 0.xy \pm a.bc$ and $|U_{\tau 4}|^2 = 0.vw \pm d.ef$, consistent with the no sterile neutrino hypothesis. At the end of this thesis there is a short discussion of future sensitivity improvements using a larger dataset.

Contents

List of Figures

List of Tables

This is the dedication.

Acknowledgments

These people were cool.

1

A Brief History of Neutrinos

1.1 Introduction

The neutrino was first postulated by Wolfgang Pauli as a possible explanation for the continuous spectrum of electrons emitted from nuclear β decay [1]. This decay was originally thought to be the emission of an electron from an atom, resulting in a different nucleus, via the process,

$$N \rightarrow N' + e \tag{1.1}$$

where N and N' are the parent and daughter nuclei, respectively. In a two body decay such as this, the momenta and energies of the outgoing particles are exactly constrained. Pauli's new particle explained the continuous spectrum of electron energy via a modified decay process:

$$N \rightarrow N' + e + \nu \tag{1.2}$$

where ν is the outgoing neutral particle. Pauli's original proposal called the new particle the neutron, but this name was later used to name the massive neutral nucleon discovered by Chadwick in 1932 [2]. Three years after Pauli's idea, Fermi proposed a model for nuclear β decay that included the new particle, which he coined the neutrino, or little neutral one [3].

1.2 First Detection of Neutrinos

Twenty years passed from Fermi's model proposal before neutrinos were discovered experimentally. Fred Reines and Clyde Cowan made the discovery by placing a detector near a nuclear reactor as a source of neutrinos and observing inverse β decay [4, 5]. The neutrinos observed were anti-electron neutrinos, thus the following was the observed process.

$$p + \bar{\nu}_e \rightarrow n + e^+ \tag{1.3}$$

Reines earned the Nobel Prize in Physics in 1995 for the detection of the neutrino.

In 1962, the muon neutrino was discovered at Brookhaven National Laboratory using the first neutrino beam [6] in a scheme still used in neutrino experiments today. The beam was generated by colliding protons with a target, producing pions that decayed into muons and muon neutrinos. The resultant beam then passed through thick steel, absorbing everything but the neutrinos. Leon Lederman, Melvin Schwartz, and Jack Steinberger won the Nobel Prize in Physics in 1988 for the discovery of the muon neutrino.

The last generation of neutrino, the tau neutrino, was discovered at Fermilab by the DONUT collaboration in 2000 [7].

1.3 Evidence of Neutrino Oscillations

Pontecorvo first postulated neutrino oscillations between neutrinos and anti-neutrinos, analogous to $K^0/\bar{K}^0$ oscillations, in 1957 [8]. Nothing came of the proposal immediately, but the idea was later revived and modified to solve the solar neutrino problem. The physics community initially viewed neutrino oscillations with skepticism and believed the experiments to be flawed, but over time oscillations have become an unmistakable and accepted phenomenon.

The solar neutrino problem was born from a large discrepancy between the theoretical and observed number of neutrinos produced by the sun. Neutrinos were used as a study for solar models because photons take a thousand years to escape the dense nuclear plasma to the surface of the sun, but neutrinos are unimpeded. The models, which have been confirmed today, describe a somewhat complicated chain of nuclear reactions, many of which produce neutrinos. Each individual process contributes a neutrinos in a different energy spectrum, but all of the neutrinos are created as electron neutrinos.

The experimental observations and theoretical predictions were both published in 1968. Ray Davis designed an experiment underground in the South Dakota Homestake mine consisting of a tank of an ultra pure chlorine cleaning solution capable of neutrino capture via the process

$$\nu_e + {}^{37}\mathrm{Cl} \rightarrow {}^{37}\mathrm{Ar} + e^- \tag{1.4}$$

The argon atoms could be collected and counted for a direct measurement of the neutrino flux [9]. Meanwhile, John Bahcall precisely calculated the expected neutrino flux [10], and the observed rate was found to be about one third of the predicted rate. Pontecorvo revived his theory with the modification of allowing ν_e to ν_μ oscillations [11], but the idea was still not taken seriously and it was another 20 years before the solar neutrino problem was confirmed.

Beginning in 1989, multiple experiments with different methodologies confirmed the solar neutrino problem. Kamiokande, a water Cherenkov detector, measured a rate deficit in 1989 [12]. Two experiments measured solar neutrinos via the reaction

$$\nu_e + {}^{71}\mathrm{Ga} \rightarrow {}^{71}\mathrm{Ge} + e^- \tag{1.5}$$

and measured a similar deficit, SAGE in 1991 [13] and GALLEX in 1992 [14]. With results from three different experimental methods all showing similar rate deficits, the solar neutrino problem could no longer be relegated to an experimental error.

Evidence soon emerged for oscillations with atmospheric neutrinos as well. These neutrinos are produced when cosmic rays collide with particles in the atmosphere and decay, predominantly via the following channels.

$$\begin{aligned} \pi^{+/-} &\rightarrow \mu^{+/-} + \nu_\mu/\bar{\nu}_\mu \\ \mu^{+/-} &\rightarrow e^{+/-} + \nu_e/\bar{\nu}_e + \bar{\nu}_\mu/\nu_\mu \end{aligned} \tag{1.6}$$

Thus, the expected ratio of muon family neutrinos to muon family neutrinos was expected to be 2. Kamiokande measured this ratio in 1992 and found the ratio to be much closer to 1 [15]. Furthermore, the ratio seemed to be dependent on zenith angle, with the measurement being nearly 2 for neutrinos coming from directly overhead, and dropping as the angle increased. Super-Kamiokande (or Super-K), the successor to Kamiokande, improved upon this measurement in 1998 [16], providing the most definitive evidence of neutrino oscillations to that point.

A resolution to the solar neutrino problem did not have to wait much longer with detector technologies capable of discerning different neutrino interaction types. SNO was designed as a heavy water (D_2O) Cherenkov detector experiment to be sensitive to both the flux of electron neutrinos and the flux of all neutrinos. In 2002, it released results for these measurements, finding what was then the expected deficit in electron neutrino flux, but a total flux consistent with the standard solar model, see figure1.1 [17]. With this result, neutrino oscillations were confirmed, and subsequent experiments now measure oscillation parameters with precision.

1.4 Possible Evidence of Sterile Neutrinos

Several experiments have reported results that can be explained by oscillations between more than three neutrinos. The frequency of oscillations is controlled by the mass splitting between neutrino mass states, Δm^2, and will be considered in more detail in chapter 2. Historically, solar and atmospheric neutrino oscillations were discovered first and were well explained by oscillations between the standard model's three active neutrinos, and with three neutrinos, there are only two independent mass splittings. Fur-

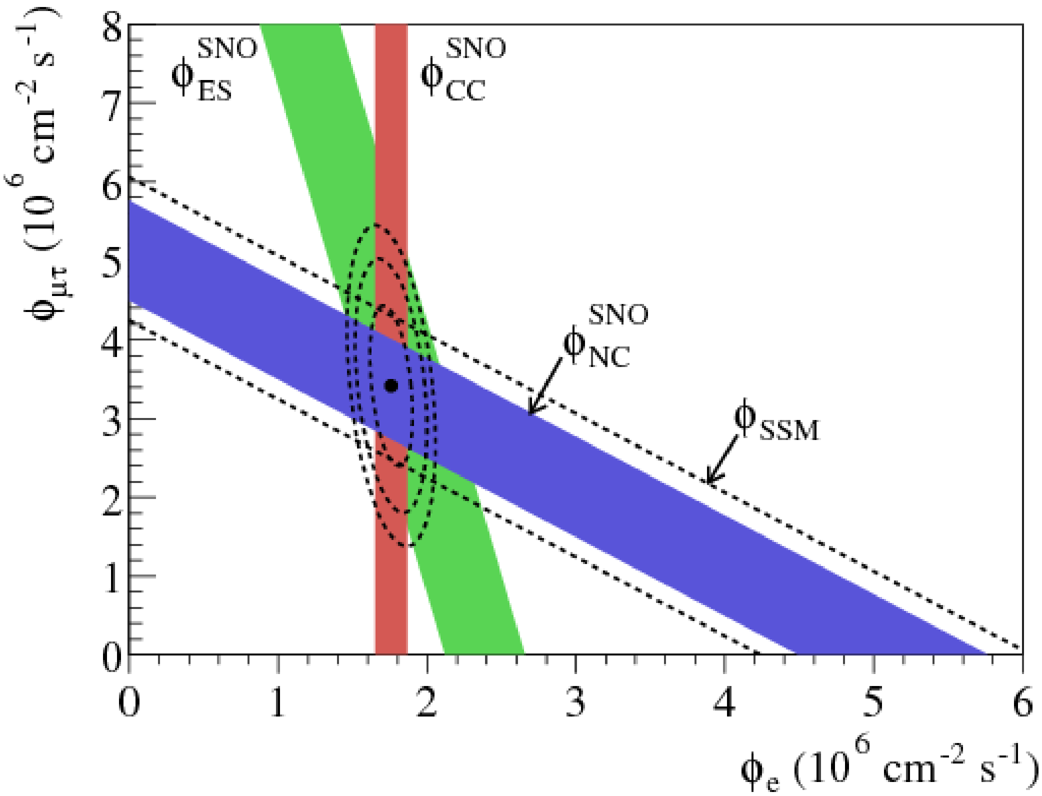

Figure 1.1: The measurement of different event rates at SNO [17]. The red band represents ν_e CC interactions with the deuterium neutron, an interaction only sensitive to electron neutrinos. The blue band represents neutral current scattering off of the deuterium nucleus, an interaction sensitive to the total neutrino flux. The green band represents elastic scattering of the neutrino off the deuterium electron, an interaction sensitive to all neutrino flavors, but not completely independent of neutrino flavor. The dashed straight lines represent the flux prediction by the standard solar model. The point represents the best fit for the flux of electron neutrinos and the flux for the combined muon and tau neutrinos.

thermore, it is known that there can only be three active neutrinos. However, there have been some experimental results that cannot be explained by oscillations based on the solar and atmospheric mass splitting scales, but they can be explained by oscillations based on a third independent mass splitting.

The number of active neutrinos is constrained by measurements of the width of the Z boson. LEP has measured the number of active neutrinos to be 2.984 ± 0.008 [18], so the discoveries of the ν_e, ν_μ, and ν_τ leave no room for new active neutrinos. Strictly speaking, there could be other active neutrinos if they had mass greater than half the mass of the Z boson so the Z could not decay to them, but while current evidence hinting at a sterile neutrino would suggest a mass splitting much larger than the solar and atmospheric scales, it is still much smaller than the mass of the Z.

The first evidence for an additional neutrino came from the Liquid Scintillator Neutrino Detector, or LSND, in 1995. This experiment searched for $\bar{\nu}_e$ appearance in a $\bar{\nu}_\mu$ beam. When it found an excess of events, it reported a measurement of a mass splitting between neutrino states Δm^2 of $O(1\ \mathrm{eV}^2)$ [19], a measurement incompatible with the mass splittings measured in both the atmospheric and solar oscillation experiments, suggesting the addition of at least one more neutrino. However, based on the result from LEP, this new neutrino cannot couple to the Z boson, hence the suggestion for a sterile neutrino.

Searches for sterile neutrinos can be categorized in one of three channels: $\overset{(-)}{\nu}_\mu \rightarrow \overset{(-)}{\nu}_e$ appearance, $\overset{(-)}{\nu}_e$ disappearance, and $\overset{(-)}{\nu}_\mu$ disappearance. The LSND result was from the appearance channel. The MiniBooNE experiment at Fermilab searched for both ν_e appearance in a ν_μ beam and $\bar{\nu}_e$ appearance in an $\bar{\nu}_\mu$ beam. While they first reported no event excess in 2007 [20], their more results show excesses in both modes [21] that could be consistent with some sterile neutrino models. Not all experiments have found evidence of sterile neutrinos, however. The most recent results from KARMEN in 2002 [22] and NOMAD in 2003 [23], both measuring the appearance channel, showed no evidence of oscillations at the same mass scale as LSND.

Experiments measuring the $\overset{(-)}{\nu}_e$ disappearance channel have also reported some indication for a neutrino at the same mass scale as the appearance channel. The so-called Gallium anomaly comes from a measured deficit of events in GALLEX [24] and Sage [25] when placing a radioactive source inside the detectors for detector response measurements. On the other hand, reactor experiments such as Bugey [26] reported no oscillations and RENO [27] and Daya Bay [28] reported only oscillations consistent with standard three flavor oscillations. Furthermore, T2K, an accelerator experiment not unlike NOνA, performed a short baseline analysis at its Near Detector and also found no evidence of sterile oscillations at 95% confidence.

To date, experiments probing the $\overset{(-)}{\nu}_\mu$ disappearance channel have universally shown no evidence of sterile neutrinos. This includes an atmospheric neutrino measurement by Super-K [29] and a long baseline analysis by MINOS [30]. This list of experimental evidence for sterile neutrinos (or lack thereof) is not intended to be exhaustive, but it should be clear that there is not yet a scientific consensus on the existence of sterile oscillations despite the variety of past and current searches.

NOνA is a long baseline neutrino experiment with a near detector, thus capable of performing both short baseline and long baseline sterile neutrino analyses; this dissertation focuses on the long baseline. It measures events generated by the NuMI beam, a mostly pure ν_μ beam, and thus measures the ν_μ disappearance channel. (In the future, the beam will switch to $\bar{\nu}_\mu$ allowing for measurement in the $\bar{\nu}_\mu$ disappearance channel.) The analysis presented here searches for a deficit in the number of neutral current events at the far detector, using the near detector data to constrain the predicted spectrum. Neutral currents are insensitive to the flavors of the standard 3 active neutrinos, so a rate deficit would point to the existence of oscillations between active and sterile neutrinos.

2

Theory of Neutrino Oscillations

The idea of neutrino oscillations was first proposed by Pontecorvo in 1957 [8], but his proposal described oscillations between neutrinos and anti-neutrinos. In 1962, after the discovery of the muon neutrino, Maki, Nakagawa, and Sakata proposed the theory that described oscillations between neutrino flavors due to differing neutrino flavor and mass eigenstates [31]. This chapter describes the modern formalism in detail and uses natural units where $\hbar = c = 1$, except where otherwise noted.

2.1 The PMNS Matrix

In the Standard Model, neutrinos only interact via the W and Z bosons as shown by the Feynman diagrams in Fig. 2.1. From these diagrams, it is clear that neutrinos always interact in a definite flavor eigenstate, $|\nu_\alpha\rangle$. Furthermore, when a neutrino is produced from a W boson, the flavor is always determined

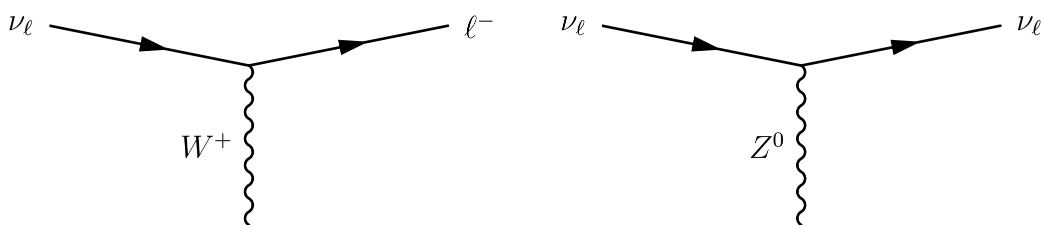

Figure 2.1: Standard Model Weak interactions involving a neutrino. Left: Charged current interaction. Right: Neutral current interaction.

by the associated charged lepton shown in eq. 2.1.

$$\begin{pmatrix} \nu_e \\ e \end{pmatrix}, \quad \begin{pmatrix} \nu_\mu \\ \mu \end{pmatrix}, \quad \begin{pmatrix} \nu_\tau \\ \tau \end{pmatrix} \tag{2.1}$$

On the other hand, neutrinos propagate through spacetime with a definite mass, $|\nu_i\rangle$ an eigenstate of the free Hamiltonian. The flavor states can be written as a superposition of the mass states via

$$|\nu_\alpha\rangle = \sum_{i=1}^{n} U_{\alpha i}^{*} |\nu_i\rangle , \tag{2.2}$$

where n is the number of neutrinos, and U is the unitary PMNS matrix, named after Pontecorvo, Maki, Nakagawa, and Sakata. The PMNS matrix is unitary, and would reduce to the identity matrix if neutrinos did not oscillate between flavor states. Yet since it does provide the mechanism for flavor transitions, it can be thought of as analogous to the quark sector CKM matrix.

2.2 Vacuum Oscillations

In this section, the basics of neutrino oscillations are developed by considering oscillations in a vacuum. The neutrinos are treated as plane waves, as in [32], with the assumption that the neutrino is actually localized in space put in by hand. A careful, rigorous analysis treating the neutrinos as plane waves in [33] reproduces the same results.

Consider a neutrino in a state of definite flavor α at time $t = 0$, $|\nu(0)\rangle = |\nu_\alpha\rangle$. This state is in a superposition of mass eigenstates. The time evolution of this neutrino is simply the time evolution of the individual mass states. In a vacuum, this adds a phase factor to each mass state.

$$|\nu_\alpha(t)\rangle = \sum_i U^*_{\alpha i} e^{-i(E_i t - \mathbf{p_i}\cdot\mathbf{x})} |\nu_i\rangle \tag{2.3}$$

With the neutrino at position $\mathbf{x} = L$ at time t, the dot product evaluates to $\mathbf{p_i} \cdot \mathbf{x} = p_i L$. Eq 2.3 can then simplified by making use of the fact that neutrinos are ultra-relativistic, allowing for several assumptions. First, the time, t, is replaced by the distance, L. Next, the energy of each mass state is approximated to be the same energy, $E_i = E$. Last, the momentum is expanded as $p_i = \sqrt{E^2 - m_i^2} \approx E - m_i^2/2E$. With these assumptions, eq. 2.3 simplifies as:

$$|\nu_\alpha(L)\rangle = \sum_i U^*_{\alpha i} e^{-im_i^2 L/2E} |\nu_i\rangle \, . \tag{2.4}$$

The mass eigenstate inside the sum is then re-expressed in terms of flavor eigenstates using the inverse of eq. 2.2 and unitarity of U.

$$|\nu_\alpha(L)\rangle = \sum_{\alpha'} \sum_i U^*_{\alpha i} U_{\alpha' i} e^{-im_i^2 L/2E} |\nu'_\alpha\rangle \, . \tag{2.5}$$

Eq. 2.5 can then be used to find the probability that the original neutrino in flavor state α has transitioned (or survived) as flavor state β. First, the matrix element $\langle\nu_\alpha|\nu_\beta(L)\rangle$ is computed.

$$\langle\nu_\alpha|\nu_\beta(L)\rangle = \sum_{\beta'} \sum_i U_{\beta' i} U^*_{\beta i} e^{-im_i^2 L/2E} \langle\nu_\alpha|\nu'_\beta\rangle = \sum_i U_{\alpha i} U^*_{\beta i} e^{-im_i^2 L/2E} \tag{2.6}$$

The last equality in eq. 2.6 follows from the orthogonality of individual flavor eigenstates. The probability of the flavor transition is then the square of this matrix element.

$$P(\nu_\alpha \to \nu_\beta) = |\left\langle \nu_\alpha | \nu_\beta(L) \right\rangle|^2 = \sum_{i,j} U_{\alpha i} U^*_{\beta i} U_{\beta j} U^*_{\alpha j} e^{-i(m_i^2 - m_j^2)L/2E} \tag{2.7}$$

It is standard to rewrite the mass squared difference as $\Delta m^2_{ij} \equiv m_i^2 - m_j^2$. Eq. 2.7 is then manipulated using the properties of unitary matrices.

$$\begin{aligned} P(\nu_\alpha \to \nu_\beta) &= \sum_{i,j} U_{\alpha i} U^*_{\beta i} U_{\beta j} U^*_{\alpha j} + \sum_{i,j} U_{\alpha i} U^*_{\beta i} U_{\beta j} U^*_{\alpha j} (e^{-i\Delta m^2_{ij} L/2E} - 1) \\ &= \delta_{\alpha\beta} + \sum_{i,j} U_{\alpha i} U^*_{\beta i} U_{\beta j} U^*_{\alpha j} (e^{-i\Delta m^2_{ij} L/2E} - 1) \end{aligned} \tag{2.8}$$

The remaining summed term is further simplified making use of two facts. When $i = j$, the complex phase is 0 as $\Delta m^2_{ii} = 0$, and thus these terms vanish. Second, the terms with $i < j$ are complex conjugates of those with $i > j$, and $z + z^* = 2\Re(z)$ for any complex number z.

$$P(\nu_\alpha \to \nu_\beta) = \delta_{\alpha\beta} + 2\sum_{i>j} \Re\left[U_{\alpha i} U^*_{\beta i} U_{\beta j} U^*_{\alpha j} (e^{-i\Delta m^2_{ij} L/2E} - 1)\right] \tag{2.9}$$

Both pieces of this term are split into their real and imaginary parts, and simplified using the trigonometric identity $\cos 2\theta - 1 = -2\sin^2\theta$. Defining $\mathcal{U} \equiv U_{\alpha i} U^*_{\beta i} U_{\beta j} U^*_{\alpha j} (e^{-i\Delta m^2_{ij} L/2E} - 1)$ and $\phi \equiv \Delta m^2_{ij} L/2E$:

$$\begin{aligned} \Re(\mathcal{U}) &= \Re\left[U_{\alpha i} U^*_{\beta i} U_{\beta j} U^*_{\alpha j} (e^{-i\Delta m^2_{ij} L/2E} - 1)\right] && (2.10) \\ &= \Re\left\{\left[\Re(U_{\alpha i} U^*_{\beta i} U_{\beta j} U^*_{\alpha j}) + i\Im(U_{\alpha i} U^*_{\beta i} U_{\beta j} U^*_{\alpha j})\right]\left[-2\sin^2(\phi/2) - i\sin\phi\right]\right\} && (2.11) \\ &= -2\Re(U_{\alpha i} U^*_{\beta i} U_{\beta j} U^*_{\alpha j})\sin^2(\phi/2) + \Im(U_{\alpha i} U^*_{\beta i} U_{\beta j} U^*_{\alpha j})\sin\phi && (2.12) \end{aligned}$$

Inserting the expression from eq. 2.12 into eq. 2.9, we find:

$$
\begin{aligned}
P(\nu_\alpha \to \nu_\beta) = \delta_{\alpha\beta} \quad &- \quad 4\sum_{i>j} \Re(U_{\alpha i}U^*_{\beta i}U_{\beta j}U^*_{\alpha j}) \sin^2 \Delta_{ij} \\
&+ \quad 2\sum_{i>j} \Im(U_{\alpha i}U^*_{\beta i}U_{\beta j}U^*_{\alpha j}) \sin 2\Delta_{ij},
\end{aligned} \tag{2.13}
$$

where $\Delta_{ij} \equiv \Delta m^2_{ij} L/4E = 1.267\Delta m^2_{ij} L\,(\text{km})/E\,(\text{GeV})$. It can now be seen that the distance the neutrino travels, its energy, and the different mass splittings all affect the frequency of oscillation. Ideally, neutrino oscillations would be studied by having neutrinos with a fixed energy profile (preferably monoenergetic) and varying the baseline. However, neutrino detectors are incredibly large, so in practice the baseline is fixed and the oscillation probability is studied as a function of neutrino energy.

For the case of survival probability, $\alpha = \beta$ and eq. 2.13 simplifies further. The imaginary piece from eq. 2.13 drops out, as

$$
\Im(U_{\alpha i}U^*_{\alpha i}U_{\alpha j}U^*_{\alpha j}) = \Im(|U_{\alpha i}|^2|U_{\alpha j}|^2) = 0. \tag{2.14}
$$

The survival probability is then given by:

$$
P(\nu_\alpha \to \nu_\alpha) = 1 - 4\sum_{i>j} |U_{\alpha i}|^2|U_{\alpha j}|^2 \sin^2 \Delta_{ij}. \tag{2.15}
$$

Due to the combined influence of mass splitting, oscillation baseline, and neutrino energy on the oscillation probability, it is often the case that only one term contributes to the sums in eq.s 2.13 and 2.15. The two neutrino approximation can be instructive in this instance. For this model, the mixing matrix simplifies to the two dimensional rotation matrix:

$$
U = \begin{pmatrix} \cos\theta & \sin\theta \\ -\sin\theta & \cos\theta \end{pmatrix}. \tag{2.16}
$$

As this matrix is entirely real, the imaginary piece of eq. 2.13 drops out. Plugging the matrix elements into the remaining term directly and simplifying slightly, we find the following forms for the survival and appearance probabilities.

$$
\begin{aligned}
P(\nu_\alpha \to \nu_\alpha) &= 1 - \sin^2 2\theta \sin^2\left(\frac{\Delta m^2 L}{4E}\right) &\quad (2.17)\\
P(\nu_\alpha \nrightarrow \nu_\alpha) &= \sin^2 2\theta \sin^2\left(\frac{\Delta m^2 L}{4E}\right) &\quad (2.18)
\end{aligned}
$$

From these equations it is clear that the mixing matrix parameters control the amplitude of neutrino oscillations. For small angles, most neutrinos will not change flavor, while larger angles can cause most of the neutrinos to change flavor. The case where $\theta = 45°$ is called maximal mixing as at specific baseline lengths the probability of oscillation becomes 1.

2.3 Standard 3-Flavor Oscillations

The Standard Model includes three neutrinos, so the PMNS matrix is 3×3 in this picture. Explicitly expanding eq. 2.2, U takes the following form:

$$
\begin{pmatrix} \nu_e \\ \nu_\mu \\ \nu_\tau \end{pmatrix} = \begin{pmatrix} U_{e1} & U_{e2} & U_{e3} \\ U_{\mu 1} & U_{\mu 2} & U_{\mu 3} \\ U_{\tau 1} & U_{\tau 2} & U_{\tau 3} \end{pmatrix} \begin{pmatrix} \nu_1 \\ \nu_2 \\ \nu_3 \end{pmatrix}. \tag{2.19}
$$

The PMNS matrix can be parametrized in terms of 3 real mixing angles, θ_{ij} and a complex phase, δ, called the CP phase. Following the convention from the Particle Data Group [34], the expanded matrix takes the form

$$
\begin{aligned}
U &= \begin{bmatrix} c_{12}c_{13} & s_{12}c_{13} & s_{13}e^{-i\delta} \\ -s_{12}c_{23} - c_{12}s_{23}s_{13}e^{i\delta} & c_{12}c_{23} - s_{12}s_{23}s_{13}e^{i\delta} & s_{23}c_{13} \\ s_{12}s_{23} - c_{12}c_{23}s_{13}s^{i\delta} & -c_{12}s_{23} - s_{12}c_{23}s_{13}e^{i\delta} & c_{23}c_{13} \end{bmatrix} \\
&= \begin{bmatrix} 1 & 0 & 0 \\ 0 & c_{23} & s_{23} \\ 0 & -s_{23} & c_{23} \end{bmatrix} \begin{bmatrix} c_{13} & 0 & s_{13}e^{-i\delta} \\ 0 & 1 & 0 \\ -s_{13}e^{i\delta} & 0 & c_{13} \end{bmatrix} \begin{bmatrix} c_{12} & s_{12} & 0 \\ -s_{12} & c_{12} & 0 \\ 0 & 0 & 1 \end{bmatrix} \qquad (2.20)
\end{aligned}
$$

where $c_{ij} \equiv \cos\theta_{ij}$ and $s_{ij} \equiv \sin\theta_{ij}$.

With three neutrinos, the expanded forms of eq.s 2.13 and 2.15 can still balloon into unwieldy messes. Fortunately, based on current knowledge of the mass splittings, it is usually the case that only one mass splitting scale matters and other terms can be dropped. Fig. 2.2 shows a schematic of the mass splittings. For historic reasons, Δm^2_{21} is known as the solar mass splitting and the larger mass splitting is called the atmospheric mass splitting. The atmospheric mass splitting is about 30 times the solar mass splitting. The sign of the solar mass splitting is known, while that of the atmospheric mass splitting is not. A positive value of Δm^2_{32} is called the normal hierarchy; a negative value is called the inverted hierarchy.

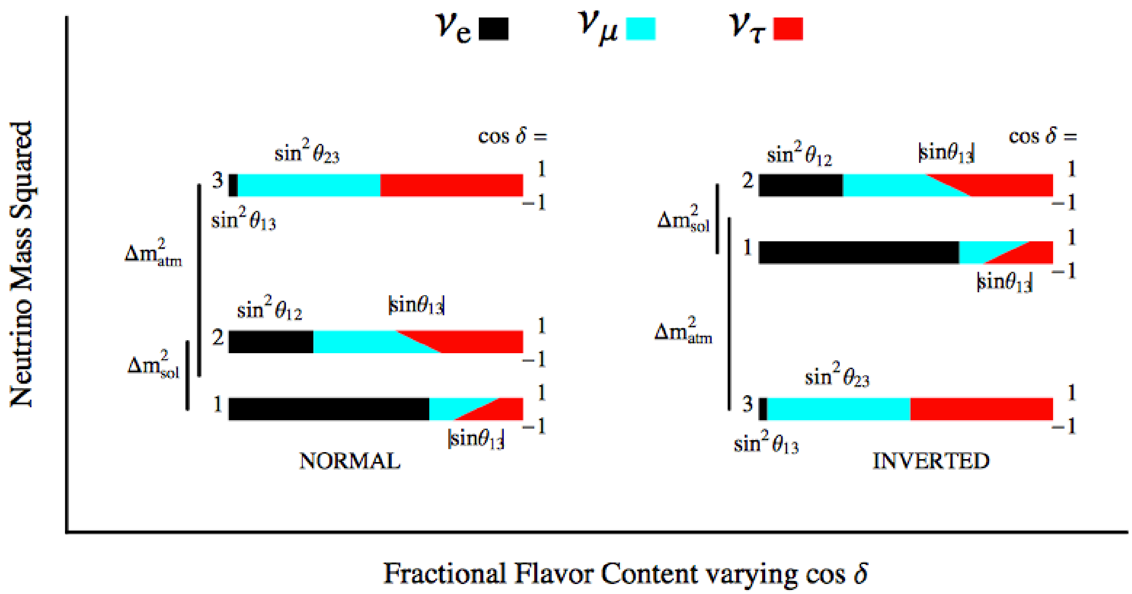

Figure 2.2: A schematic of the mass splittings between the three known neutrino mass states and how much they couple to each of the flavor states [35].

Two oscillation probabilities that are of interest to NOνA are the muon neutrino survival probability and electron neutrino appearance from a muon neutrino beam. Since $|\Delta m^2_{21}|$ is so much smaller than $|\Delta m^2_{32}|$, the solar oscillation baseline is much longer, thus the oscillation probability is first dominated by terms containing Δm^2_{32}. This is the case for NOνA. Furthermore, the probability can be simplified by making making the assumption that $|\Delta m^2_{32}| \approx |\Delta m^2_{31}|$. Under these conditions, the survival probability of muon neutrinos is calculated as follows:

$$
\begin{aligned}
P(\nu_\mu \to \nu_\mu) &\approx 1 - 4|U_{\mu 3}|^2(|U_{\mu 1}|^2 + |U_{\mu 2}|^2)\sin^2\Delta_{32} && (2.21)\\
&\approx 1 - 4s_{23}^2(1 - s_{13}^2)(c_{23}^2 + s_{23}^2 s_{13}^2)\sin^2\Delta_{32} && (2.22)\\
&\approx 1 - 4s_{23}^2 c_{23}^2 \sin^2\Delta_{32} + 4s_{23}^2 s_{13}^2(c_{23}^2 - s_{23}^2)\sin^2\Delta_{32} && (2.23)\\
&= 1 - \sin^2 2\theta_{23}\sin^2\Delta_{32} + 4\sin^2\theta_{23}\sin^2\theta_{13}\cos^2 2\theta_{23}\sin^2\Delta_{32} && (2.24)
\end{aligned}
$$

Between eq.s 2.22 and 2.23, the term proportional to s_{13}^4 was dropped using the current knowledge that s_{13}^2 is small [34]. Note that if θ_{13} were 0, then eq. 2.24 would reduce to eq. 2.17, the two neutrino survival probability.

The full 3 flavor electron neutrino appearance from muon neutrino oscillation probability is often written in the form [36]:

$$
P(\overset{(-)}{\nu}_\mu \to \overset{(-)}{\nu}_e) = P_{atm} + 2\sqrt{P_{atm}}\sqrt{P_{sol}}\left(\cos\delta\cos\Delta_{32} \overset{(+)}{-} \sin\delta\sin\Delta_{32}\right) + P_{sol} \qquad (2.25)
$$

where

$$
\begin{aligned}
\sqrt{P_{atm}} &\equiv \sin\theta_{23}\sin 2\theta_{13}\sin\Delta_{32} && (2.26)\\
\sqrt{P_{sol}} &\equiv \cos\theta_{23}\sin 2\theta_{12}\sin\Delta_{21} && (2.27)
\end{aligned}
$$

where the approximation $|\Delta m_{32}^2| \approx |\Delta m_{31}^2|$ has been made and higher order terms of s_{13}^2 been dropped. For an experiment at a short enough baseline such as NOνA, the P_{sol} term is negligible as it depends on a higher order term of the solar mass splitting. The cross term is also not the dominant effect as it also depends upon the solar mass splitting, but it demonstrates interesting behavior. The $\cos\delta$ term is CP conserving, but the $\sin\delta$ term exhibits CP violation. This is why δ is called the CP violating phase angle.

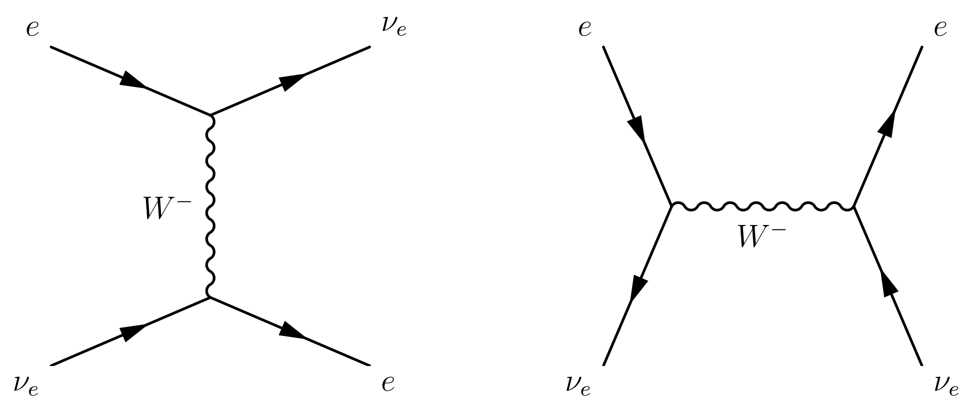

Figure 2.3: Coherent forward scattering interactions involved in the MSW effect. Left: Scattering of electron neutrinos on electrons. Right: Scattering of anti-electron neutrinos on electrons.

2.4 Matter Effects

So far, the oscillation formalism has been developed only considering neutrinos in a vacuum. However, most neutrino oscillation experiments involve neutrinos traveling through matter, be it the Sun or the Earth. This affects the oscillation probabilities in a process called the Mikheyev-Smirnov-Wolfenstein effect, or MSW effect. The phenomenon was first proposed by Wolfenstein in 1978 [37]; Mikheyev and Smirnov built upon that work in 1985 [38] as a possible solution for the solar neutrino problem.

The MSW effect is the coherent forward scattering of neutrinos off of the electrons in ordinary matter, a channel only available to electron flavor neutrinos and anti-neutrinos. Fig. 2.3 illustrates the interactions. The electrons contribute an additional potential term, $V_e = \pm\sqrt{2}G_F N_e$, where G_F is Fermi's constant, N_e is the electron number density, the positive sign is for neutrinos, and the negative for anti-neutrinos. Neutrinos also forward scatter off the neutrons and protons in matter via neutral current interactions, but this only provides an overall phase as all neutrino flavors participate in these interactions equally. The matter induced potential adds an additional term to the Schrödinger equation, affecting the time evolution of the flavor states and thus changing the oscillation probabilities.

The following derivation will consider the MSW effect in the case of two neutrino flavors. The time evolution of the flavor states is written as follows:

$$i \begin{pmatrix} \nu_e \\ \nu_\mu \end{pmatrix} = \left[U \begin{pmatrix} \frac{m_1^2}{2E} & 0 \\ 0 & \frac{m_2^2}{2E} \end{pmatrix} U^\dagger + \begin{pmatrix} \pm V_e & 0 \\ 0 & 0 \end{pmatrix} \right] \begin{pmatrix} \nu_e \\ \nu_\mu \end{pmatrix} \tag{2.28}$$

Inserting the 2 flavor PMNS matrix from eq. 2.16, applying some trigonometric identites, and dropping common diagonal terms, eq. 2.28 simplifies to

$$i \begin{pmatrix} \nu_e \\ \nu_\mu \end{pmatrix} = \frac{1}{4E} \begin{pmatrix} -\Delta m_{21}^2 \cos 2\theta \pm 4EV_e & \Delta m_{21}^2 \sin 2\theta \\ \Delta m_{21}^2 \sin 2\theta & \Delta m_{21}^2 \cos 2\theta \end{pmatrix} \begin{pmatrix} \nu_e \\ \nu_\mu \end{pmatrix}. \tag{2.29}$$

The diagonal terms are dropped because they can be absorbed by the phase convention of the neutrino states. This Hamiltonian can be re-diagonalized with another unitary transformation, $H_M = U_M^\dagger H U_M$, with the following results:

$$H_M = \frac{1}{2} \begin{pmatrix} -\frac{\Delta m_M^2}{2E} & 0 \\ 0 & \frac{\Delta m_M^2}{2E} \end{pmatrix} \tag{2.30}$$

$$U_M = \begin{pmatrix} \cos\theta_M & \sin\theta_M \\ -\sin\theta_M & \cos\theta_M \end{pmatrix}, \tag{2.31}$$

where

$$\sin 2\theta_M \equiv \frac{\sin 2\theta}{A_M} \tag{2.32}$$

$$\Delta m_M^2 \equiv \Delta m_{21}^2 A_M \tag{2.33}$$

$$A_M \equiv \sqrt{\left(\cos 2\theta \mp \frac{2EV_e}{\Delta m_{21}^2}\right)^2 + \sin^2 2\theta}, \tag{2.34}$$

and now the negative sign in A_M is for neutrinos and the positive sign for anti-neutrinos. As the electron number density goes to 0, so too does V_e and the vacuum solution is recovered.

From the form of this solution, it can be seen that the Hamiltonian takes the same form as that in vacuum oscillations, but with modified effective masses. Likewise, U_M has the same form as the 2 neutrino PMNS matrix, so θ_M can be considered the effective mixing angle. In the absence of neutrino oscillations (when $\theta = 0$), matter effects cannot "create" them. However, even for small angles θ, the matter effect can create a resonant effect pushing the effective mixing angle, θ_M, maximally to $45°$. This occurs when the term in parenthesis in the definition of A_M is 0 (eq. 2.34).

$$N_e^{res} = \frac{\Delta m_{21}^2 \cos 2\theta}{2\sqrt{2} G_F E} \tag{2.35}$$

In the case of 3 neutrinos, the same procedure is followed to diagonalize the Hamilton and obtain effective values for the various oscillation parameters. The effects are considerably more complicated, but the general effect is the same–matter changes the effective neutrino mass and alters the oscillation probability curves differently for neutrinos and anti-neutrinos. Under the same conditions that were used to calculate $P(\overset{(}{\bar{\nu}}\overset{)}{}_\mu \rightarrow \overset{(}{\bar{\nu}}\overset{)}{}_e)$ in sec. 2.3, the results can be simplified to a few basic replacements [39].

$$P(\overset{(}{\bar{\nu}}\overset{)}{}_\mu \rightarrow \overset{(}{\bar{\nu}}\overset{)}{}_e) = P_{atm}^M + 2\sqrt{P_{atm}^M}\sqrt{P_{sol}^M}\left(\cos\delta\cos\Delta_{32} \overset{(+)}{-} \sin\delta\sin\Delta_{32}\right) + P_{sol}^M \tag{2.36}$$

This is exactly the same form as eq. 2.25. The interesting effects are seen with how P_{atm}^M and P_{sol}^M differ from their respective vacuum counterparts.

$$\sqrt{P_{atm}^M} \equiv \sin\theta_{23}\sin 2\theta_{13}\frac{\sin(\Delta_{31} - aL)}{\Delta_{31} - aL}\Delta_{31} \tag{2.37}$$

$$\sqrt{P_{sol}} \equiv \cos\theta_{23}\sin 2\theta_{12}\frac{\sin(aL)}{aL}\Delta_{21} \tag{2.38}$$

Here, $a \equiv \pm G_F N_e/\sqrt{2}$ where the positive sign is for neutrinos and the negative sign for anti-neutrinos. For the Earth, $|a| \approx 1/3500\,km$.

The combined effect that appears in eq.s 2.36, 2.37, and 2.38 due to the presence of matter plays an interesting role in the search for CP violation. The MSW effect by itself mimics CP violation as it alters oscillation probabilities for neutrinos and anti-neutrinos differently. Depending on the value of δ that nature has chosen, the differences in oscillation probabilities due to the CP violation angle and the MSW effect can either compound or cancel out.

2.5 Current Measurements

Most of the free parameters in the PMNS matrix have been measured by various solar, atmospheric, accelerator, and reactor neutrino experiments. However, any given neutrino experiment does not have sensitivity to all of the oscillation parameters. Instead, experiments are sensitive to specific angles based on their baseline and the energies of the neutrinos they observe. Solar neutrino experiments, such as GALLEX, SAGE, Super-K, and SNO, measure neutrinos with energies on the order of several MeV after a very long baseline, and are most sensitive to θ_{12} and Δm^2_{21}. Due to the strong MSW effect within the Sun, solar neutrino experiments also determined the ordering of mass states ν_1 and ν_2; ν_2 is defined as the heavier state. Atmospheric neutrino experiments, such as Super-K, SNO, and MINOS, measure neutrinos generated by cosmic ray collisions with the Earth's atmosphere, and are sensitive to θ_{23} and Δm^2_{32}.

Reactor neutrino experiments, such as Chooz, Double Chooz, RENO, and Daya Bay, measure $\bar{\nu}_e$ generated by nearby nuclear reactors. Like solar neutrinos, reactor neutrinos have energies on the order of a few MeV. By measuring these neutrinos with a short baseline ($O(1km)$), the 2 neutrino approximation is valid, so the oscillation probability can be approximated as:

$$P(\bar{\nu}_e \rightarrow \bar{\nu}_e) \approx 1 - \sin^2 2\theta_{13} \sin^2 \Delta_{31}. \tag{2.39}$$

Daya Bay made the first nonzero measurement of θ_{13} in 2012, reporting a value of $\sin^2 2\theta_{13} = 0.092 \pm 0.016$ (stat) $\pm\ 0.005$ (syst) after taking just 55 days of data [40]. This result excluded a zero value for θ_{13} at 5.2σ and is shown in Fig. 2.4. Since that result, the limits have only continued to improve, and the leading measurement still comes from Daya Bay.

Accelerator neutrino experiments, such as MINOS, T2K, and NOνA, begin with a beam of nearly pure $\overset{(-)}{\nu}_\mu$ and search for both a disappearance of $\overset{(-)}{\nu}_\mu$ and appearance of other neutrino flavors. These experiments are sensitive to θ_{13}, θ_{23}, Δm^2_{32}, and δ. The experiments that have the largest matter effect are the most sensitive to δ and the mass hierarchy.

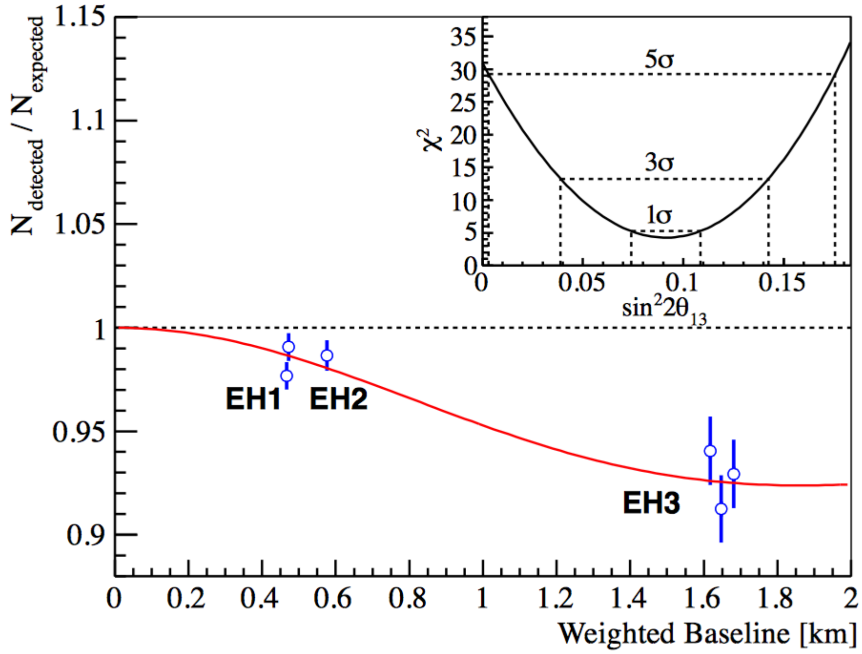

Figure 2.4: First measurement of θ_{13} from Daya Bay [40]. The points show the ratio of observed to expected events assuming $\theta_{13} = 0$. Each point is a measurement at a different detector. The inset in the upper corner shows the χ^2 value vs value of $\sin^2 2\theta_{13}$, and excludes $\theta_{13} = 0$ at greater than 5σ.

Global fits to the combined data of these (and other) neutrino experiments have been performed and summarized in [34, 41]; the best fit values are shown in Table 2.1. While most of the parameters have been measured with good precision, there are still a few lingering questions. From the table it is clear that a much better measurement on the CP violation angle is needed. The mass hierarchy still needs to be definitively measured as well. The other main question is whether θ_{23} is maximal, and if not, whether it is in the lower or upper octant.

Current and next generation reactor experiments have a great outlook to answer these outstanding questions. Making use of the MSW effect, the ν_e and $\bar{\nu}_e$ appearance results from experiments like T2K and NOνA could simultaneously measure δ, the mass hierarchy, and θ_{23} octant. The prospects for NOνAto make these measurements are shown in Fig. 2.5. The first analysis results from NOνA [42, 43] were published after taking about 10% of the experiments design statistics and already show promise. The NOνA measurement for δ, shown in Fig. 2.6, provide a hint toward the normal hierarchy and eliminate portions of δ space at 90% confidence.

Table 2.1: Current status of best fit oscillation parameters, from [34, 41]. The last column shows the allowed values within a 3σ range, with the exception of δ, which is shown at a 2σ range. This is because the current global best fit for δ still allows the full range from 0 to 2π at 3σ. NOνA should vastly improve the limits on δ.

Parameter		Best-Fit ($\pm 1\sigma$)	3σ Range
Δm^2_{21} [10^{-5} eV²]		$7.54^{+0.26}_{-0.22}$	$6.99 - 8.18$
$\lvert\Delta m^2\rvert$ [10^{-3} eV²]	NH	2.43 ± 0.06	$2.23 - 2.61$
	IH	2.38 ± 0.06	$2.19 - 2.56$
$\sin^2\theta_{12}$		0.308 ± 0.017	$0.259 - 0.359$
$\sin^2\theta_{23}$	NH	$0.437^{+0.033}_{-0.023}$	$0.374 - 0.628$
	IH	$0.455^{+0.039}_{0.031}$	$0.380 - 0.641$
$\sin^2\theta_{13}$	NH	$0.0234^{+0.0020}_{-0.0019}$	$0.0176 - 0.0295$
	IH	$0.0240^{+0.0019}_{-0.0022}$	$0.0178 - 0.0298$
δ/π (2σ range)	NH	$1.39^{+0.38}_{-0.27}$	$(0.00 - 0.16) \oplus (0.86 - 2.00)$
	IH	$1.31^{+0.29}_{-0.33}$	$(0.00 - 0.02) \oplus (0.70 - 2.00)$

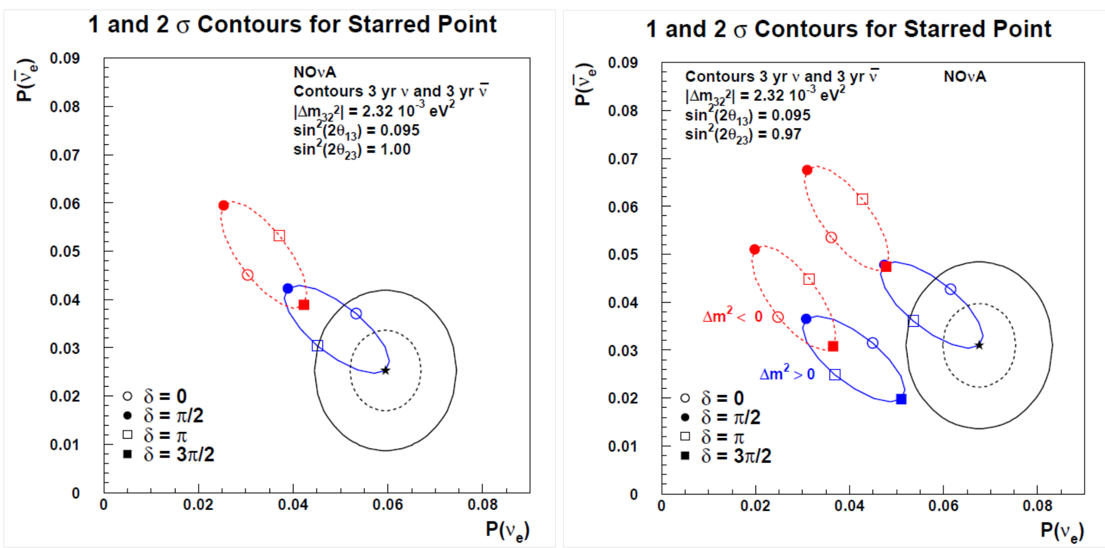

Figure 2.5: Probability of ν_e appearance versus $\bar{\nu}_e$ appearance at NOνA. The blue ellipses are for the normal hierarchy; the red ellipses are for the inverted hierarchy. The starred points show a possible measurement NOνA could make. The matter effect can either constructively or destructively combine with the CP violation effect. A larger matter effect, further separates the two mass hierarchy ellipses. This corresponds to neutrinos passing through more matter. On the left, θ_{23} is assumed to be $45°$ for maximal mixing, purely showcasing the interference between the matter and CP violation effects. On the right, θ_{23} is non-maximal, showing how the dependence on θ_{23} affects both ellipses in the same way.

2.6 Sterile Neutrinos

The analysis presented in this dissertation considers sterile neutrinos in a $3+1$ model. This adds a fourth neutrino flavor state, ν_s, and mass state, ν_4, and the PMNS matrix becomes a 4×4 matrix. Given that

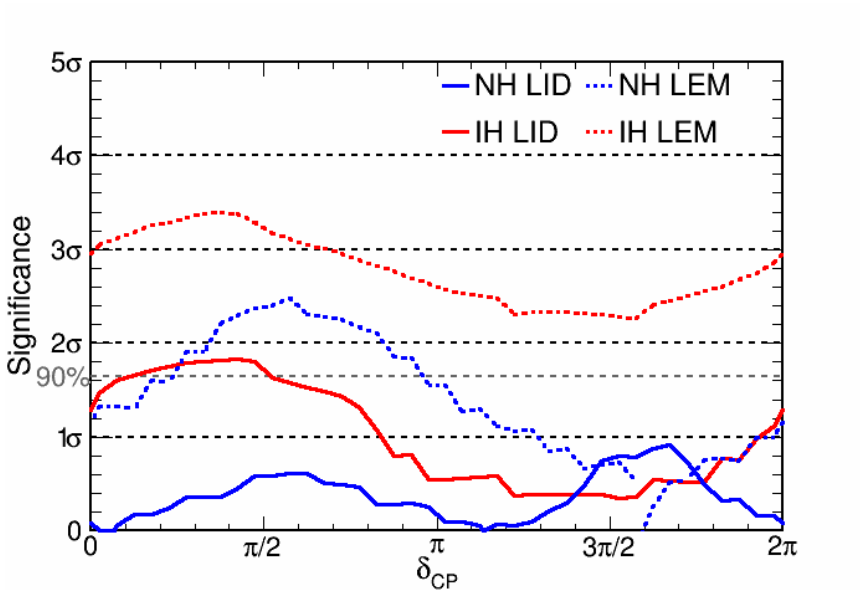

Figure 2.6: First measurement of δ from NOνA [42]. The plot shows the significance of the difference between the observed and predicted number of events as a function of delta. NOνA used a primary and secondary selection technique, the primary (secondary) technique is shown as the solid (dotted) line. The secondary selection disfavors the inverted hierarchy for all values of δ.

standard three flavor oscillations explain solar, atmospheric, and long-baseline oscillations so well, this fourth state must be mostly sterile, i.e., $|U_{\alpha 4}| \ll 1$ for $\alpha \in \{e, \mu, \tau\}$.

The mass splitting suggested by the experimental evidence discussed in section 1.4 is $\Delta m^2 \sim O(1\,\text{eV}^2)$. If the fourth neutrino mass state were the lightest, then all of the other mass states would have absolute masses $m \gtrsim 1$ eV. However, the sum of the active neutrino masses is well constrained by cosmology; the most recent Planck results reported $\sum m_\nu < 0.23$ eV [44]. Consequently, it is assumed that the additional neutrino mass state is heavier than the other three. Furthermore, since $\Delta m^2_{4i} \gg |\Delta m^2_{ji}|$ for $i, j < 4$, it is assumed that $\Delta_{41} \approx \Delta_{42} \approx \Delta_{43}$.

As mentioned above, adding a fourth neutrino state expands the PMNS matrix into a 4×4 matrix. It can be written as the product of individual (complex) rotation matrices, as in the second line of equation 2.20. This adds an additional 3 real rotation angles and 2 complex phases. It is a matter of convention on how exactly to add these mixing angles into the PMNS matrix, but as physical results cannot be affected by a particular parametrization, it is best to choose the most convenient one. Following the parametrization in [45], U takes the form:

$$U = R_{34}C_{24}R_{23}R_{14}C_{13}C_{12}, \tag{2.40}$$

where R_{ij} is a real matrix parametrized by a single mixing angle, θ_{ij}, and C_{ij} is a complex matrix parametrized by a real mixing angle θ_{ij} and complex phase δ_{ij}. This parametrization is convenient because as was the case in section 2.3, the solar mass scale Δ_{21} is negligible, thus mixing angles parametrized by C_{12} drop out of the oscillation probabilities. Based on this, equation 2.40 can be expanded in terms of the mixing angles:

$$U = \begin{bmatrix} U_{e1} & U_{e2} & c_{14}s_{13}e^{-i\delta_{13}} & s_{14} \\ U_{\mu 1} & U_{\mu 2} & -s_{14}s_{13}e^{-i\delta_{13}}s_{24}e^{-i\delta_{24}} + c_{13}s_{23}c_{24} & c_{14}s_{24}e^{-i\delta_{24}} \\ U_{\tau 1} & U_{\tau 2} & -s_{14}c_{24}s_{34}s_{13}e^{-i\delta_{13}} - c_{13}s_{23}s_{34}s_{24}e^{i\delta_{24}} + c_{13}c_{23}c_{34} & c_{14}c_{24}s_{34} \\ U_{s1} & U_{s2} & -s_{14}c_{24}c_{34}s_{13}e^{-i\delta_{13}} - c_{13}s_{23}c_{34}s_{24}e^{i\delta_{24}} - c_{13}c_{23}s_{34} & c_{14}c_{24}c_{34} \end{bmatrix} \tag{2.41}$$

Above, only the columns that appear in the oscillation probabilities have been expanded. Before using these expanded forms, however, it is useful to write the oscillation probability formulae in terms of the matrix elements first.

For NOνA, which starts with a nearly pure ν_μ beam, the two most important oscillation probabilities are the ν_μ survival probability, $P(\nu_\mu \to \nu_\mu)$ and the probability that a ν_μ will not oscillate to a sterile neutrino, $1 - P(\nu_\mu \to \nu_s)$. Starting with equations 2.15 and 2.13, these probabilities are calculated as follows, using the unitarity of U to remove elements found in its the first two columns.

$$\begin{aligned} P(\nu_\mu \to \nu_\mu) \approx 1 &- 4|U_{\mu 4}|^2(|U_{\mu 1}|^2 + |U_{\mu 2}|^2 + |U_{\mu 3}|^2)\sin^2\Delta_{41} \\ &- 4|U_{\mu 3}|^2(|U_{\mu 1}|^2 + |U_{\mu 2}|^2)\sin^2\Delta_{31} \\ \approx 1 &- 4|U_{\mu 4}|^2(1 - |U_{\mu 4}|^2)\sin^2\Delta_{41} \\ &- 4|U_{\mu 3}|^2(1 - |U_{\mu 3}|^2 - |U_{\mu 4}|^2)\sin^2\Delta_{31} \end{aligned} \tag{2.42}$$

$$
\begin{aligned}
1 - P(\nu_\mu \to \nu_s) = 1 \quad &+ \quad 4\sum_{i>j} \Re(U_{\mu i}U^*_{si}U_{sj}U^*_{\mu j})\sin^2\Delta_{ij} \\
&- \quad 2\sum_{i>j} \Im(U_{\mu i}U^*_{si}U_{sj}U^*_{\mu j})\sin 2\Delta_{ij} \\
\approx 1 \quad &+ \quad 4\Re(C_{41,42,43})\sin^2\Delta_{41} + 4\Re(C_{31,32})\sin^2\Delta_{31} \\
&- \quad 2\Im(C_{41,42,43})\sin 2\Delta_{41} - 2\Im(C_{31,32})\sin 2\Delta_{31} \qquad (2.43)
\end{aligned}
$$

In equation 2.43, $C_{41,42,43}$ and $C_{31,32}$ are sums of products of PMNS matrix elements.

$$
\begin{aligned}
C_{41,42,43} &= U_{\mu 4}U^*_{s4}(U_{s1}U^*_{\mu 1} + U_{s2}U^*_{\mu 2} + U_{s3}U^*_{\mu 3}) \\
&= U_{\mu 4}U^*_{s4}(-U_{s4}U^*_{\mu 4}) \\
&= -|U_{\mu 4}|^2|U_{s4}|^2 \qquad (2.44)
\end{aligned}
$$

Note that this term is real, thus the term with $\Im(C_{41,42,43})$ in equation 2.43 drops out.

$$
\begin{aligned}
C_{31,32} &= U_{\mu 3}U^*_{s3}(U_{s1}U^*_{\mu 1} + U_{s2}U^*_{\mu 2}) \\
&= -U_{\mu 3}U^*_{s3}(U_{s4}U^*_{\mu 4} + U_{s3}U^*_{\mu 3}) \\
&= -|U_{\mu 3}|^2|U_{s3}|^2 - U_{\mu 3}U^*_{\mu 4}U^*_{s3}U_{s4} \\
&= -|U_{\mu 3}|^2|U_{s3}|^2 - \Re(U_{\mu 3}U^*_{\mu 4}U^*_{s3}U_{s4}) - i\Im(U_{\mu 3}U^*_{\mu 4}U^*_{s3}U_{s4}) \\
&= -|U_{\mu 3}|^2|U_{s3}|^2 - \Re(U^*_{\mu 3}U_{\mu 4}U_{s3}U^*_{s4}) + i\Im(U^*_{\mu 3}U_{\mu 4}U_{s3}U^*_{s4}) \qquad (2.45)
\end{aligned}
$$

The last equality in 2.45 was done so that all terms in the oscillation probability are subtracted from 1. Using these results, equation 2.43 becomes

$$
\begin{aligned}
1 - P(\nu_\mu \to \nu_s) \approx 1 \quad &- \quad 4|U_{\mu 4}|^2|U_{s4}|^2\sin^2\Delta_{41} \\
&- \quad 4(|U_{\mu 3}|^2|U_{s3}|^2 + \Re(U^*_{\mu 3}U_{\mu 4}U_{s3}U^*_{s4}))\sin^2\Delta_{31} \\
&- \quad 2\Im(U^*_{\mu 3}U_{\mu 4}U_{s3}U^*_{s4})\sin 2\Delta_{31}. \qquad (2.46)
\end{aligned}
$$

Equations 2.42 and 2.46 are the probabilities that a ν_μ will survive as a ν_μ and survive as one of the active neutrino flavors, respectively. These can now be written in terms of the mixing angles. However, several approximations make the expressions much more bearable. First, based on the best value reported in section 2.5, the value of s_{13} is taken as 0. This has the fortunate side effect of removing any dependence on δ_{13} as well. Second, the value of s_{14} is also taken as 0, based on reactor and other constraints, e.g. [28, 46]. Note that in the relevant matrix elements, s_{13} and s_{14} always appear together as a product, further justifying the approximation. The matrix element products that appear in the oscillation probabilities are calculated below.

$$|U_{\mu 4}|^2 = s_{24}^2 \tag{2.47}$$

$$|U_{s4}|^2 = c_{24}^2 c_{34}^2 \tag{2.48}$$

$$|U_{\mu 3}|^2 = s_{23}^2 c_{24}^2 \tag{2.49}$$

$$|U_{s3}|^2 = c_{23}^2 s_{34}^2 + s_{23}^2 s_{24}^2 c_{34}^2 + 2 c_{23} s_{23} s_{24} c_{34} s_{34} \cos\delta_{24} \tag{2.50}$$

$$U_{\mu 3}^* U_{\mu 4} U_{s3} U_{s4}^* = -s_{23} c_{24}^2 s_{24} c_{34} (s_{23} s_{24} c_{34} + c_{23} s_{34} e^{-i\delta_{24}}) \tag{2.51}$$

$$\Re(U_{\mu 3}^* U_{\mu 4} U_{s3} U_{s4}^*) = -s_{23} c_{24}^2 s_{24} c_{34} (s_{23} s_{24} c_{34} + c_{23} s_{34} \cos\delta_{24}) \tag{2.52}$$

$$\Im(U_{\mu 3}^* U_{\mu 4} U_{s3} U_{s4}^*) = c_{23} s_{23} c_{24}^2 s_{24} c_{34} s_{34} \sin\delta_{24} \tag{2.53}$$

These results can be substituted into equations 2.42 and 2.46.

$$\begin{aligned}
P(\nu_\mu \to \nu_\mu) \approx 1 &- 4|U_{\mu 4}|^2 (1 - |U_{\mu 4}|^2) \sin^2\Delta_{41} \\
&- 4|U_{\mu 3}|^2 (1 - |U_{\mu 3}|^2 - |U_{\mu 4}|^2) \sin^2\Delta_{31} \\
\approx 1 &- 4 s_{24}^2 (1 - s_{24}^2) \sin^2\Delta_{41} \\
&- 4 s_{23}^2 c_{24}^2 (1 - s_{23}^2 c_{24}^2 - s_{24}^2) \sin^2\Delta_{31} \\
\approx 1 &- 4 c_{24}^2 s_{24}^2 \sin^2\Delta_{41} - 4 c_{24}^4 s_{23}^2 (1 - s_{23}^2) \sin^2\Delta_{31} \\
\approx 1 &- \sin^2 2\theta_{24} \sin^2\Delta_{41} - c_{24}^4 \sin^2 2\theta_{23} \sin^2\Delta_{31}
\end{aligned} \tag{2.54}$$

$$
\begin{aligned}
1 - P(\nu_\mu \to \nu_s) \approx 1 \quad &- \quad 4|U_{\mu 4}|^2 |U_{s4}|^2 \sin^2 \Delta_{41} \\
&- \quad 4(|U_{\mu 3}|^2 |U_{s3}|^2 + \Re(U^*_{\mu 3} U_{\mu 4} U_{s3} U^*_{s4})) \sin^2 \Delta_{31} \\
&- \quad 2\Im(U^*_{\mu 3} U_{\mu 4} U_{s3} U^*_{s4}) \sin 2\Delta_{31} \\
\approx 1 \quad &- \quad 4 c_{24}^2 s_{24}^2 c_{34}^2 \sin^2 \Delta_{41} \\
&- \quad 4 \left[s_{23}^2 c_{24}^2 (c_{23}^2 s_{34}^2 + s_{23}^2 s_{24}^2 c_{34}^2 + 2 c_{23} s_{23} s_{24} c_{34} s_{34} \cos \delta_{24}) \right. \\
&\quad\quad \left. - s_{23} c_{24}^2 s_{24} c_{34} (s_{23} s_{24} c_{34} + c_{23} s_{34} \cos \delta_{24}) \right] \sin^2 \Delta_{31} \\
&- \quad 2 c_{23} s_{23} c_{24}^2 s_{24} c_{34} s_{34} \sin \delta_{24} \sin 2\Delta_{31} \\
\approx 1 \quad &- \quad c_{34}^2 \sin^2 2\theta_{24} \sin^2 \Delta_{41} \\
&- \quad 4 \left[c_{23}^2 s_{23}^2 c_{24}^2 s_{34}^2 - s_{23}^2 c_{24}^2 s_{24}^2 c_{34}^2 (1 - s_{23}^2) \right. \\
&\quad\quad \left. + c_{23} s_{23} c_{24}^2 s_{24} c_{34} s_{34} (2 s_{23}^2 - 1) \cos \delta_{24} \right] \sin^2 \Delta_{31} \\
&- \quad \frac{1}{4} c_{24} \sin 2\theta_{23} \sin 2\theta_{24} \sin 2\theta_{34} \sin \delta_{24} \sin 2\Delta_{31} \\
\approx 1 \quad &- \quad c_{34}^2 \sin^2 2\theta_{24} \sin^2 \Delta_{41} - c_{24}^2 (s_{34}^2 - s_{24}^2 c_{34}^2) \sin^2 2\theta_{23} \sin^2 \Delta_{31} \\
&- \quad \frac{1}{4} c_{24} \sin 2\theta_{23} \sin 2\theta_{24} \sin 2\theta_{34} \sin \delta_{24} \sin 2\Delta_{31}
\end{aligned} \tag{2.55}
$$

In the last equality, the term proportional to $\cos \delta_{24}$ was dropped noting that $2s_{23}^2 - 1 \approx 0$. Even if it is not exact, there is already an additional factor of $s_{24} s_{34}$. Both s_{24} and s_{34} must be small in order to satisfy $|U_{\mu 4}|, |U_{\tau 4}| \ll 1$, thus the term proportional to $s_{24} s_{34} (2 s_{23}^2 - 1)$ can be considered higher order than the remaining terms.

The effect of each of the oscillation parameters can be seen in the figures below. Each page shows the ν_μ survival probability followed by the active neutrino survival probability and uses the exact oscillation probabilities. Figures 2.7-2.11 show how the mixing parameters that appear in equations 2.54 and 2.55 affect the oscillation probabilities. Figures 2.12-2.14 are similar but show the much smaller effects of the parameters that dropped out of these equations due to approximations. (Solar mixing parameters are not shown.) The individual plots show different probabilities curves while varying a single oscillation parameter over a set of representative values; the mixing parameters that are not varied in a particular figure are held fixed to the values in table 2.2. In the figures, the bottom axis shows the neutrino L/E, thus the plots show oscillation probabilities at both the near and far detectors. The top axis shows the neutrino energy at each NOνAdetector, the dashed line separates the Near Detector (ND) on the left from the Far Detector (FD) on the right. Finally, the grey bands show the neutrino energies each detector is sensitive to; a darker color means a higher intensity of neutrinos at that energy.

Table 2.2: The four flavor oscillation parameters assumed for studying the effects of different parameters on the oscillation probabilities.

Oscillation Parameter	Value
ρ	2.84 g/cm³
Δm^2_{21}	7.53×10^{-5} eV²
Δm^2_{32}	2.44×10^{-3} eV²
Δm^2_{41}	0.5 eV²
$\sin^2 2\theta_{12}$	0.846
$\sin^2 2\theta_{13}$	0.085
θ_{23}	$\pi/4$
θ_{14}	0
θ_{24}	$10°$
θ_{34}	$35°$
δ_{13}	0
δ_{24}	0

For the analysis presented in the rest of this dissertation, it is assumed that there are no Near Detector oscillations. Thus, the analysis will make measurements of θ_{24}, θ_{34}, and these will be translated into measurements of $|U_{\mu 4}|^2$ and $|U_{\tau 4}|^2$, and the results will be valid in the range $0.05 < \Delta m^2_{41} < 0.5$ eV^2.

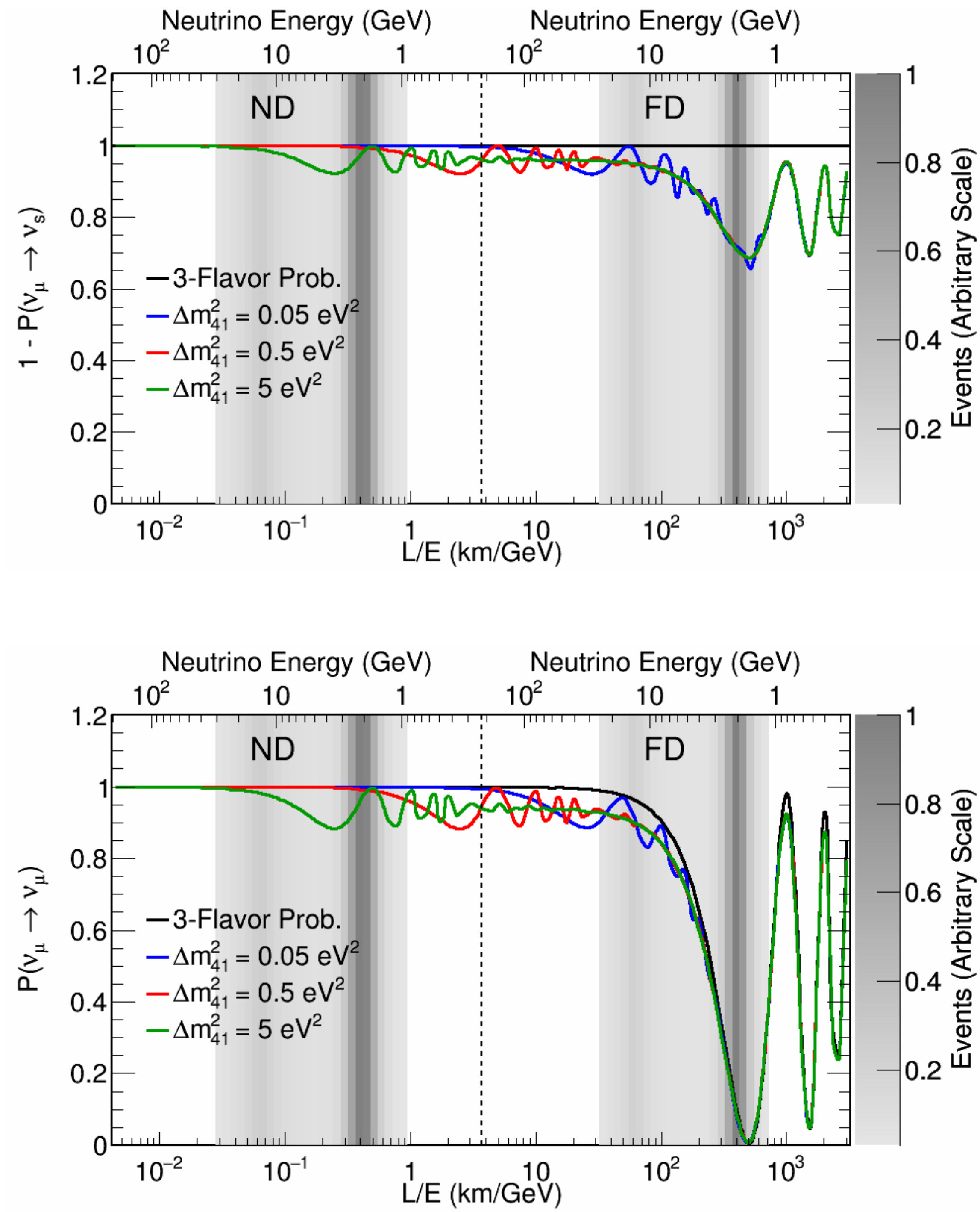

Figure 2.7: Total active neutrino survival probability (top) and ν_μ survival probability (bottom) for different values of Δm^2_{41}. Above $\Delta m^2_{41} = 0.5$ eV^2, oscillations start to affect the ND. The grey bands show the neutrino energy spectra observed by NOνA, with darker colors representing a higher intensity of neutrinos. Parameters not varied in the figures are held fixed to values shown in table 2.2.

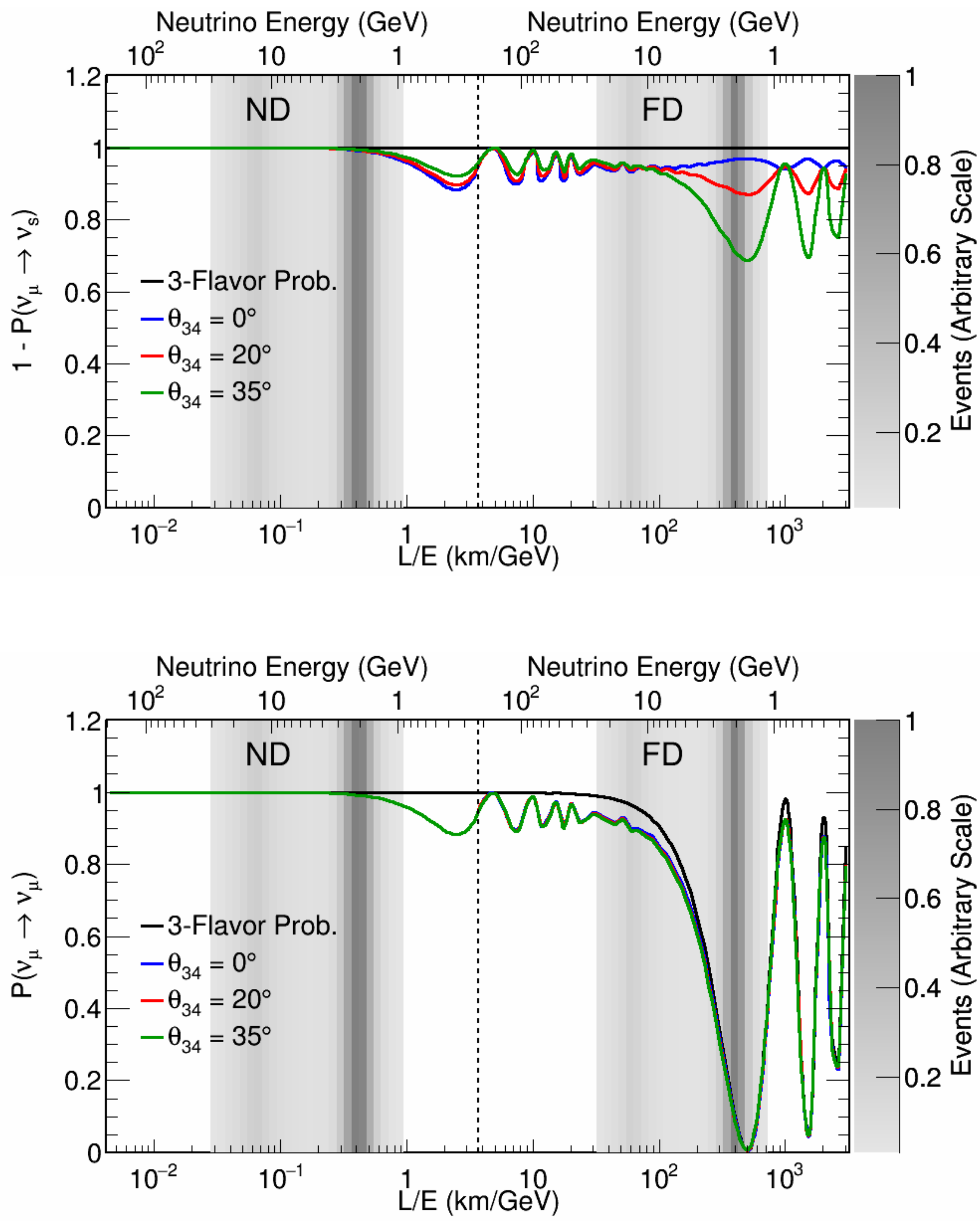

Figure 2.8: Total active neutrino survival probability (top) and ν_μ survival probability (bottom) for different values of θ_{34}. The grey bands show the neutrino energy spectra observed by NOνA, with darker colors representing a higher intensity of neutrinos. Parameters not varied in the figures are held fixed to values shown in table 2.2.

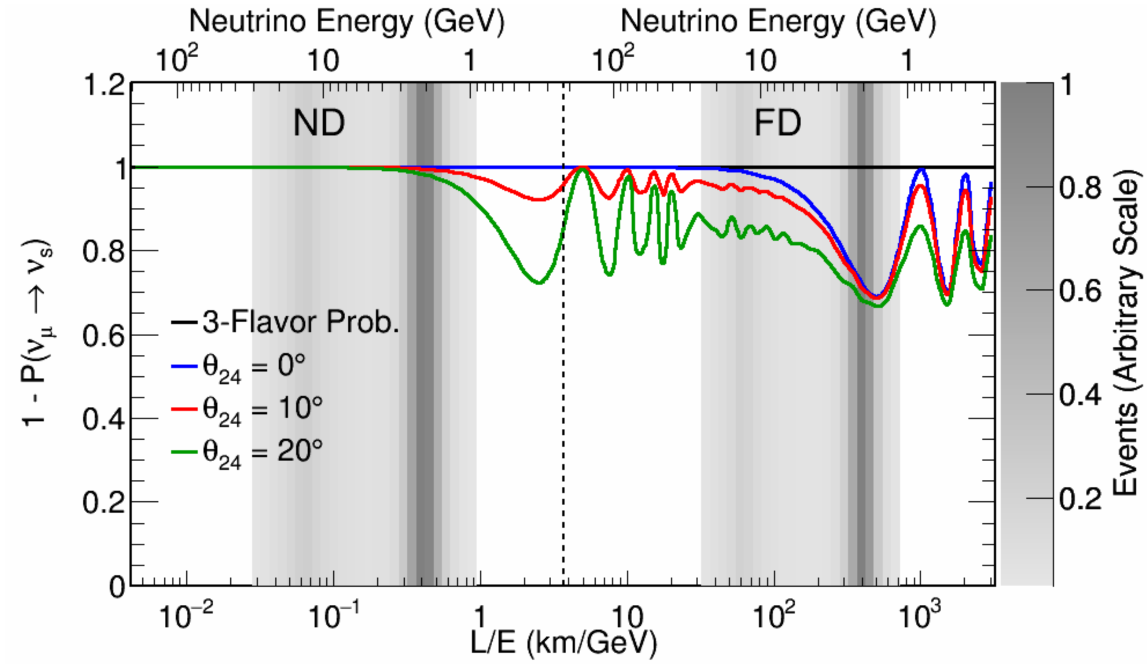

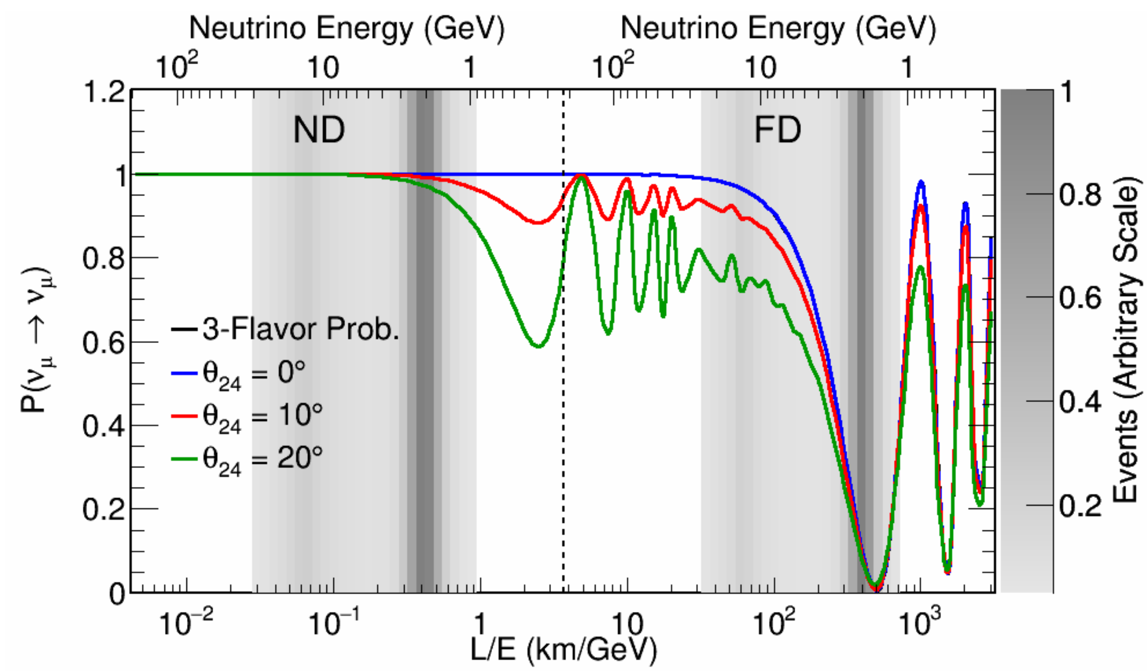

Figure 2.9: Total active neutrino survival probability (top) and ν_μ survival probability (bottom) for different values of θ_{24}. The grey bands show the neutrino energy spectra observed by NOνA, with darker colors representing a higher intensity of neutrinos. Parameters not varied in the figures are held fixed to values shown in table 2.2.

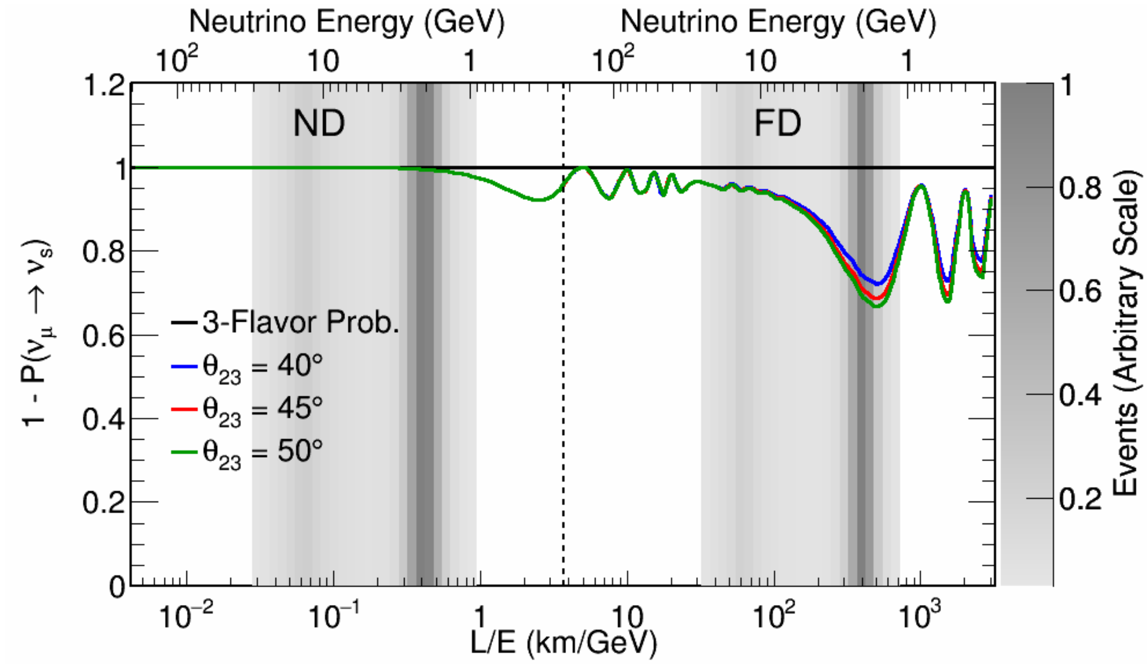

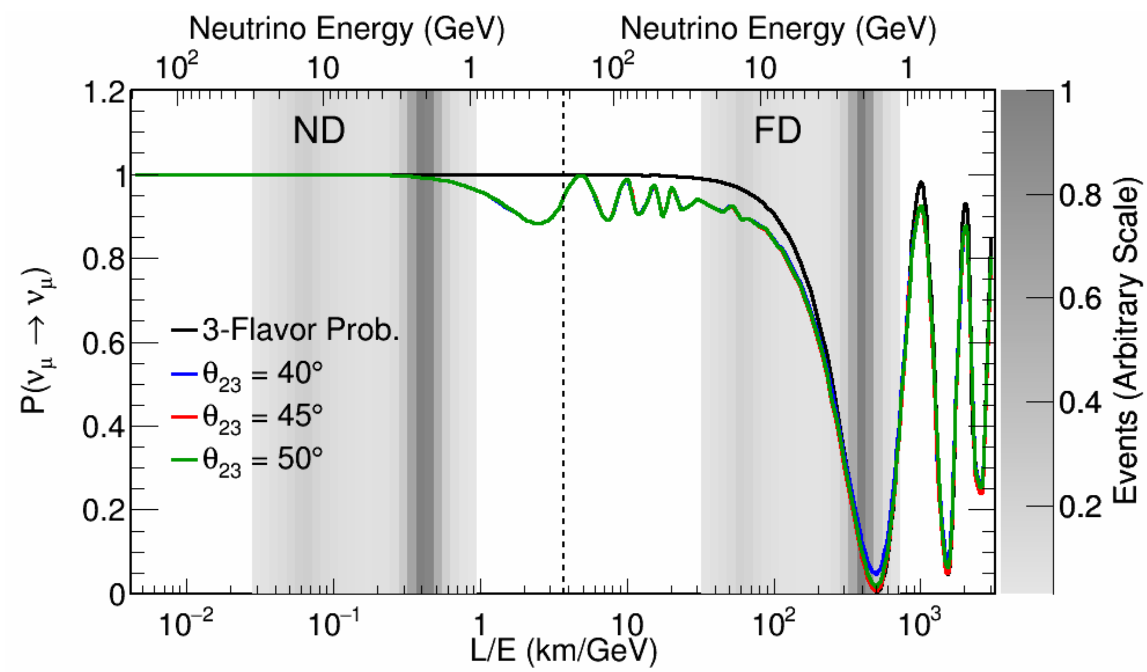

Figure 2.10: Total active neutrino survival probability (top) and ν_μ survival probability (bottom) for different values of θ_{23}. Shifts in θ_{23} have a modest effect at the NOνA peak energy. The grey bands show the neutrino energy spectra observed by NOνA, with darker colors representing a higher intensity of neutrinos. Parameters not varied in the figures are held fixed to values shown in table 2.2.

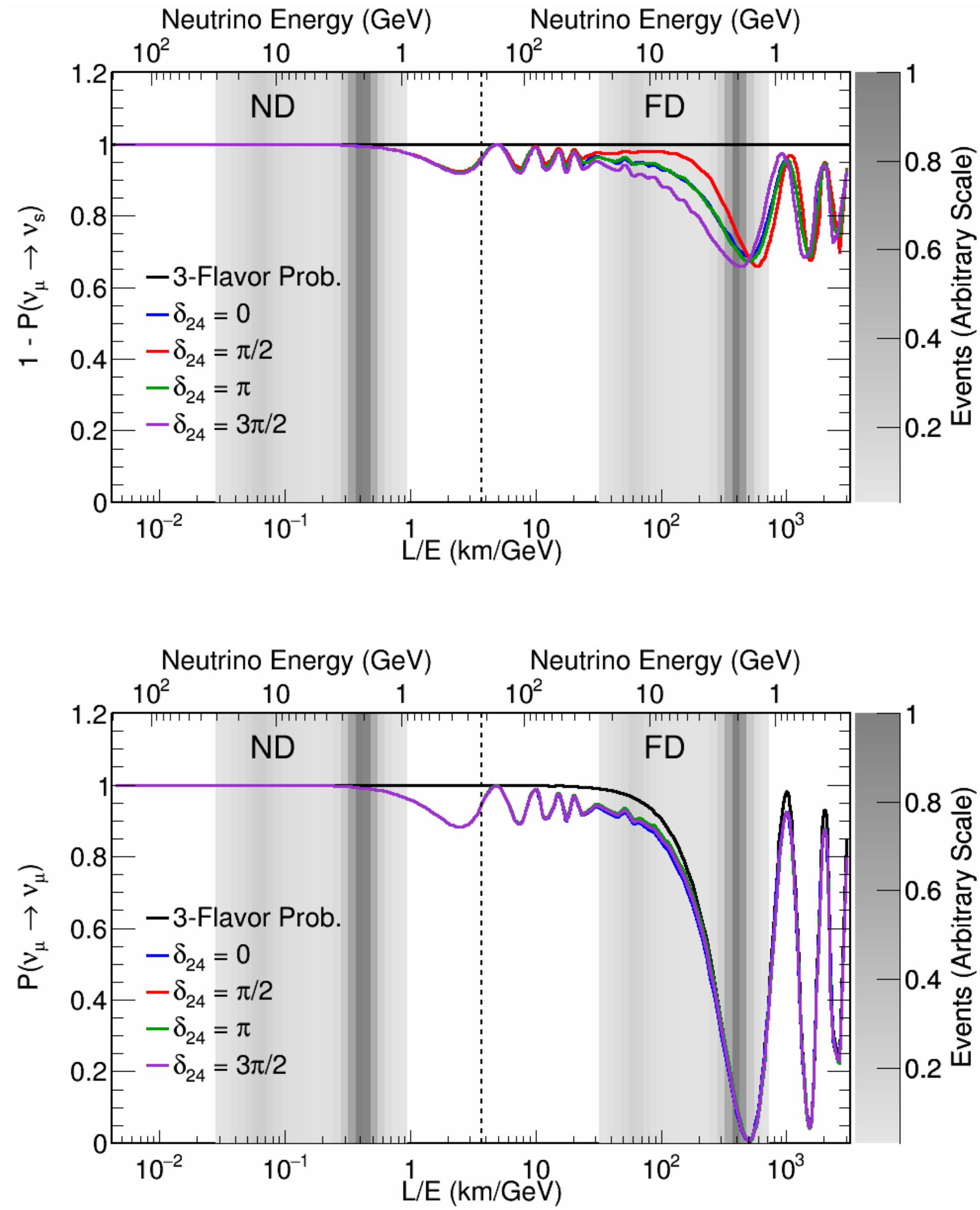

Figure 2.11: Total active neutrino survival probability (top) and ν_μ survival probability (bottom) for different values of δ_{24}. The grey bands show the neutrino energy spectra observed by NOνA, with darker colors representing a higher intensity of neutrinos. Parameters not varied in the figures are held fixed to values shown in table 2.2.

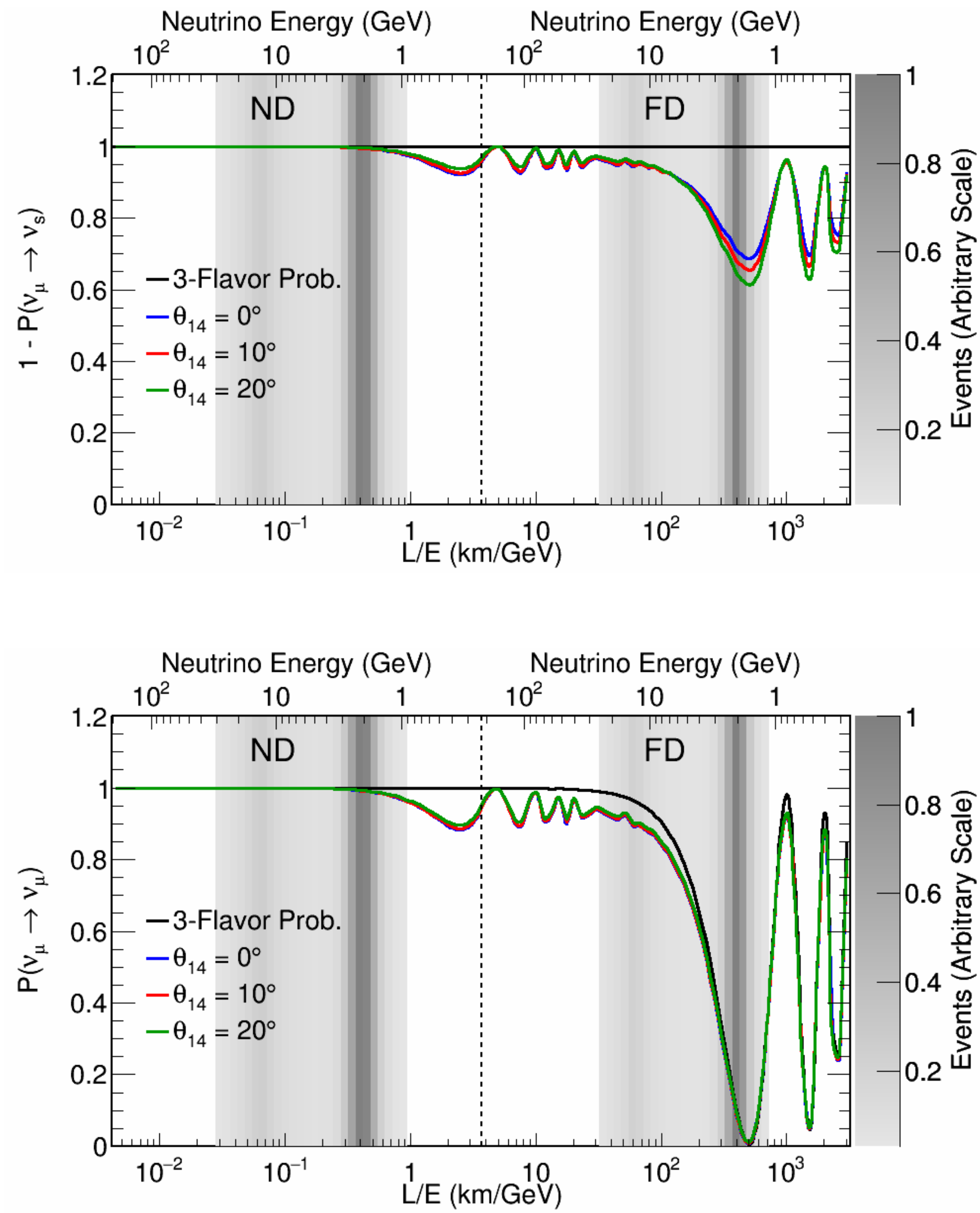

Figure 2.12: Total active neutrino survival probability (top) and ν_μ survival probability (bottom) for different values of θ_{14}. The values shown are well outside of experimental bounds, but even these large shifts have only a small effect on the oscillation probabilities that is largely degenerate with θ_{23}. The grey bands show the neutrino energy spectra observed by NOνA, with darker colors representing a higher intensity of neutrinos. Parameters not varied in the figures are held fixed to values shown in table 2.2.

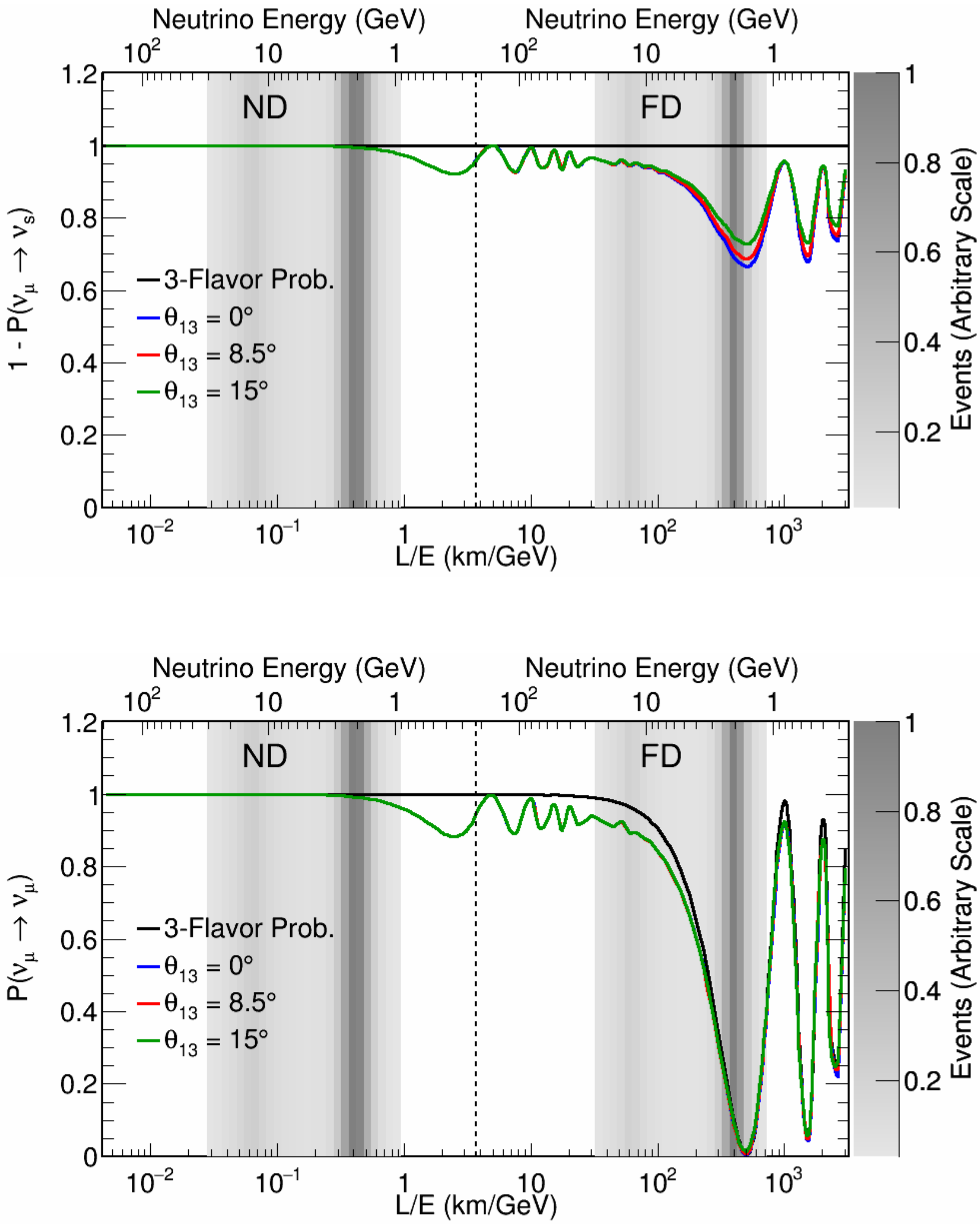

Figure 2.13: Total active neutrino survival probability (top) and ν_μ survival probability (bottom) for different values of θ_{13}. The values shown are well outside of experimental bounds, but even these large shifts have only a small effect on the oscillation probabilities that is largely degenerate with θ_{23}. The grey bands show the neutrino energy spectra observed by NOνA, with darker colors representing a higher intensity of neutrinos. Parameters not varied in the figures are held fixed to values shown in table 2.2.

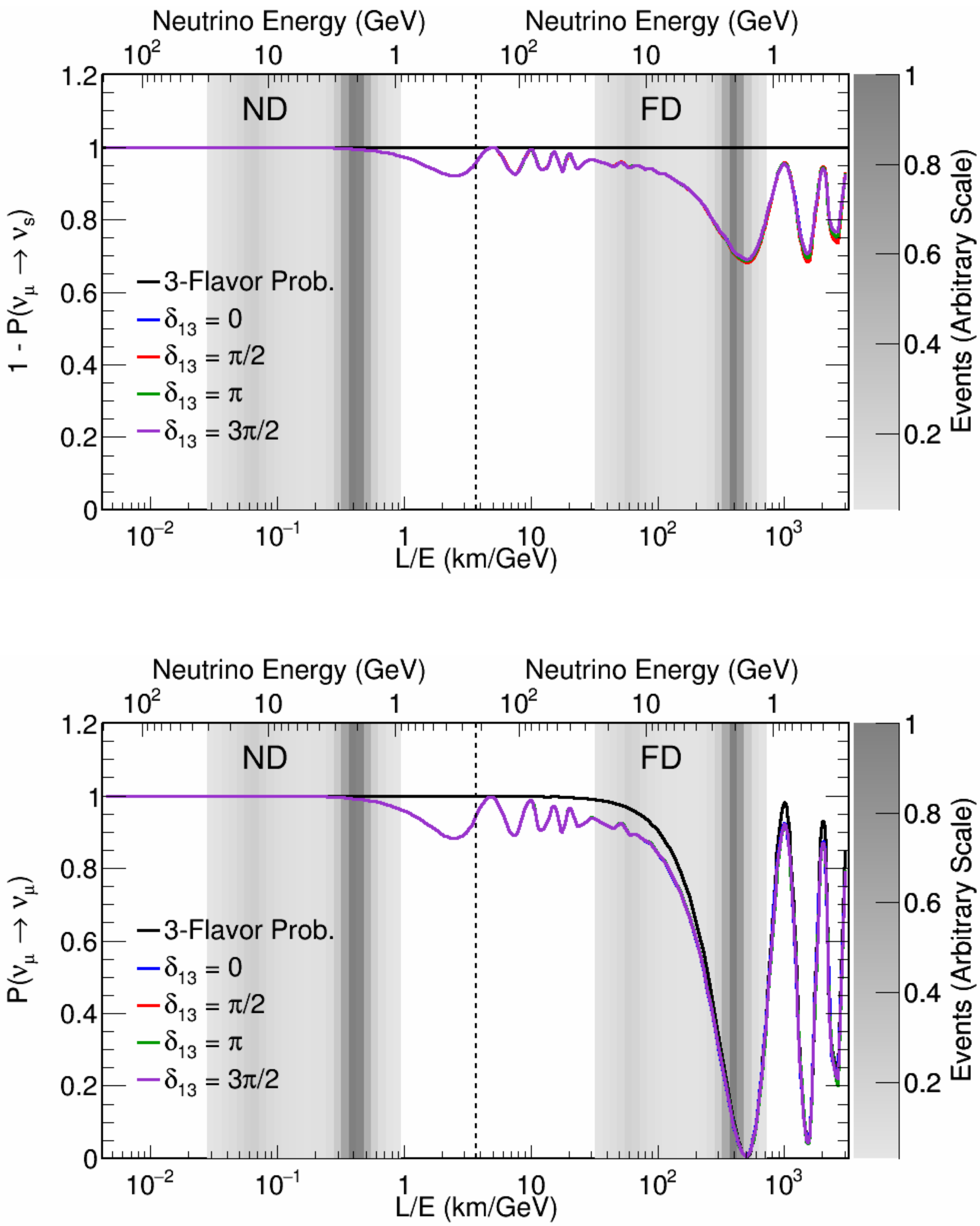

Figure 2.14: Total active neutrino survival probability (top) and ν_μ survival probability (bottom) for different values of δ_{13}. The effects of δ_{13} are negligible on the oscillation probabilities. The grey bands show the neutrino energy spectra observed by NOνA, with darker colors representing a higher intensity of neutrinos. Parameters not varied in the figures are held fixed to values shown in table 2.2.

3

The NOνA Experiment

4

Experiment Simulation

5

Event Reconstruction

5.1 Reconstruction Chain

5.2 Calibration

6

Neutral Current Event Selection

The NC disappearance analysis is performed by comparing the observed FD spectrum of NC events to the predicted number of events after extrapolation. This requires a largely pure sample of NC signal events. There are three main backgrounds for this sample, ν_e CC interactions, ν_μ CC interactions, and cosmic ray events. This chapter describes the full process for selecting a sample of NC events and eliminating backgrounds, briefly discussing data quality and event quality metrics, and fully detailing the fiducial, containment, NC selection, and cosmic rejection.

The analysis specific cuts were chosen based on the official SA files. These files were produced in tag R16-03-03, and NuS group specific DeCAF files were produced in tag S16-04-08. The cuts were trained on cosmic data from the cosmic trigger so that the actual cosmic prediction could come from the NuMI timing sideband. Beam events were oscillated assuming three flavor oscillations with the parameters listed in Table 6.1. For normalization simplicity, only 14 diblock MC and data were studied. After applying this criterion, all beam spectra were scaled to 6×10^{20} POT, and the cosmic spectra were scaled to

120 s. The remainder of this note describes each level of event cut and the data/MC comparison spectra from the ND as validation.

Table 6.1: The three flavor oscillation parameters assumed for studying the NC selection cuts

Oscillation Parameter	Value
ρ	$2.84\,\mathrm{g/cm^3}$
Δm^2_{21}	$7.53 \times 10^{-5}\,\mathrm{eV^2}$
$\sin^2 2\theta_{12}$	0.846
Δm^2_{32}	$2.40 \times 10^{-3}\,\mathrm{eV^2}$
θ_{23}	$\pi/4$
$\sin^2 2\theta_{13}$	0.084
δ	0

6.1 Data Quality

Data quality cuts were developed well before the first NOνA results to ensure proper data taking conditions, and all analysis groups apply them as standard. These cuts are applied per spill, and spills that fail these cuts are not included in POT accounting. The cuts can be categorized into three main groups, beam quality, data quality, and timing.

The beam quality cuts were studied and set as described in ref. [47]. These cuts ensure that the data was collected during acceptable conditions by cutting on metrics such as the beam position on the target, and the horn current. To be included, spills must meet all of the criteria listed in Table 6.2.

Table 6.2: Beam quality cuts applied to each spill to ensure proper data taking conditions. Taken from ref. [47].

Beam Quality Parameter	Minimum	Maximum
Spill POT	2.00×10^{12}	
Horn Current	$-202\,\mathrm{kA}$	$-198\,\mathrm{kA}$
Beam X and Y position on target	$0.02\,\mathrm{mm}$	$2.00\,\mathrm{mm}$
Beam X and Y width	$0.57\,\mathrm{mm}$	$1.58\,\mathrm{mm}$
Time to nearest beam spill		$0.5\,\mathrm{s}$

Two data quality cuts were applied to data from each detector. These cuts were motivated and set as described in [48, 49, 50], and are summarized in Table 6.3. The ND observes a higher level of noise when lights are on in the detector hall, so a cut is placed on one of the particularly noisy DCMs. Also at the ND, data is only considered good if all of the DCMs are active. A similar cut at the FD is made, but as the detector conditions were changing during commissioning, the cut is made using the LiveGeometry package that properly handles a changing detector. The other cut applied at the FD is an 'edge metric' that looks for tracks matching across DCM boundaries and cuts spills where the fraction of matches is too low, cutting spills where the DCMs were out of sync relatively to one another.

Table 6.3: Data quality cuts applied to each spill to ensure proper data taking conditions.

Data Quality Parameter	Detector	Metric for Spill to Pass
Number of Missing DCMs	ND	$= 0$
Lights On Effect Hit Fraction	ND	≤ 0.45
Missing DCMs from LiveGeometry	FD	$= 0$
DCM Edge Match Fraction	FD	> 0.2

Finally, a timing cut is applied to cosmic data to ensure that the data is not too close to the edge of the data taking window. For cosmic events within a given $500\ \mu s$ trigger window, only events between $25\ \mu\text{s} < t < 475\ \mu\text{s}$ are kept.

Table 6.4 shows the number of events that pass these data quality cuts, and fig. 6.1 shows the energy spectra at the ND and FD.

Table 6.4: The number of events that pass the data quality cuts, at both detectors.

Cut Level	NC	ν_μ CC	ν_e CC	Cosmic
FD:				
Data Quality	363.1	298.1	65.0	14.4 $\times 10^6$
ND ($\times 10^3$):				
Data Quality	12260	86703	1085	

6.2 Event Quality

Event quality cuts are the first applied to individual events and ensure that there is enough reconstructed information to be properly analyzed and that there were no obvious reconstruction failures. As with

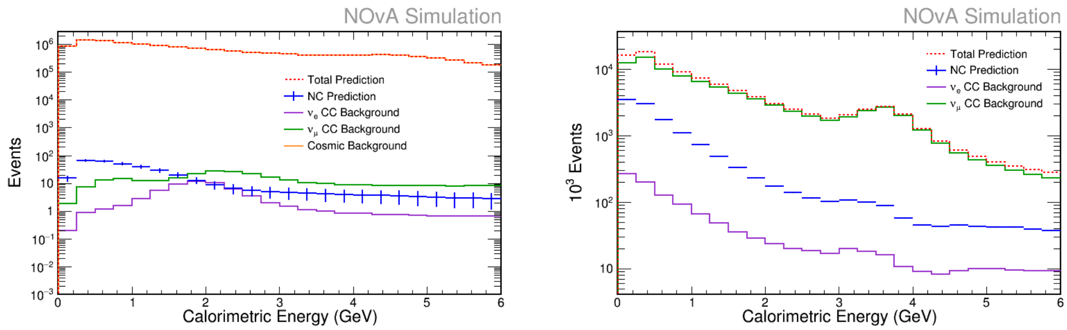

Figure 6.1: Energy spectra after Data Quality cuts for the FD (left) and ND (right).

the data quality cuts above, these cuts were taken directly from the ν_e [51, 52] and ν_μ [53] analyses. Two of the cuts within this suite simply require the presence of a reconstructed vertex and a shower object. These reconstructed objects are used more extensively in later stages, so the event quality cuts make sure they are available. Other quantities considered are the number of hits per plane, distance between the reconstructed vertex and leading shower, and number of contiguous planes. Events with a high number of hits per plane are cut to remove so called 'FEB Flashers,' an event most often triggered by high energy cosmic rays. The events have a signature where all of the cells read out by an FEB appear to be triggered. Events with a low number of contiguous planes are most often associated with very vertical cosmic rays, so events with a low number of planes are cut. Finally, a large distance between a vertex and leading shower is considered a reconstruction failure. These cuts are summarized with the exact parameters used for the cuts in Table 6.5. The number of events before and after the event quality cuts are listed in Table 6.6, and fig. 6.2 shows the energy spectra of the events that pass these cuts.

Table 6.5: Quality cuts applied to individual events to ensure properly reconstructed quantities.

Event Quality Metric	Metric for Event to Pass
Number of vertex objects	> 0
Number of shower objects	> 0
Number of hits per plane	< 8
Number of contiguous planes	> 2
Distance between vertex and leading shower	< 100 cm

Table 6.6: The number of events before and after application of event quality cuts, at both detectors.

Cut Level	NC	ν_μ CC	ν_e CC	Cosmic
FD:				
Data Quality	363.1	298.1	65.0	14.4 $\times 10^6$
+Event Quality	226.6	121.7	59.7	0.176 $\times 10^6$
ND ($\times 10^3$):				
Data Quality	12260	86703	1085	
+Event Quality	7518	45752	658	

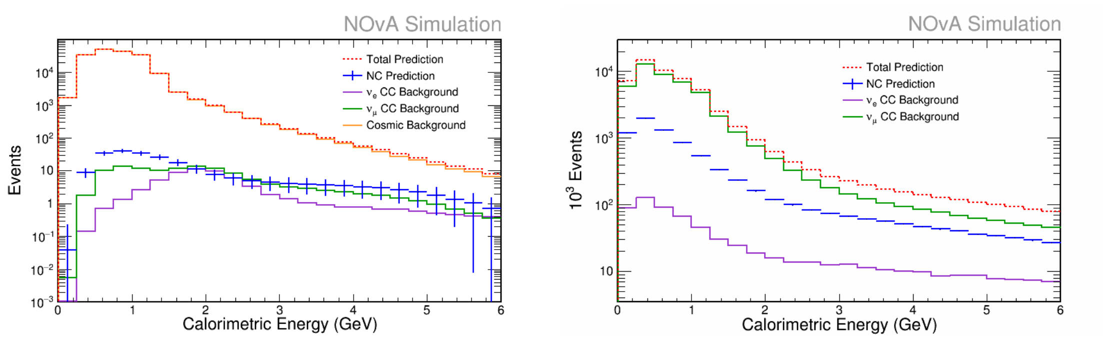

Figure 6.2: Energy spectra after Event Quality cuts for the FD (left) and ND (right).

6.3 Fiducial Volume and Containment

Fiducial volume and containment cuts are applied to remove events originating outside of the detector and to ensure that events originating inside of the detector do not have activity that escapes the detector. The fiducial volume cut is a cut on the location of the reconstructed neutrino vertex. The containment cut considers the leading shower of an event and cuts the event if the start or stop point is too close to a detector wall. The specific cuts were set separately at each detector.

6.3.1 Far Detector

For the FD, the fiducial and containment cuts are the first major step in reducing the cosmic background. Since cosmic ray events originate above the detector, there are many more cosmic events with reconstructed vertices in the upper portion of the detector. The fiducial volume cut in Y is thus applied in an asymmetric way to eliminate more of the cosmic background. The fiducial volume cut on Z (the beam direction) is also asymmetric to account for cosmic rays entering the back of the detector hall where there is a smaller amount of rock overburden to shield these events. The fiducial volume cut on X is also applied slightly asymmetrically for a slight performance gain. Events that pass these fiducial cuts must still pass the containment cuts. For the FD, the start and stop points of the leading prong must be further than 10 cm of any detector face. Fig. 6.3 shows the distributions of these variables before application of the fiducial or containment cuts. Table 6.8 summarizes the event rates before and after applying fiducial and containment cuts; fig. 6.4 show the energy spectra of events that pass these cuts.

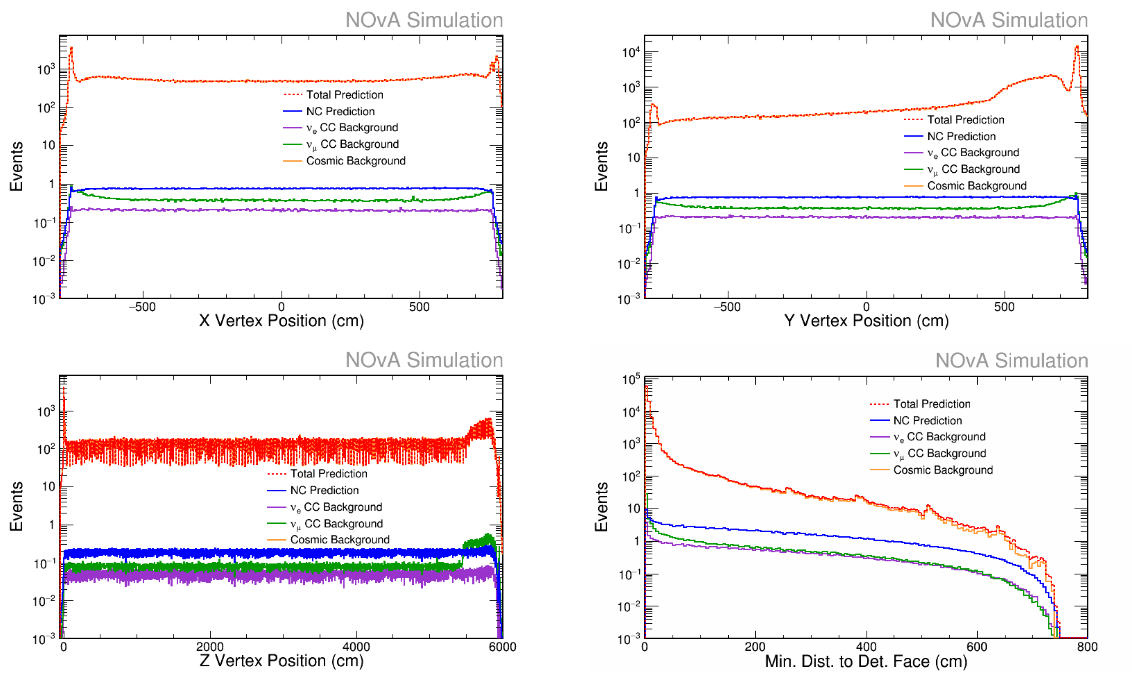

Figure 6.3: Distributions of variables used for fiducial and containment cuts at the FD. The top left, top right, and bottom left show the distributions of the reconstructed vertex. The bottom right shows the minimum distance between the start or stop of the leading prong to any detector face.

Table 6.7: Fiducial and containment cuts applied to events in the FD.

Reconstructed Quantity	Metric for Event to Pass
Reconstructed Vertex X Coordinate	$-680\text{ cm} \leq vtxX \leq 650\text{ cm}$
Reconstructed Vertex Y Coordinate	$-720\text{ cm} \leq vtxY \leq 600\text{ cm}$
Reconstructed Vertex Z Coordinate	$50\text{ cm} \leq vtxZ \leq 5450\text{ cm}$
Leading prong start/stop distance to detector face	$> 10\text{ cm}$

Table 6.8: The number of events before and after application of fiducial and containment cuts at the FD.

Cut Level	NC	ν_μ CC	ν_e CC	Cosmic
...Event Quality	226.6	121.7	59.7	175900
+ Fiducial	142.2	49.2	37.2	13550
+ Containment	139.5	44.9	36.5	2295

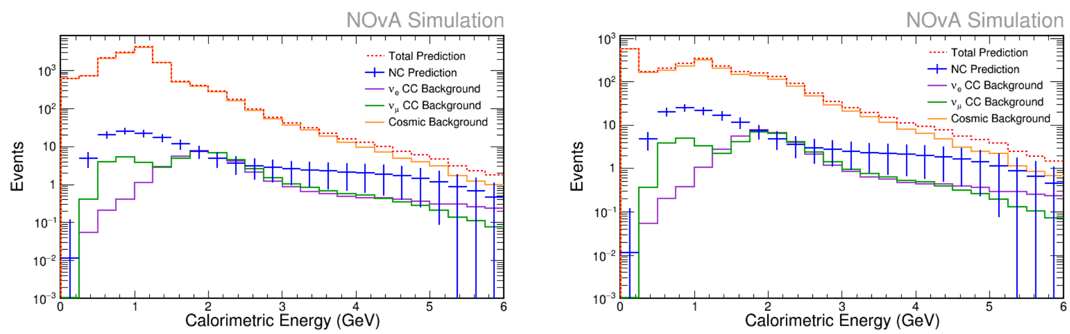

Figure 6.4: Energy spectra after fiducial and containment cuts for the FD. On the left, the cuts applied are data quality, event quality, and fiducial. The right plot also includes the containment cut.

6.3.2 Near Detector

While the ND does not have a large cosmic background to eliminate, there are many events that originate in the rock outside of the detector that can leak into the detector. Furthermore, the small size of the ND means that many events have activity that escapes outside of the detector. The fiducial and containment cuts at the ND are designed to combat both of these effects. The fiducial cuts on the X and Y coordinates of the reconstructed vertex were applied symmetrically, with a modestly large cut to remove events that originate in the rock outside the detector. The vertex cut on Z also cuts a large portion of the detector to cut rock events that leak into the front of the detector. The containment cuts at the ND are more strict than the FD. The leading prong is required to be greater than 25 cm from each detector face, and every track in the event is also subject to this cut. For the cut on each track, the back 'face' of the detector is considered to be the last plane of the fully active portion of the detector, effectively cutting events with activity in the muon catcher. All of these cuts are summarized in Table 6.9, Table 6.10 lists the event rates before and after the cuts are applied, and fig. 6.5 shows the energy spectra of events that pass these cuts.

Table 6.9: Fiducial and containment cuts applied to events in the ND.

Reconstructed Quantity	Metric for Event to Pass
Reconstructed Vertex X Coordinate	$-100\text{ cm} \leq vtxX \leq 100\text{ cm}$
Reconstructed Vertex Y Coordinate	$-100\text{ cm} \leq vtxY \leq 100\text{ cm}$
Reconstructed Vertex Z Coordinate	$200\text{ cm} \leq vtxZ \leq 1000\text{ cm}$
Leading prong start/stop point, distance to detector face	> 25 cm
Each track start/stop point, distance to detector face	> 25 cm

Table 6.10: The number of events before and after application of fiducial and containment cuts at the ND. Here, containment refers to cuts on the distance of the leading prong and each track to the closest detector face.

Cut Level	NC	ν_μ CC	ν_e CC
...Event Quality	7518	45752	658
+ Fiducial	619.3	1437.1	30.8
+ Containment	343.6	382.0	15.4

6.4 NC Selection

All of the cuts discussed to this point ensure that the remaining sample of events are well reconstructed, contained events. The remaining events should all be representative of their respective types, i.e., NC, ν_e CC, and ν_μ CC. The NC selection cuts are designed to select a relatively pure sample of NC events from amongst the CC backgrounds. The LID, RemID, and CVN PID distributions all have power to complete this goal, though only CVN was ultimately the only PID used. Finally, we use a cut on the number of hits for a small performance gain at the ND.

CVN, discussed in detail in ref. [?], does not attempt to identify a single event type; rather, it gives the most likely event type among all possibilities. CVN is a convolutional neural network that only takes the raw event topology as input. The algorithm applies a series of convolutional filters to search for key event features as opposed to taking these features as input, then trains against these features. Since this PID attempts to classify all event types, cutting events that have a low NC score removes a significant majority of all background types.

RemID, discussed in detail in ref. [54], is specifically designed to identify muons from charged pions, and provides separation power to remove ν_μ CC events that score highly under this PID. The PID is

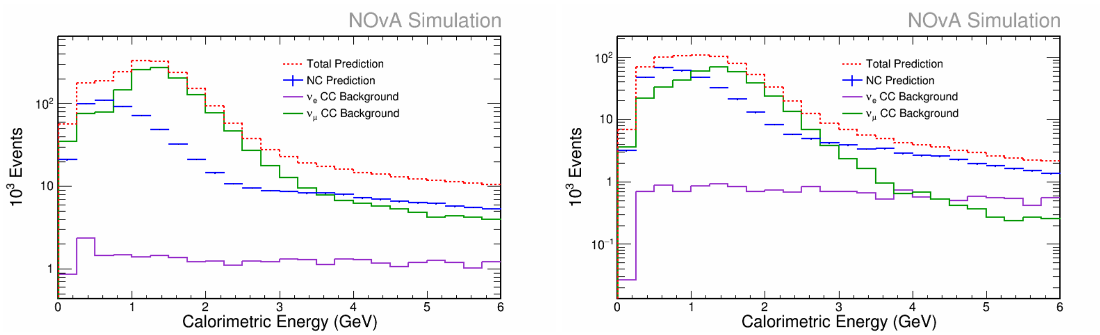

Figure 6.5: Energy spectra after fiducial and containment cuts for the ND. On the left, the cuts applied are data quality, event quality, and fiducial. The right plot also includes the containment cuts.

trained using a k−Nearest Neighboor classification on four input variables for a reconstructed track, the track energy deposition log likelihood, a scattering log likelihood, the track length, and the fraction of planes passed by the track that are uncontaminated by vertex or hadronic activity.

LID, described in ref. [55], has the power to remove ν_e CC events. This PID uses an artificial neural network to test the most energetic shower against electron, muon, proton, neutron, pion (charged and neutral), and photon hypothesis. The main inputs to this PID are the longitudinal and transverse energy deposition, but it also considers the fraction of event energy contained in the primary shower, the invariant mass of all event showers, the energy contained within eight planes of the vertex, the distance between the event vertex and shower start point, and the angle of the shower away from the beam direction.

Chronologically, CVN was developed later than RemID and LID, thus these PIDs were originally used to develop the analysis. While they were replaced by CVN as the sole PID used in the analysis, they nevertheless provided a valuable check that CVN was behaving sensibly. The PID distributions for RemID and LID were studied before and after applying the cut chosen on CVN to ensure that it was removing largely the same events, and if there were any other minor performance increases to be gained. Fig. 6.6 shows these distributions. Based on the results, it was decided that CVN provided all of the necessary separation power and so RemID and LID were not used in the analysis.

The distributions of CVN and the number of hits at the FD are shown in fig. 6.7. Table 6.11 summarizes the cuts used, table 6.12 lists the event rates before and after the selection cuts are applied, and

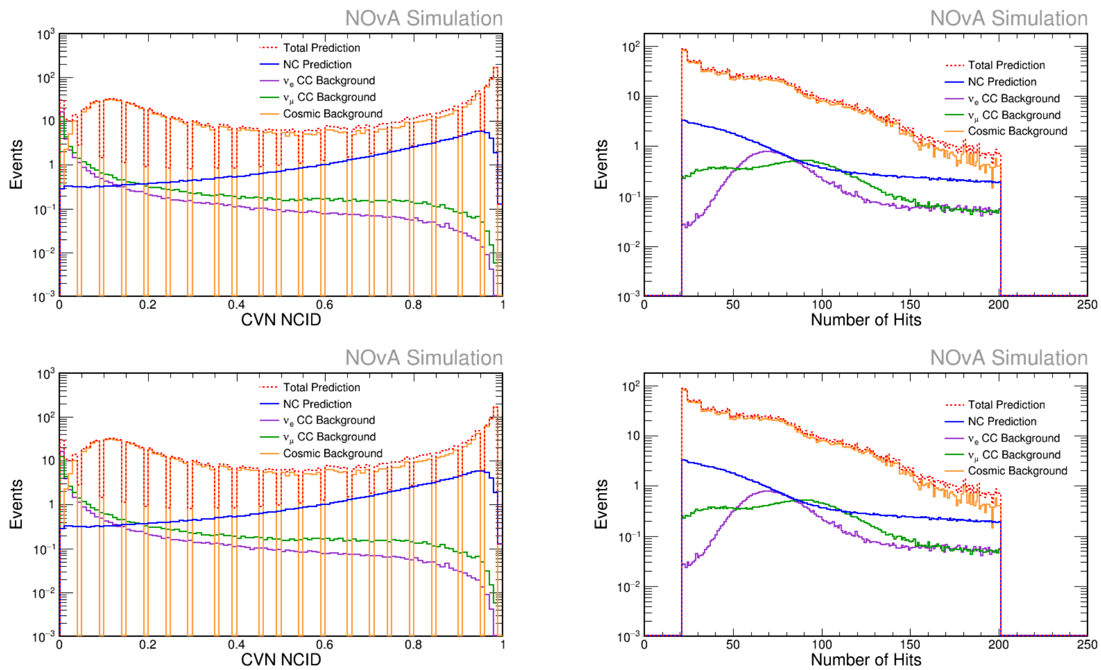

Figure 6.6: Distributions of RemID (left column) and LID (right column) at the FD before (top row) and after (bottom row) applying the cut on CVN listed in Table 6.11.

fig. 6.8 shows the energy distributions of events that pass these cuts.

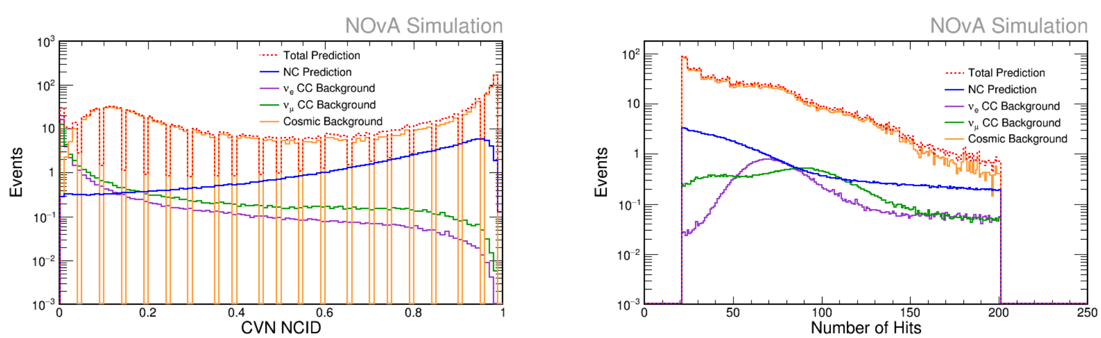

Figure 6.7: Distributions of variables used for NC selection at the FD.

6.5 Cosmic Rejection

The final set of cuts applied to the events is cosmic rejection. While there are essentially no cosmic events at the ND, the cuts are still applied at the ND when possible to maintain similar spectra at both detectors. The main variable to discriminate against cosmics is the output of a boosted decision tree originally

Table 6.11: NC selection cuts to reject CC events, leaving a relatively pure sample of NC events.

Selection Parameter	Metric for Event to Pass
CVN NC distribution score	≥ 0.2
Number of Hits	≤ 200

Table 6.12: The number of events before and after application of NC selection cuts, at both detectors.

Cut Level	NC	ν_μ CC	ν_e CC	Cosmic
FD:				
...Containment	139.5	44.9	36.5	2295
+NC Selection	132.9	12.8	6.7	339.0
ND ($\times 10^3$):				
...Containment	343.6	382.0	15.4	
+NC Selection	296.9	136.0	4.2	

tuned for the ν_μ disappearance analysis [56]. This algorithm takes a number of inputs, mainly based on the reconstructed track, such as the angle from the beam, the track length, and number of hits in the track. Another powerful discriminant is the fraction of total transverse energy deposition versus total event energy deposition, originally developed for the ν_e appearance analysis [52]. The other cuts used for cosmic rejection are a cut on low average energy per hit, a harsher cut on the start/stop distance of the leading prong to the top of the detector, and removing events where the leading shower has a greatest likelihood of being a muon. The distributions of these variables at the FD are shown in fig. 6.9 and Table 6.13 summarizes the cosmic rejection with the values used for the actual cuts. Table ?? lists the event rates before and after the cosmic rejection cuts are applied, and fig. ?? shows the energy distributions of events that pass these cuts.

6.6 Summary

The final selection combines all of the cuts from the previous sections. The event rates at each level of cut are summarized for the FD in Table 6.14, and in Table 6.15 for the ND. The final energy spectra are shown in fig. 6.10.

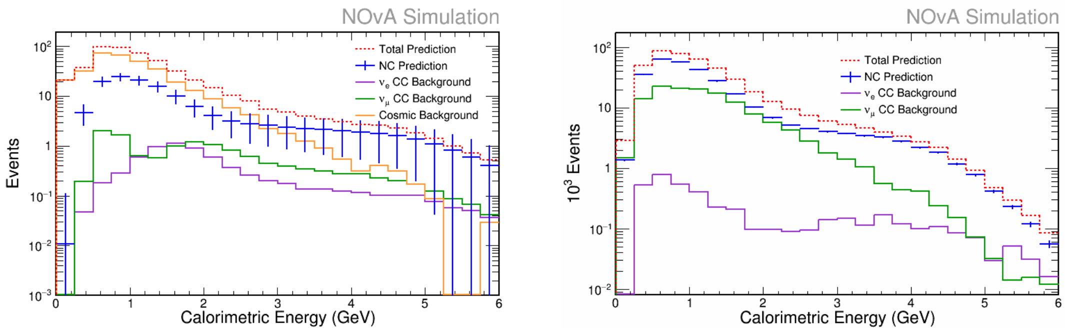

Figure 6.8: Energy spectra after NC selection cuts for the FD (left) and ND (right).

Table 6.13: The number of events after each cut level at the FD.

Cut Level	NC	ν_μ CC	ν_e CC	Cosmic
FD:				
...NC Selection	132.9	12.8	6.7	339.0
+ Cosmic Rejection	73.1	6.3	4.3	6.0
ND ($\times 10^3$):				
...NC Selection 296.9	136.0	4.2		
+ Cosmic Rejection	235.9	88.1	3.4	

Table 6.14: The number of events after each cut level at the FD.

Cut Level	NC	ν_μ CC	ν_e CC	Cosmic
Data Quality	363.1	298.1	65.0	14.40 $\times 10^6$
+ Event Quality	226.6	121.7	59.7	175900
+ Fiducial	142.2	49.2	37.2	13550
+ Containment	139.5	44.9	36.5	2295
+ NC Selection	132.9	12.8	6.7	339.0
+ Cosmic Rejection	73.1	6.3	4.3	6.0

Table 6.15: The number of events after each cut level at the ND.

Cut Level	NC	ν_μ CC	ν_e CC
Data Quality	12260	86703	1085
+Event Quality	7518	45752	658
+ Fiducial	619.3	1437.1	30.8
+ Containment	343.6	382.0	15.4
+ NC Selection 296.9	136.0	4.2	
+ Cosmic Rejection	235.9	88.1	3.4

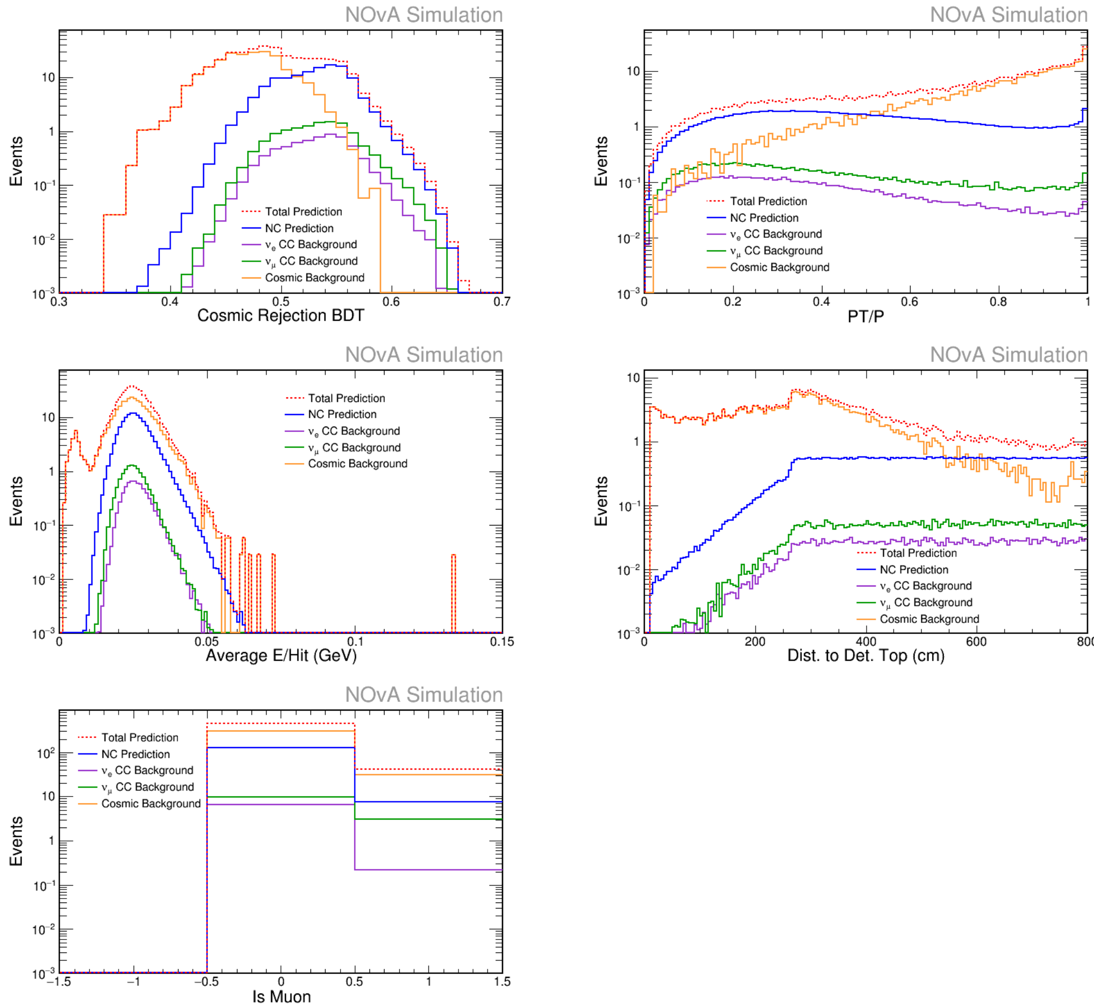

Figure 6.9: Distributions of variables used for cosmic rejection at the FD.

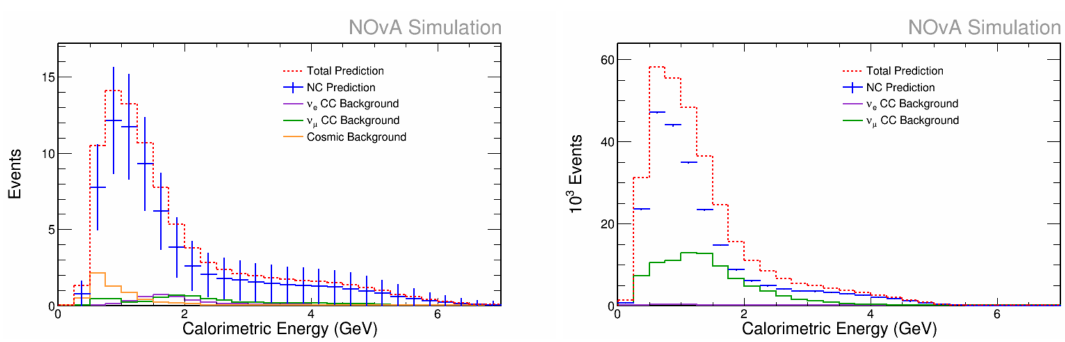

Figure 6.10: Energy spectra after all cuts for the FD (left) and ND (right).

7

Neutral Current Spectrum Prediction

Any rigorous scientific analysis must have a well defined analysis procedure. This chapter describes the bulk of that procedure for the FD NC disappearance analysis. The methods presented use the NC event selection discussed in ch. 6 to predict the FD energy spectrum.

7.1 The CAFAna Analysis Chain

The analysis presented in this thesis was performed in a software framework called CAFAna that analyzes Common Analysis Format files, or CAFs. The design principles of CAFAna recognize that all neutrino analyses have to perform essentially the same tasks, such as decomposing a detector spectrum into different components or applying oscillation weights to a particular event spectrum. A given task might have multiple implementations, but while the inner details are different, the number and type of end products are the same. Thus CAFAna has a fixed general analysis chain with the ability to easily swap specific implementations of any given piece of the chain.

The general analysis chain shown in fig. TODO illustrates how a near to far detector analysis can be neatly separated into smaller components that can be implemented individually. The first three components, IDecomp, IExtrap, and IPrediction, are responsible for the creation of a predicted FD spectrum. Each of these classes are pure virtual and simply declare the necessary functions for each class to hook into the next. The remainder of this chapter discusses these three classes in more detail; the classes that follow in the analysis chain are for the fitting and final results and are described in ch. 9.

Before delving into the analysis classes, it is worth briefly mentioning the basic unit of CAFAna, the Spectrum. The primary use of this class is to store the histogram of a specific variable and two methods of normalization, POT and livetime. Nearly every analysis class handles Spectrum objects in some fashion, be it storing them for internal calculations, returning them as output, or both. While the Spectrum has the ability to handle two dimensional histograms on its own, the specialized class OscillatableSpectrum stores a two dimensional histogram of a user defined variable on its X axis, and true neutrino energy on its Y axis. The function OscillatableSpectrum::Oscillated applies oscillation weights to all of the stored histogram's rows based on the true energy, then returns a one dimensional Spectrum by summing all of the contents in a column, projecting out the true energy axis.

7.2 Near Detector Decomposition

Near detector decomposition is performed within implementations of IDecomp. The output of any decomposition is simply a set of ND spectra separated by neutrino flavor and sign; thus IDecomp declares a set of functions that each return a Spectrum object with the same X axis and contain estimates of the NC, ν_μ, $\bar{\nu}_\mu$, ν_e, and $\bar{\nu}_e$ components. Since oscillations do not necessarily affect neutrinos and antineutrinos equally, a split by sign must happen at some point; it was a design choice to have that occur starting with the decomposition. The most basic implementation of IDecomp, named CheatDecomp, simply fills component histograms based on MC truth information. Fig. TODO shows the inheritance structure for all of the decompositions discussed in this section.

The decomposition used for the main analysis was ProportionalDecomp, which split each bin in data based on the proportion of each event type found in the MC. Fig. TODO shows the ND decomposition based on this method. Other decompositions were used for systematic studies, including NCDecomp, NumuDecomp, NueDecomp100Up, and NueDecomp100Dn. NCDecomp and NumuDecomp assess any data/MC difference to a single component. For NCDecomp, the ν_μ, $\bar{\nu}_\mu$, ν_e, and $\bar{\nu}_e$ components are taken directly from MC, and the difference between the sum of these components and the total data Spectrum is taken as the NC component. For NumuDecomp, it is the NC, ν_e, and $\bar{\nu}_e$ components that are taken from MC. NueDecomp100Up and NueDecomp100Dn split the data proportionally as in ProportionalDecomp, but then fluctuate the ν_e and $\bar{\nu}_e$ components up by 100% (doubling this background) or down by 100% (removing it), respectively.

7.3 Extrapolation

Near to far detector extrapolation occurs within implementations of IExtrap.

7.4 Far Detector Prediction

Oscillation weights are applied within implementations of IPrediction.

8

Systematic Error Analysis

As with any analysis, the NC disappearance analysis is sensitive to a number of systematic effects. NOνA was designed with two functionally identical detectors, so that Near Detector data can be used to constrain or correct the Far Detector prediction. Since many effects such as beam and cross section uncertainties affect the spectra at both detectors in a similar or the same way, this two detector technique leads to the reduction of these systematic errors. Other effects, such as Near Detector rock event contamination, require a data driven technique to quantify.

The general technique for analyzing systematic errors was to run the full extrapolation chain and generate a predicted spectrum with and without a systematic effect applied. As in ch. 6, the prediction assumed the same three flavor oscillation parameters listed in Table 6.1, and for normalization simplicity, only 14 diblock MC and data were studied. All spectra were then scaled to 6×10^{20} POT. Each given systematic effect was used to shift the MC simulation at one or both detectors as appropriate. The resulting difference between the shifted and nominal spectra was quantified as a systematic error.

The systematic effects analyzed included uncertainties arising from the beam, GENIE simulation, Birks-Chou light yield simulation, calibration, bias from the ND containment, ND rock event contamination, ND data/MC spectrum and hadronic energy differences, noise model, MC statistics, and overall normalization. The rest of this chapter discusses each of these effects in greater detail.

8.1 Beam

The NOνA MC simulation involves a fully detailed model of the NuMI beam process in an attempt to create the most realistic MC possible, but systematic errors can result from any mismatch between simulation and reality. The NOνA Beam Working Group performed studies to assess the effect that uncertainties in the simulation can have on the neutrino flux [57]. These studies included the effects of incorrectly modeling various parts of the beam transport and the effects of uncertainties in hadron production arising from fixed target experiments.

To quantify the systematic error caused by these beam uncertainties, a sample flux was generated using a systematic shift and compared to the nominal flux via a simple ratio. Results were generated separately for each neutrino flavor and for each detector. The ratios were used to modify the MC from the full simulation used as inputs to the extrapolated prediction. Finally, the shifted FD prediction was compared to the nominal prediction, with any differences being taken as the systematic error. At the end of this process, the individual errors were added in quadrature. Errors were calculated for the following systematics:

- Beam position on target varied by $\pm 0.5\,mm$ in X
- Beam position on target varied by $\pm 0.5\,mm$ in Y
- Beam spot size varied by $\pm 0.2\,mm$ in both X and Y
- Target position varied by $+2\,mm$ in Z
- Horn current varied $\pm 1\,kA$
- Horn 1 position varied by $\pm 2\,mm$ in both X and Y
- Horn 2 position varied by $\pm 2\,mm$ in both X and Y

- Horn magnetic field changed from linear to exponential distribution
- Changes to MC beamline simulation
- Comparison between versions of FLUKA
- Comparison between FLUKA and G4NuMI
- Comparison between FLUKA and NA49

Hadron production uncertainties were combined in quadrature before being provided as weights, so this is evaluated as single systematic error. The percentage difference due to each systematic is shown in Table 8.1, and the full error envelopes for NC signal and background are shown in Fig. 8.1. The beam systematics had an overall effect of 3.4% on the NC signal and 3.6% on the background.

Table 8.1: The percentage difference between the shifted and nominal predictions for the number of FD events due to beam systematics.

Systematic	NC Difference (%)	Background Difference (%)
Beam Position, X	0.5	0.4
Beam Position, Y	0.2	0.2
Beam Spot Size	0.2	0.3
Target Position	0.04	0.1
Horn Current	0.1	0.1
Horn 1 Position	0.6	0.8
Horn 2 Position	0.2	0.2
Horn B Field	0.05	0.05
Geometry Simulation Change	0.4	1.2
FLUKA Versions	0.04	0.4
FLUKA v G4NuMI	0.4	1.2
FLUKA v NA49	3.0	2.6
Combined	3.4	3.6

8.2 Birks-Chou Light Yield Simulation

The NOνA MC simulation employs the Birks-Chou Law to model the relationship between scintillator light yield, LY, and particle energy deposition rate, $\frac{dE}{dx}$ [58].

$$LY = A\frac{\frac{dE}{dx}}{1 + k_B\frac{dE}{dx} + k_C\left(\frac{dE}{dx}\right)^2} \tag{8.1}$$

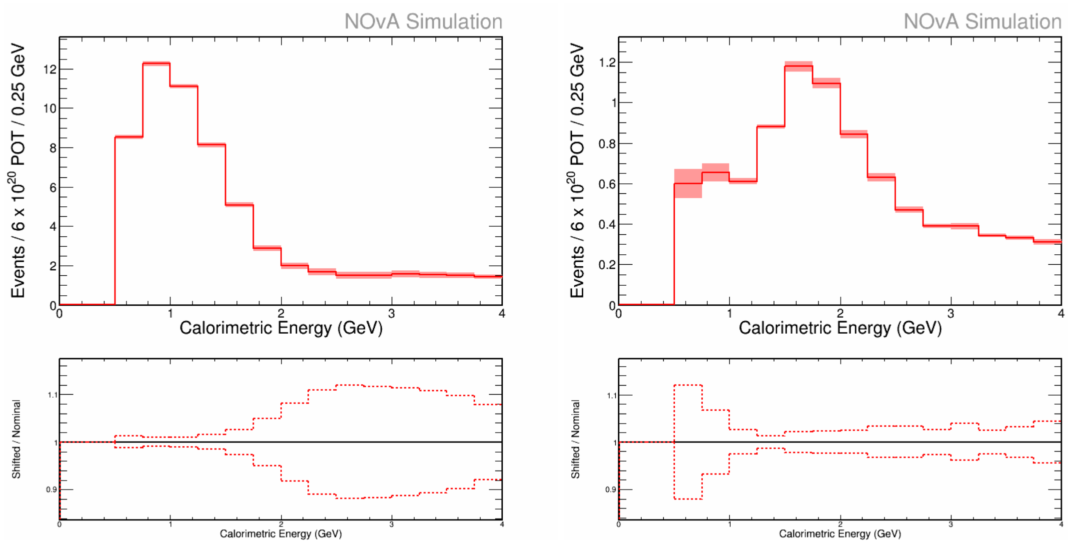

Figure 8.1: Beam systematics error envelope on the NC signal (left) and background (right) event spectra, after extrapolation. The envelope was calculated by adding in quadrature the larger of $|+1\sigma|$ and $|-1\sigma|$ for each individual systematic.

This formula encapsulates the known light yield quenching that occurs for particles with a high energy deposition rate. The constants k_B and k_C are dependent on the scintillator material and had to be estimated for NOνA as no measurement existed for the particular material used in this experiment. A study was performed comparing the energy deposition at the end of proton tracks in the ND for both data and MC to find parameters that would generate agreement between the two [59]. The results of the study were $k_B = 0.04$ cm/MeV and $k_C = -0.0005\,(\text{cm/MeV})^2$.

The systematic error based on the Birks-Chou light yield simulation was quantified by comparing the nominal FD prediction to predicted spectra using alternative Birks-Chou parameter constants. The values reported in the study from [59] were much larger than other typical measurements, so two MC samples were generated with more traditional values, one with $k_B = 0.01$ cm/MeV called BirksB, the other with $k_B = 0.02$ cm/MeV called BirksC, both with $k_C = 0$. Shifted FD event spectra were predicted by extrapolating the same set of ND data as the nominal prediction, but using the MC with alternative Birks-Chou model parameters. The error was taken as the percentage difference between the nominal and shifted predictions. Table 8.2 shows the percentage differences from both MC samples; fig. 8.2 shows the shifted event spectra compared to nominal. Instead of combining the individual errors in quadrature, the shifted sample with the larger overall difference from the BirksC model taken as the systematic error, which had a 2.4% effect on the NC signal, and a 1.8% effect on the background.

Table 8.2: The percentage difference between the shifted and nominal predictions for the number of FD events due to extrapolation using MC with alternative Birks-Chou model parameters.

Model	NC Difference (%)	Background Difference (%)
BirksB	0.5	1.2
BirksC	2.4	1.8

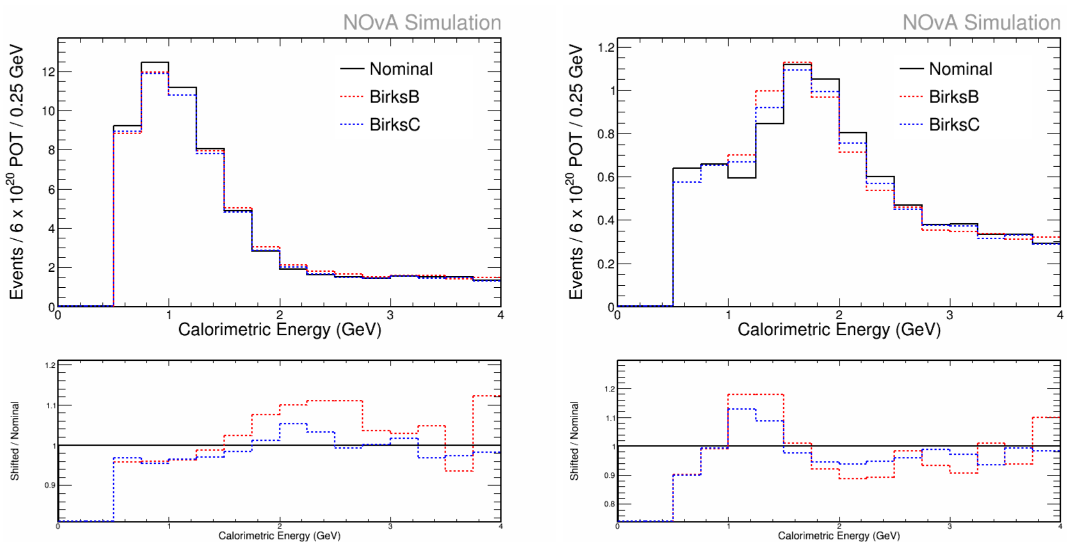

Figure 8.2: Shifted FD predictions due to extrapolation of ND data with MC using different Birks-Chou parameter values. The NC signal spectrum is on the left; the background spectrum is on the right.

8.3 Calibration

The calibration procedure is designed to make a constant energy response both across each detector and between the two, but any problem can introduce a systematic error. This error was evaluated by studying various MC samples with an engineered miscalibration. The effects studied included a miscalibration that varied as a function of the cell length and an overall scale miscalibration. The functional miscalibration was studied separately between the X and Y views of the detector. The scale miscalibration was applied as a 5% effect both up and down at each detector. These effects are motivated by studying data/MC comparisons for various samples [60, 61, 62] and were updated based on the most recent round of data [63].

The systematic error was evaluated in two regimes. The first applied the same miscalibration to the MC at both detectors, and a shifted prediction was then generated using these shifted as inputs into the extrapolation. This procedure was followed for each type of miscalibration, and all of these systematics were added in quadrature at the end. The overall scale miscalibration was also applied as a miscalibration to a single detector to measure the effect of a missed absolute calibration. A shifted prediction was then generated as above, but with this procedure only the maximum overall effect was used as the systematic error that was then added in quadrature with the systematics from above. Table 8.3 shows the percentage difference for each of the calibration systematics. The effects of the calibration systematics on the NC signal and CC background spectra are shown in fig.s 8.3 and 8.4 when applied to both detectors and one detector, respectively. The overall error was 5.8% on the NC signal and 6.0% on the background.

Table 8.3: The percentage difference between the shifted and nominal predictions for the number of FD events due to deliberately applied miscalibrations. For the flat scale miscalibration applied to 1 detector, the largest overall effect from the flat scale down at the ND was taken as the systematic.

Miscalibration	NC Difference (%)	Background Difference (%)
Miscalibration applied to both detectors:		
Sloped X	0.5	0.5
Sloped Y	1.6	1.1
Flat Scale Up	1.6	1.2
Flat Scale Down	3.5	2.3
Miscalibration applied to one detector:		
Flat Scale Up, ND	2.2	3.8
Flat Scale Down, ND	4.3	5.5
Flat Scale Up, FD	0.6	5.6
Flat Scale Down, FD	0.6	2.4

8.4 GENIE Simulation

Neutrino interactions in the NOνA simulation are generated using GENIE [64], a generator that involves a detailed physics modeling of cross sections, hadronization, and final state interactions. GENIE includes a plethora of parameters that alter individual physics input quantities, with the parameters themselves acting as systematic uncertainties, either dialing up or down a particular quantity by a stan-

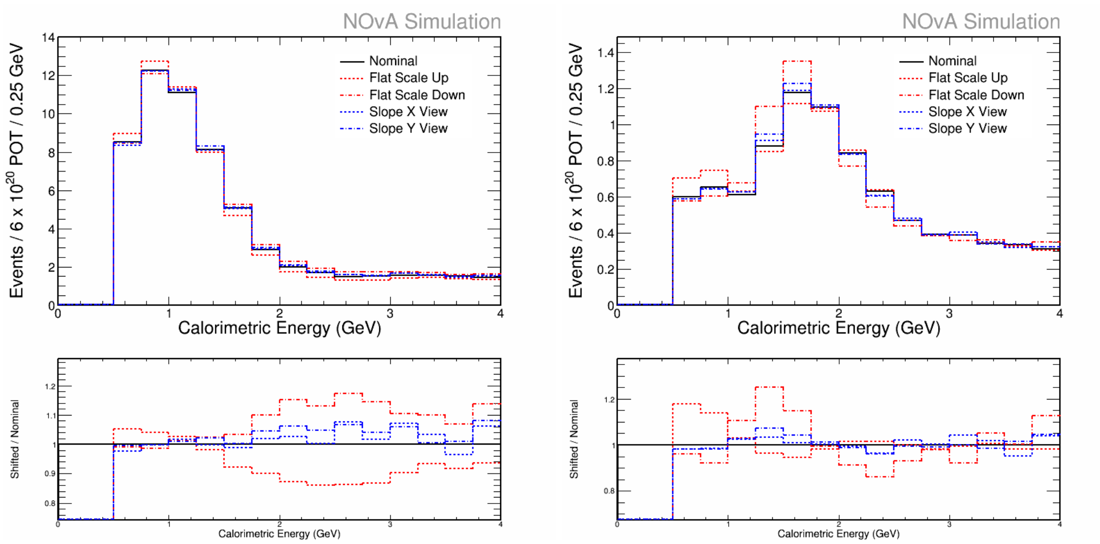

Figure 8.3: Shifted FD predictions due to miscalibration applied to both detector MC samples. The NC signal spectrum is on the left; the background spectrum is on the right.

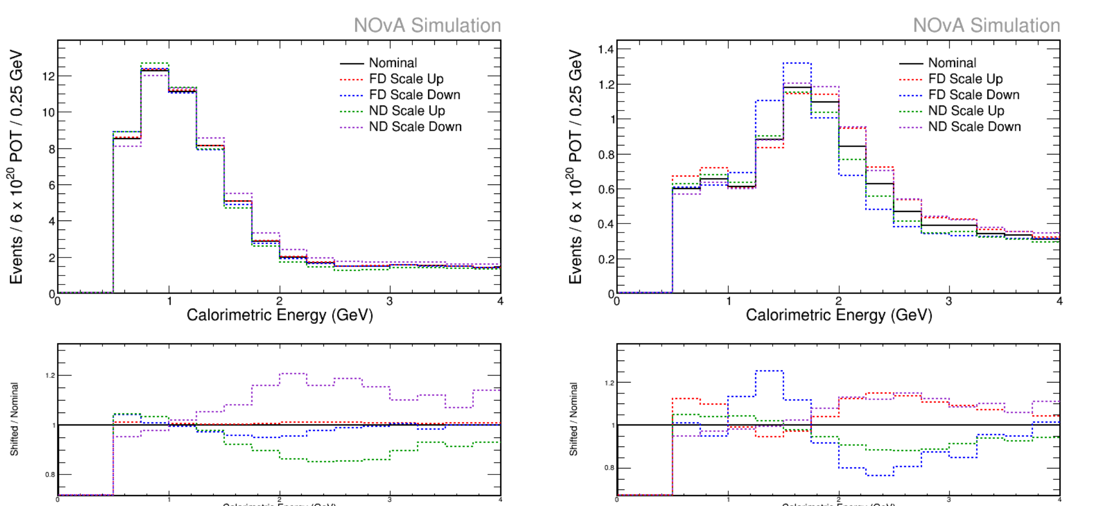

Figure 8.4: Shifted FD predictions due to miscalibration applied to one detector MC sample. The NC signal spectrum is on the left; the background spectrum is on the right.

dard deviation recommended by the GENIE authors.

The systematic uncertainties from physics modeling were evaluated by using the GENIE parameters as event reweights. Nominal MC was produced using the parameters and weights as provided by the GENIE authors, but also included a table of weights to modify an events 'worth' based on how much the different GENIE parameters shifted. Using the reweight table, a nominal FD prediction was produced from the default MC, and a shifted prediction was produced for each of the parameters provided by GENIE. The percentage difference was taken as the systematic error for the particular parameter. Table 8.4 lists all of the parameters considered for the systematic study, and the associated error. Fig. 8.5 shows the final systematic error envelope. The combined systematic error, adding the individual contributions in quadrature, was 1.6% for the NC signal and 4.8% for the background.

Table 8.4: The systematic error, in percentage difference, for each GENIE systematic parameter. The description and standard deviations come from ref. [64, 65]. Parameters with a standard deviation marked as 'D' are discrete and thus do not have a standard deviation estimate.

Parameter Description and Standard Deviation		NC Diff. (%)	Bkg. Diff. (%)
Axial mass for NC elastic	$\pm 25\%$	0.4	0.00
Strange axial form factor η for NC elastic	$\pm 30\%$	0.02	0.00
Normalization Factor for CCQE	$^{+25\%}_{-15\%}$	0.00	1.3
Axial mass CCQE distribution shape	$^{+25\%}_{-15\%}$	0.0	0.4
CCQE Pauli suppression (via changes in Fermi level k_F)	$\pm 35\%$	0.00	0.6
Choice of CCQE vector form factors (BBA05 $\leftrightarrow$ Dipole)	D	0.00	0.3
Axial mass for CC resonance neutrino production	$\pm 20\%$	0.00	2.2
Vector mass for CC resonance neutrino production	$\pm 10\%$	0.00	1.1
Axial mass for NC resonance neutrino production	$\pm 20\%$	0.7	0.00
Vector mass for NC resonance neutrino production	$\pm 10\%$	0.2	0.00
Axial mass for CC and NC coherent pion production	$\pm 50\%$	0.4	0.3
Nuclear size param controlling π absorption in RS model	$\pm 10\%$	0.4	0.3
Non-resonance bkg in νp CC1π reactions	$\pm 50\%$	0.00	0.4
Non-resonance bkg in νp CC2π reactions	$\pm 50\%$	0.00	0.9
Non-resonance bkg in νn CC1π reactions	$\pm 50\%$	0.00	1.9
Non-resonance bkg in νn CC2π reactions	$\pm 50\%$	0.00	0.9
Non-resonance bkg in νp NC1π reactions	$\pm 50\%$	0.2	0.00
Non-resonance bkg in νp NC2π reactions	$\pm 50\%$	0.2	0.00
Non-resonance bkg in νn NC1π reactions	$\pm 50\%$	0.2	0.00
Non-resonance bkg in νn NC2π reactions	$\pm 50\%$	0.1	0.00

Parameter Description and Standard Deviation		NC Diff. (%)	Bkg. Diff. (%)
Non-resonance bkg in $\bar{\nu}p$ CC1π reactions	$\pm 50\%$	0.00	0.1
Non-resonance bkg in $\bar{\nu}p$ CC2π reactions	$\pm 50\%$	0.00	0.02
Non-resonance bkg in $\bar{\nu}n$ CC1π reactions	$\pm 50\%$	0.00	0.01
Non-resonance bkg in $\bar{\nu}n$ CC2π reactions	$\pm 50\%$	0.00	0.02
Non-resonance bkg in $\bar{\nu}p$ NC1π reactions	$\pm 50\%$	0.02	0.00
Non-resonance bkg in $\bar{\nu}p$ NC2π reactions	$\pm 50\%$	0.02	0.00
Non-resonance bkg in $\bar{\nu}n$ NC1π reactions	$\pm 50\%$	0.02	0.00
Non-resonance bkg in $\bar{\nu}n$ NC2π reactions	$\pm 50\%$	0.02	0.00
A_{HT} higher-twist param in BY model scaling variable ξ_w	$\pm 25\%$	0.01	0.2
B_{HT} higher-twist param in BY model scaling variable ξ_w	$\pm 25\%$	0.02	0.3
C_{V1u} u valence GRV98 PDF correction param in BY model	$\pm 30\%$	0.02	0.1
C_{V2u} u valence GRV98 PDF correction param in BY model	$\pm 40\%$	0.01	0.1
Pion transverse momentum (p_T) for $N\pi$ states in AGKY	D	0.01	0.02
Pion Feynman x (x_F) for $N\pi$ states in AGKY	D	0.01	0.02
Pion angular distribution in $\Delta \to \pi N$ (isotropic $\leftrightarrow$ RS)	D	0.1	0.3
Branching ratio for radiative resonance decays	$\pm 50\%$	0.02	0.01
Branching ratio for single-η resonance decays	$\pm 50\%$	0.1	0.2
Nucelon mean free path (total rescattering probability)	$\pm 20\%$	0.2	0.4
Nucleon charge exchange probability	$\pm 50\%$	0.1	0.2
Nucleon elastic reaction probability	$\pm 30\%$	0.1	0.4
Nucleon inelastic reaction probability	$\pm 40\%$	0.1	0.2
Nucleon absorption probability	$\pm 20\%$	0.05	0.2
Nucleon π-production probability	$\pm 20\%$	0.04	0.1
π mean free path (total rescattering probability)	$\pm 20\%$	0.4	0.7
π charge exchange probability	$\pm 50\%$	0.1	0.2
π elastic reaction probability	$\pm 10\%$	0.1	0.1
π inelastic reaction probability	$\pm 40\%$	0.6	0.3
π absorption probability	$\pm 20\%$	0.6	0.4
π π-production probability	$\pm 20\%$	0.03	0.1
MEC event scale	$+50\%$	0.00	1.6
RPA event weight	Varied	0.00	1.1
Combined		1.6	4.8

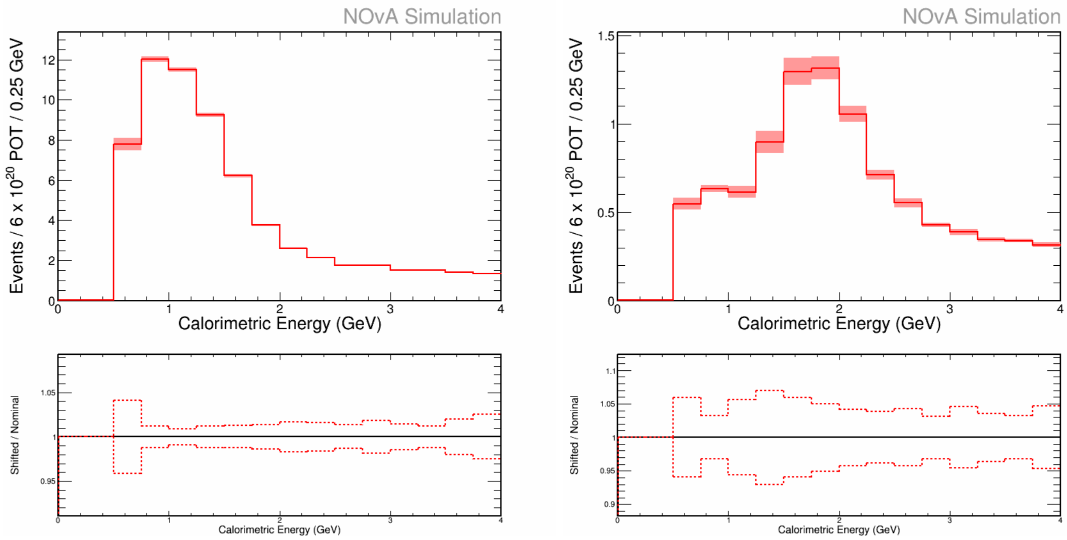

Figure 8.5: GENIE systematics error envelope on the NC signal (left) and background (right) event spectra, after extrapolation. The envelope was calculated by adding in quadrature the larger of $|+1\sigma|$ and $|-1\sigma|$ for each individual systematic.

8.5 ND Containment

The ND does not see an effective point source of neutrinos like the FD due to its proximity to the beam source. As a result, the neutrino flux is not uniform across the detector, and so the energy spectrum of neutrinos seen by the two NOνA detectors is slightly different. To study the effect this has on the extrapolated prediction, multiple predicted FD spectra were generated using subsamples of the ND. The fiducial volume of the ND was split in half along each axis, and split into an inner and outer half (the overall containment criteria was left in tact). The extrapolation was performed using each of these 'half detectors.' The error was taken as the percentage difference from the shifted prediction to the nominal. Table 8.5 shows the results from each of these extrapolations and fig. 8.6 show the shifted spectra. Like the Birks-Chou systematic, the largest overall difference was taken as the systematic error for a 1.0% effect on the NC signal and a 0.6% effect on the background.

8.6 ND Rock Event Contamination

The MC simulation does include neutrino interactions that occur in the rock that surrounds the ND. These events often leak into the detector volume, and while most of them are cut away by fiducial and

Table 8.5: The percentage difference between the shifted and nominal predictions for the number of FD events after extrapolation using half of the fiducial volume at the ND.

ND Half	NC Difference (%)	Background Difference (%)
West (+X)	0.3	0.01
East (-X)	0.2	0.1
Top (+Y)	0.3	0.01
Bottom (-Y)	0.3	0.01
Front (Low Z)	0.1	0.3
Back (High Z)	0.1	0.4
Inner (Low |X|, |Y|)	0.8	0.02
Outer (High |X|, |Y|)	1.0	0.6

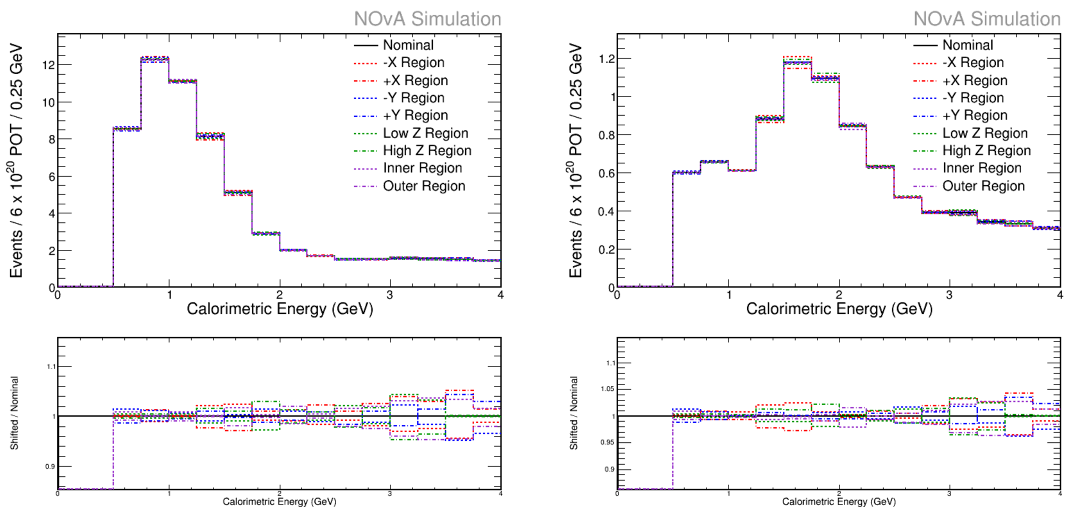

Figure 8.6: Shifted FD predictions after extrapolation using only half of the ND fiducial volume. The NC signal spectrum is on the left; the background spectrum is on the right.

containment cuts, there are some that remain. Those events that do remain cannot be reconstructed properly as their origins are outside of the detector.

The systematic error that is incurred due to the rock event contamination was estimated by predicting the FD event spectrum from an extrapolation with rock events removed by MC truth and comparing to the nominal predicted spectrum. The events were only removed from the ND MC sample, requiring that the true neutrino vertex was inside the detector to remain. The shifted spectra are shown in Fig. 8.7. This systematic amounted to an overall 4.1% shift on the NC signal spectrum and a 1.7% shift on the background spectrum.

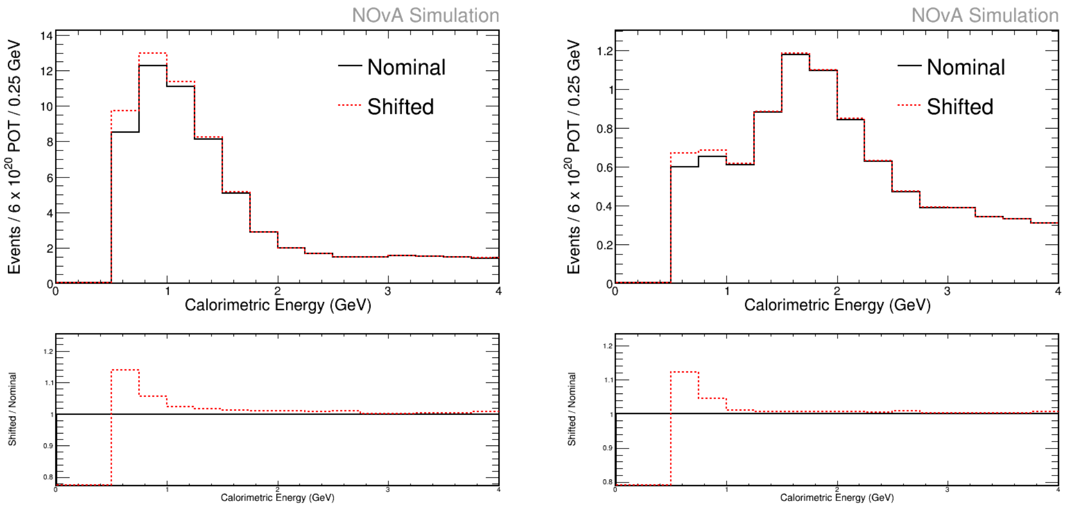

Figure 8.7: Shifted vs nominal spectra for the NC signal (left) and background (right). The shifted spectra are extrapolated after removal of rock events in the ND MC by truth.

8.7 ND Data/MC Difference and CC Background

To assess the results over the MC simulation, data was compared to MC at the ND, and the event spectra were found to be an imperfect match; see fig. 8.8. The FD prediction is made by decomposing ND data into NC, ν_μ CC and ν_e CC components proportional to the amounts in the MC, so a data/MC difference can cause a systematic effect. This error was treated as a hybrid decomposition and CC background error, and as such, was quantified using a hybrid method.

For the first NOνA ν_μ disappearance and ν_e appearance analyses, the two groups used different methods to estimate their background uncertainties. The ν_μ analysis noted that their backgrounds were small and thus placed a 100% uncertainty on each [43]. The ν_e analysis assigned any discrepancy between ND data and MC to each of the three ND background components, used each shifted decomposition to perform an extrapolation, compared the shifted predictions to nominal, and took the shift with the largest difference as the systematic error [42].

The NC disappearance analysis used a combination of the above techniques to evaluate the ND data/MC and CC background systematic error. The background from the beam ν_e component was calculated to be small, so this component was allowed to vary by $\pm 100\%$. The shifted spectrum was used for extrapolation, and the percentage difference between the nominal and shifted predictions was

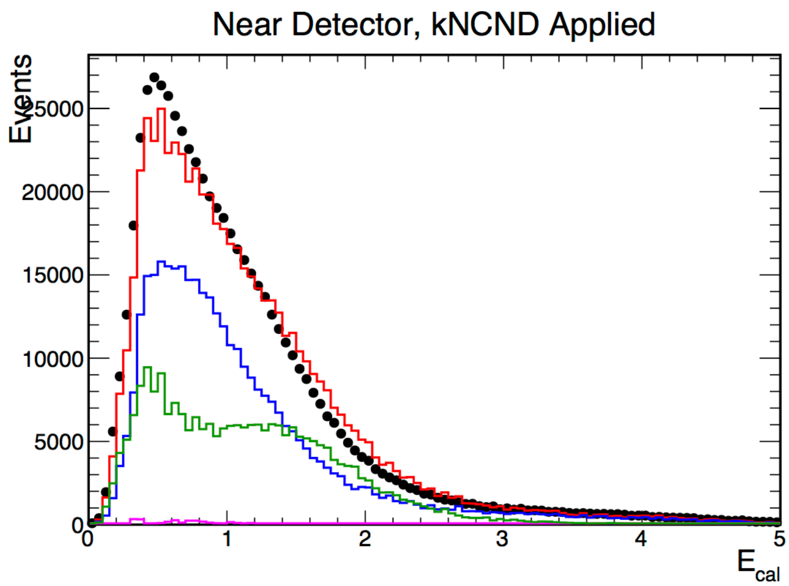

Figure 8.8: Energy spectra for data and MC at the ND, from ref. [66]

taken as the error. For both the NC and ν_μ CC components, the error was taken following the same procedure as the ν_e analysis. Results from both these two studies were then combined in quadrature. Shifting the beam ν_e component up and down produced the same net change in event numbers, albeit in opposite directions. Assigning the data/MC difference to the ν_μ CC component caused the larger overall difference, compared to assignment to the NC component. The overall error was thus calculated by combining in quadrature the errors from assigning the data/MC difference to the ν_μ CC component and shifting the beam ν_e component by $|100\%|$, for a result of a 7.0% effect on the NC signal and a 10.4% effect on the CC background. Table 8.6 summarizes the results from these studies, fig. 8.9 shows the shows the changes in the predicted spectrum due to each systematic shift.

8.8 MC Statistics

In a perfect world, there would be enough MC statistics that this section would be unnecessary, but alas, a perfect world this is not. To estimate the systematic error due to MC statistics, the MC was split into five uniformly sized samples, and each was used to extrapolate the same set of ND data. One of the resultant predicted FD spectra was labeled as nominal, and the other four were compared to this. The

Table 8.6: Systematic error covering ND data/MC discrepancy and CC backgrounds. The percentage differences were calculated by shifting the ND decomposition using the listed error method, performing an extrapolation, and comparing the predicted results to nominal.

Error Method	NC Difference (%)	Background Difference (%)
Beam ν_e $+100\%$	0.00	8.2
Beam ν_e -100%	0.00	8.2
ND Data/MC difference assigned to NC component	5.2	7.7
ND Data/MC difference assigned to ν_μ CC component	7.0	6.4
Overall	7.0	10.4

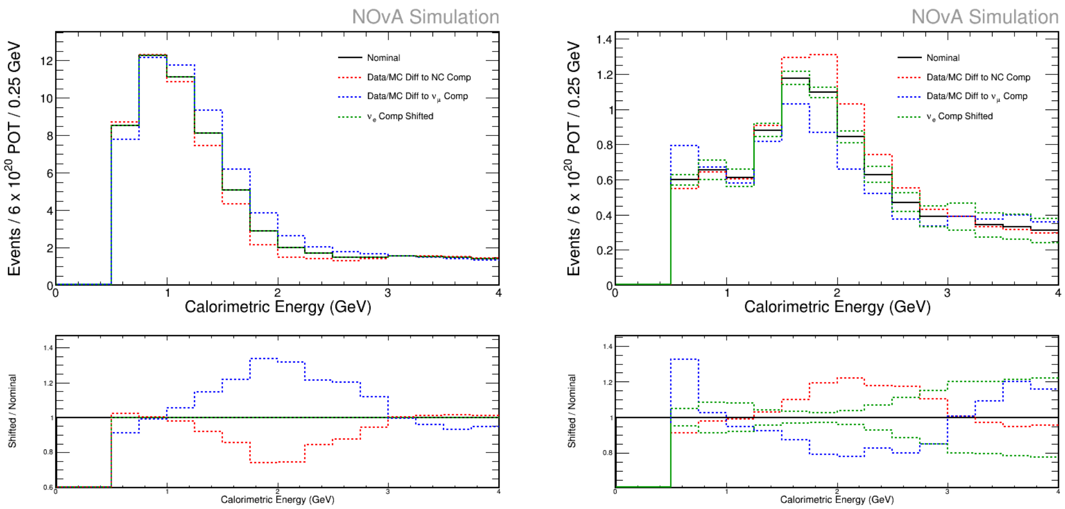

Figure 8.9: Shifted FD predictions from studies to quantify ND data/MC difference and CC background uncertainties.

bin by bin differences were taken as the error between the nominal spectrum and the 'shifted' spectrum. To come up with an overall uncertainty, all of the errors were added in quadrature and the result was divided by the square root of the number of samples, or $\sqrt{4} = 2$. The result was a 2.0% error on the NC signal spectrum and a 4.8% error on the background spectrum.

8.9 Noise Model

A sample of MC was generated for the FD using a different model of noise to study the systematic error caused by the noise model. To quantify the error, the predicted FD event spectra from the nominal and alternative MC samples were compared against each other after applying normal three flavor oscillation weights. The difference seen was 0.9% for the NC signal, and 0.7% for the background. As the shifted sample was only generated for the FD MC and the error was comparatively small, this systematic was added into the overall normalization.

8.10 Overall Normalization

Several independent effects contributed to an overall normalization systematic error. A 0.5% error on the POT counting came from a small difference in the two toroids that determine the POT in a spill [57]. Uncertainties in the masses of the various parts of the NOνA detectors contributed another error of 0.7% [67]. Finally, a study of the reconstruction efficiency between ND data and MC showed a 2.9% difference between the number of events that get fully reconstructed [68], which was taken directly as a contribution to the normalization error. These three effects and the noise systematic were combined in quadrature and constituted a systematic error of 3.2% on the NC signal and 3.1% on the background.

8.11 Systematic Error Summary

Table 8.7 shows a summary of all of the systematics, as well as an overall error. The overall error was calculated by summing the error from each row in quadrature. The final systematic error on the NC signal is 11.6% and the error on the background is 14.8%.

All of the systematics discussed to this point were also calculated at the ND. Many of these, including the Beam, Birks-Chou, and GENIE, are much larger without mitigation through extrapolation. The combined effects were studied to be certain that any data/MC discrepancy was covered under the full ND systematic error band. The data/MC spectra are shown in Fig. 8.10. Note that the systematic error that assesses any data/MC difference to a single component does not contribute to the full band. The technique used for this systematic did not change the total number of events since both the nominal and shifted spectra respected the normalization from the data. As the systematic error band was calculated using all events, by construction this data driven systematic effect does not have an effect on the total error band.

Table 8.7: A summary of the individual systematic errors for the NC disappearance analysis. The errors are percentage differences between the nominal and shifted predicted spectra.

Systematic	NC Difference (%)	Background Difference (%)
Beam	3.4	3.6
Birks-Chou	2.4	1.8
Calibration	5.8	6.0
GENIE	1.6	4.8
ND Containment	1.0	0.6
ND Rock Contamination	4.1	1.7
ND Data/MC	7.0	10.4
MC Statistics	2.0	4.8
Overall Normalization	3.2	3.1
Combined	11.6	14.8

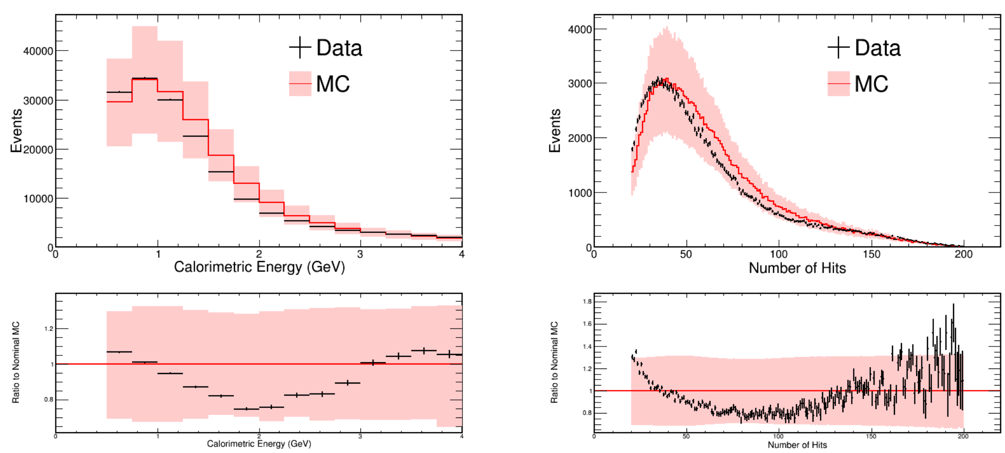

Figure 8.10: ND Data/MC spectra with full systematic error band. The calorimetric energy spectrum is shown on the left, the number of hits spectrum is shown on the right.

9

Analysis Results

The analysis presented in this dissertation was designed to make several measurements. As this dissertation was written alongside the first NOνA NC analysis, one primary goal of the analysis was to demonstrate the successful ability of NOνA to identify NC events and measure the ratio of observed to predicted NC events in a 3 flavor hypothesis, R_{NC}.

$$R_{NC} \equiv \frac{N_{Obs} - N_{Pred}^{Bkg}}{N_{Pred}^{NC}} \tag{9.1}$$

The other (arguably more important) goal was to start contributing to the global data on the sterile mixing parameters by extracting measurements on the mixing angles θ_{24}, θ_{34} and matrix elements $|U_{\mu 4}|^2$ and $|U_{\tau 4}|^2$.

Results in this chapter were collected between February 2014 and May 2016. For the FD, this corresponds to 6.69×10^{20} POT, or 6.05×10^{20} full detector equivalent POT. For the ND, 3.71×10^{20} POT was collected.

The first section in this chapter describes the fitting methods used to make the mixing angle and matrix element measurements. Before presenting the results, the next two sections discuss preliminary tests to demonstrate satisfactory performance of the analysis. The final section in this chapter presents the ultimate results.

9.1 Fitting Method

It was decided to make rate only measurements for the first NOνA NC disappearance analysis. Thus, even though the extrapolation and prediction were performed in 250 MeV bins of calorimetric energy, only the integrated event totals were input to the fitting framework.

Fitting was performed allowing some parameters to float, some held to best fit values, and others set to 0 due to insensitivity. As mentioned above, a major analysis goal was to measure θ_{24} and θ_{34}, so these angles were allowed to float between $0°$ and $45°$. Values outside of this range are either equivalent to this range through redefinition of the angles, or already highly disfavored through previous experiments and in a region difficult for fitting due to many local minima. θ_{23} was allowed to float with a Gaussian constraint with mean $45.8°$ and standard deviation $3.2°$, the best fit measurement by T2K [69]. All of the remaining parameters were held fixed to the values listed in table 9.1.

Table 9.1: The parameters held fixed and the values they were set at for fitting.

Parameter	Value
Δm^2_{21}	$7.53 \times [10^{-5}\,\mathrm{eV}^2]$
Δm^2_{32}	$2.37 \times [10^{-3}\,\mathrm{eV}^2]$
$\sin^2 2\theta_{12}$	0.846
$\sin^2 2\theta_{13}$	0.085
θ_{14}	0
δ_{13}	0
δ_{24}	0
δ_{14}	0

The best fit values were found by calculating the minimum χ^2 value and allowing individual systematics to float with a penalty,

$$\chi^2 = 2\left(N_{Pred} - N_{Obs} + N_{Obs}\ln\frac{N_{Obs}}{N_{Pred}}\right) + \left(\frac{\theta_{23} - \mu_{23}}{\sigma_{23}}\right)^2 + \sum_{i=1}^{N}\left(\frac{\sigma_i^{BF}}{\sigma_i}\right)^2, \qquad (9.2)$$

where μ_{23} and σ_{23} are the mean and standard deviation used in the Gaussian constraint on the value of θ_{23}, σ_i^{BF} is the number of standard deviations the ith systematic error is shifted in the best fit, and σ_i is one standard deviation for the ith systematic error. Eq. 9.2 is the standard formula for calculating χ^2 with penalty terms, where the first term is the basic value for χ^2, and the second and third terms add a unit for each shift of θ_{23} and the systematic errors by their respective variances. For one and two dimensional χ^2 surfaces, the remaining angles not shown were profiled.

9.2 ND Data/MC Comparisons

Before diving head first into the FD data, the first necessary analysis benchmark was ND data/MC comparisons. Fig 9.1 shows the event energy distributions and fig.s 9.2, 9.3, and 9.4 show the distributions for all of the variables used for selection discussed in ch. 6.
While most of the distributions differ by at most a small normalization, a few have an apparent shift, notably the energy and number of hits distributions. These particular discrepancies were actually expected due to a known mismodeling of NC interactions.

Very recently there was experimental evidence for a new 'mode' of interaction. A systematic scale for this event type was added to and evaluated with the GENIE systematics discussed in sec. 8.4. The inclusion of these effects drastically improved the data/MC agreement for the NOνA CC analyses. Unfortunately, while the experimental data was available allowing for study of these effects on CC events, the data for NC events is largely nonexistent. Consequently the NOνA simulation does not include these effects for NC events despite widespread belief that similar effects should be seen. This would largely explain the data/MC differences seen in the energy and number of hits distributions.

Two sanity checks were performed to ensure that the data/MC difference would not negatively impact the analysis. First, the ND data/MC energy distribution was shown with a full systematic error

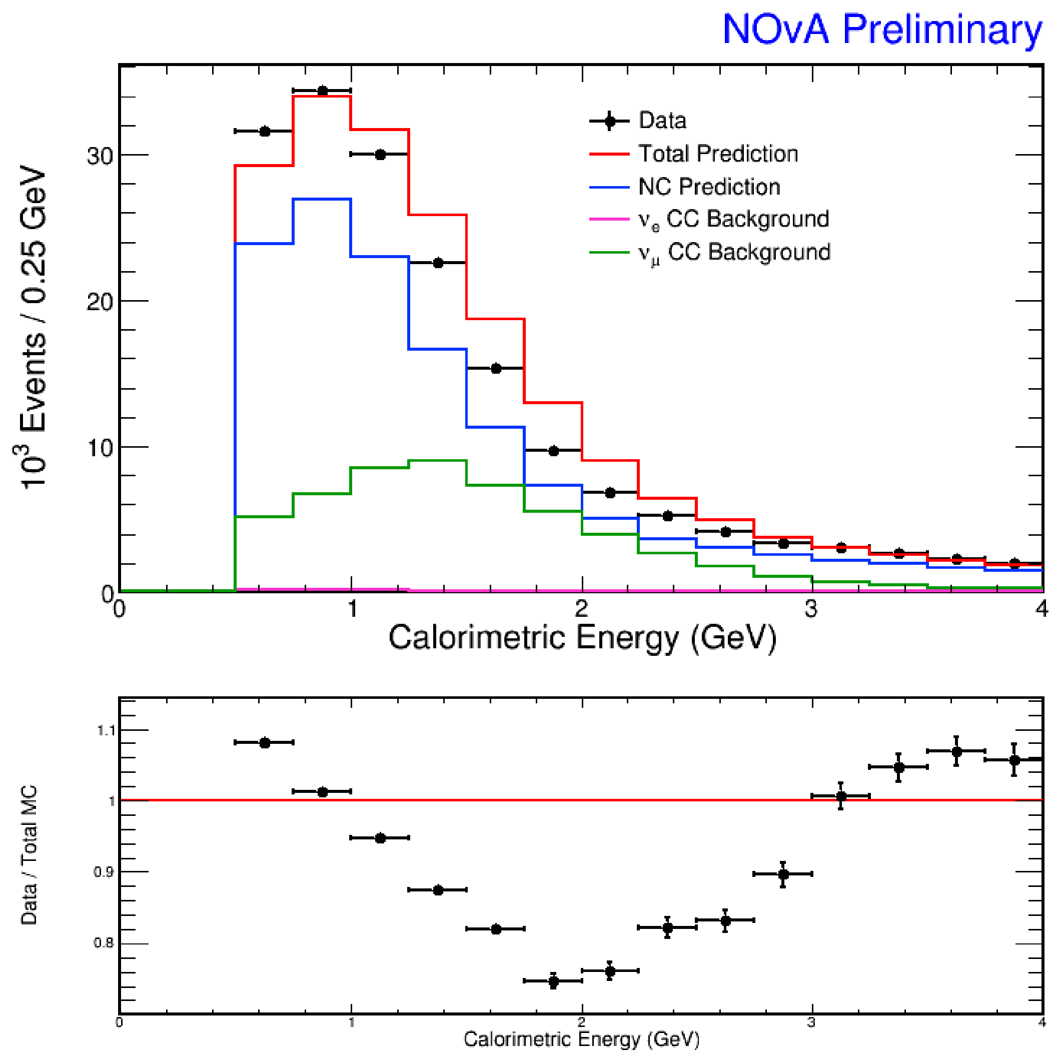

Figure 9.1: ND data/MC comparison of the calorimetric energy.

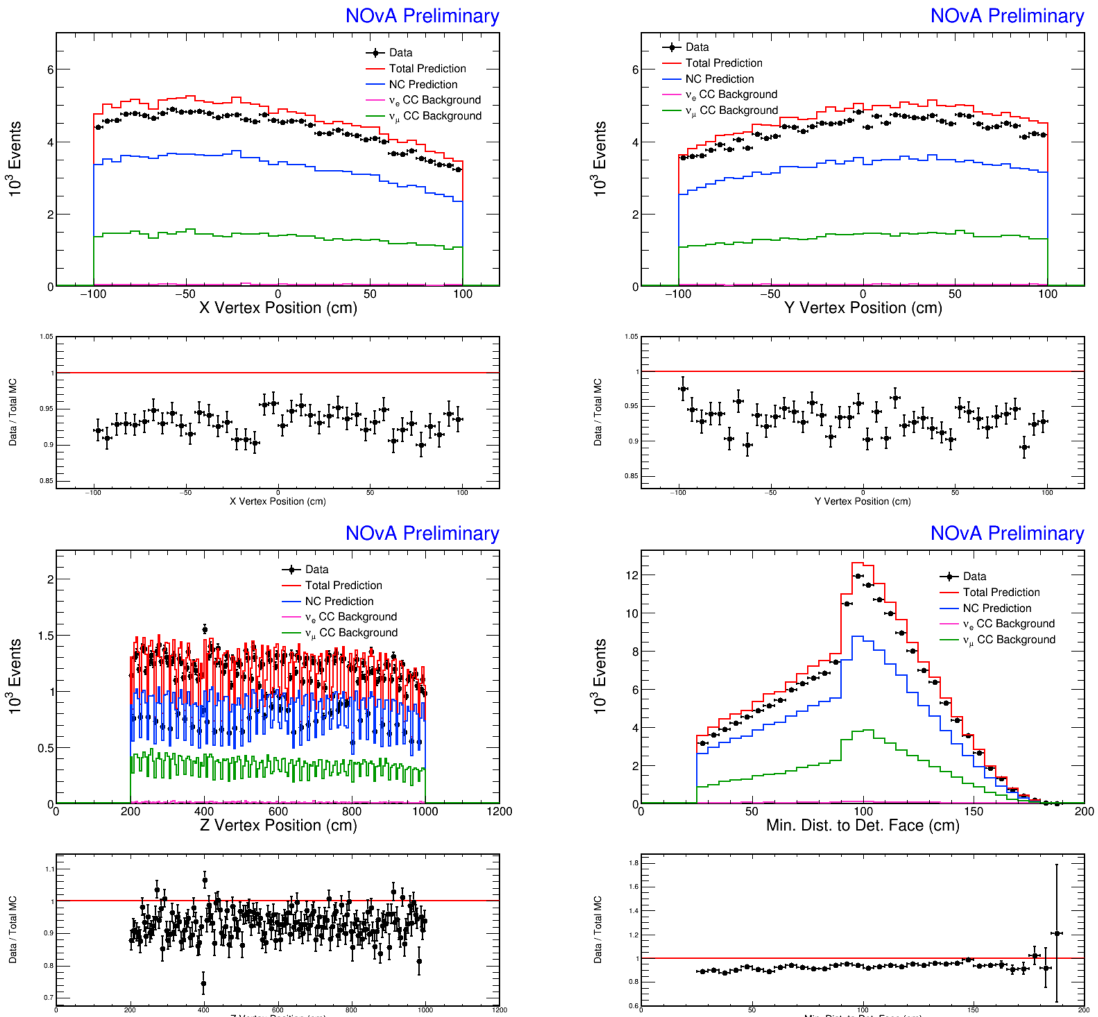

Figure 9.2: ND data/MC comparison of the reconstructed vertex position and containment distributions.

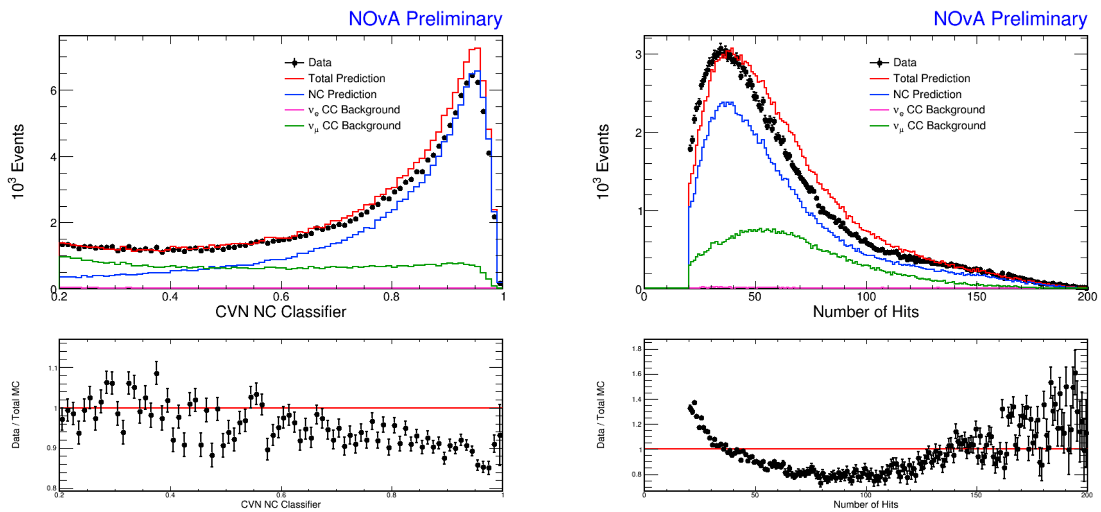

Figure 9.3: ND data/MC comparison of the CVN and number of hits distributions.

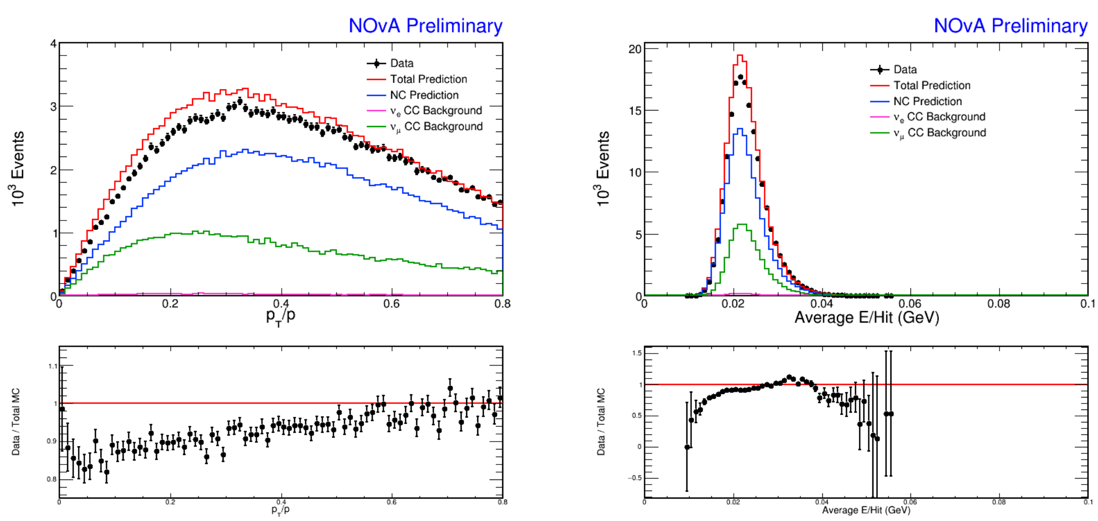

Figure 9.4: ND data/MC comparison of particle transverse momentum and energy per hit distributions.

band to show the difference is covered by systematics. This was shown in fig. 8.10. Secondly, the effect of shifting either the data or MC in relation to the other on the predicted event rate and 1D angle sensitivities was studied. This was done by shifting the data up or the MC down by the ratio of the means of the energy distributions for MC and data, $1.39\,\text{GeV}/1.33\,\text{GeV} \approx 4.5\%$ and also for a much larger shift of 10%. The event counts are shown in Table 9.2 and the angle sensitivities are shown in fig. 9.5. Due to the nature of a counting experiment, since the overall event rates are essentially unchanged, the effect of these rather large shifts is negligible. As a result, it was decided to take the data and MC as is and push for model improvements for future analyses.

Table 9.2: The number of predicted events at the FD after applying an energy shift to data or MC.

Shift	All	NC	ν_μ CC	ν_e CC	Cosmic	FOM
Nominal	83.5	60.6	4.6	3.6	14.3	6.633
Data 4.5% Up	84.6	61.0	4.7	3.7	14.9	6.634
Data 10% Up	86.2	61.4	4.9	3.7	15.8	6.612
MC 4.5% Down	85.1	61.8	4.8	3.7	14.3	6.702
MC 10% Down	87.2	63.4	5.2	3.8	14.3	6.792

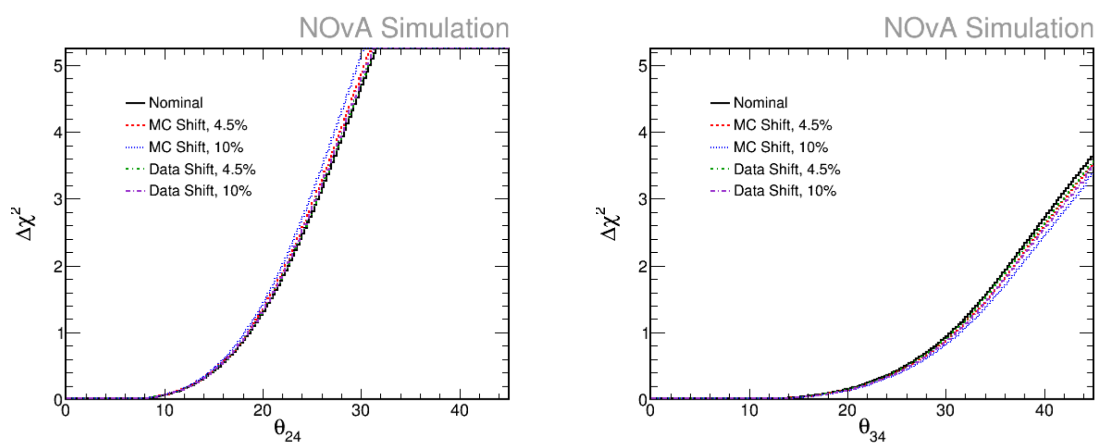

Figure 9.5: Angle sensitivities after applying an energy shift to either MC or data. Left: θ_{24}, Right: θ_{34}. The fits are statistics only and do not include any systematic errors.

9.3 Sideband Studies

Three different sidebands were studied to test the performance of the analysis, a high energy sideband, a low CVN sideband, and mid cosmic BDT sideband. The predicted and observed event rates for each sideband are shown in Table 9.3.

Table 9.3: The observed and predicted events at the FD for each sideband.

Sideband	Data	Total MC	NC	ν_μ CC	ν_e CC	Cosmic
High Energy	15	8.2	6.5	0.8	0.5	0.1
Low CVN	35	32.7	3.7	5.5	19.3	4.0
Mid BDT	17	14.5	6.0	0.5	0.4	7.5

The high energy sideband applied the standard selection and considered events between 4 and 6 GeV, a region chosen due to its high purity of NC events. The predicted and observed event distributions are shown in fig. 9.6, 8.2 events were predicted and 15 ± 4 were observed in data. While the observed rate is slightly high, the low statistics means that the observation is within 2σ of the prediction. Furthermore, the discrepancy is largely driven by a single bin rather than a systematic offset. This result was thus interpreted as validation for the general analysis procedure.

The low CVN sideband considered events that fail the CVN cut, or those with a CVN NC score below 0.2. This region was used as validation for the CVN selector. The predicted and observed event distributions are shown in fig. 9.7, 32.7 events were predicted and 35 ± 6 were observed in data. The overall agreement in both shape and rate for this sideband provided great confidence in the performance of CVN.

The mid cosmic BDT sideband considers events with a BDT score between 0.42 and 0.5, a region which fails the standard selection cuts but still has NC events. The predicted and observed event distributions are shown in fig. 9.8, 14.5 events were predicted and 17 ± 4 were observed in data. This sideband also showed excellent agreement in both shape and rate, providing further validation for the general analysis procedure, and specifically for the main cosmic rejection variable.

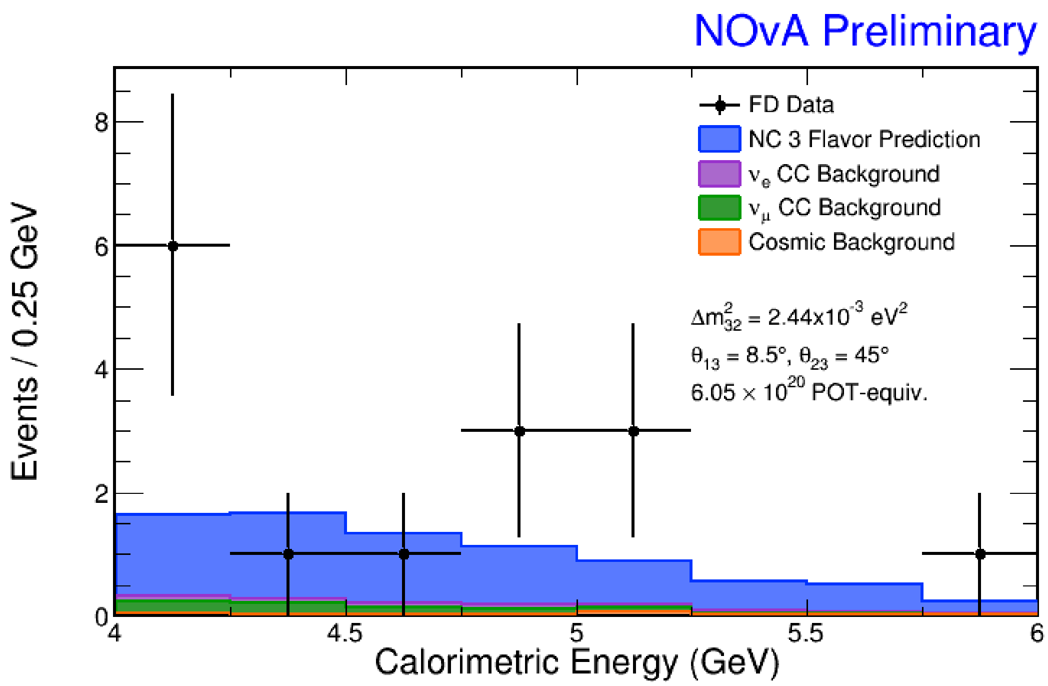

Figure 9.6: The observed and predicted FD event rates for the high energy sideband.

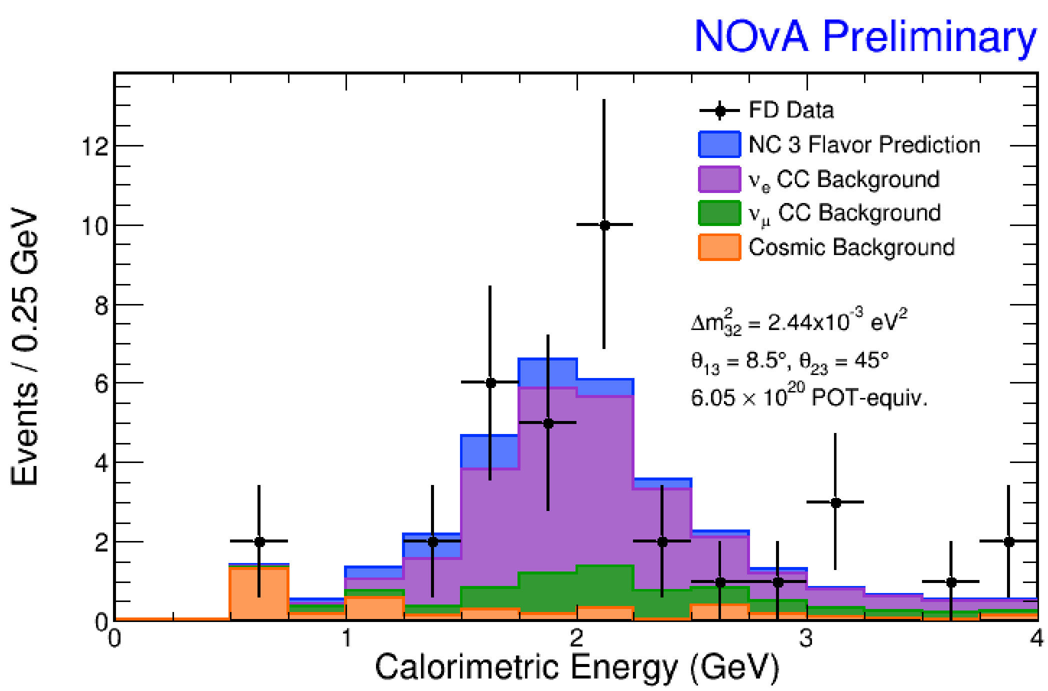

Figure 9.7: The observed and predicted FD event rates for the low CVN sideband.

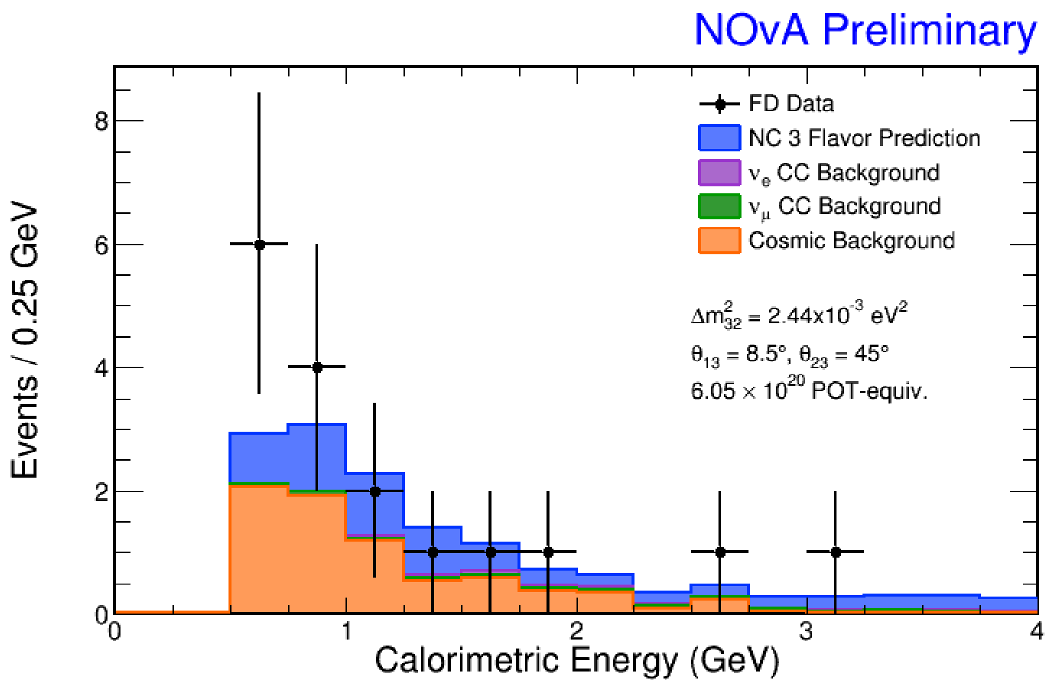

Figure 9.8: The observed and predicted FD event rates for the mid cosmic BDT sideband.

9.4 Results

This analysis predicted that there would be $83.8 \pm a.b(\text{stat.})^{+c.d}_{-e.f}(\text{syst.})$ NC-like events selected in the FD data. 95 ± 9.7 were observed, corresponding to a measurement of $R_{NC} = 1.186 \pm 0.161(\text{stat.})^{+0.081}_{-0.129}(\text{syst.})$ If active neutrinos mixed with sterile neutrinos, the number of observed events would be depleted, causing R_{NC} to be less than one. Thus, the measurement of R_{NC} is consistent with the no sterile mixing hypothesis.

The energy distribution of the predicted and observed events is shown in fig. 9.9. The χ^2 of this distribution is 23.31 for 14 bins, or 1.665/bin. To better assess the understanding of the observed data, data/MC comparisons distributions were studied for many of the variables used for selection, including regions cut for the analysis. These can be seen in fig.s 9.10, 9.11, and 9.12.

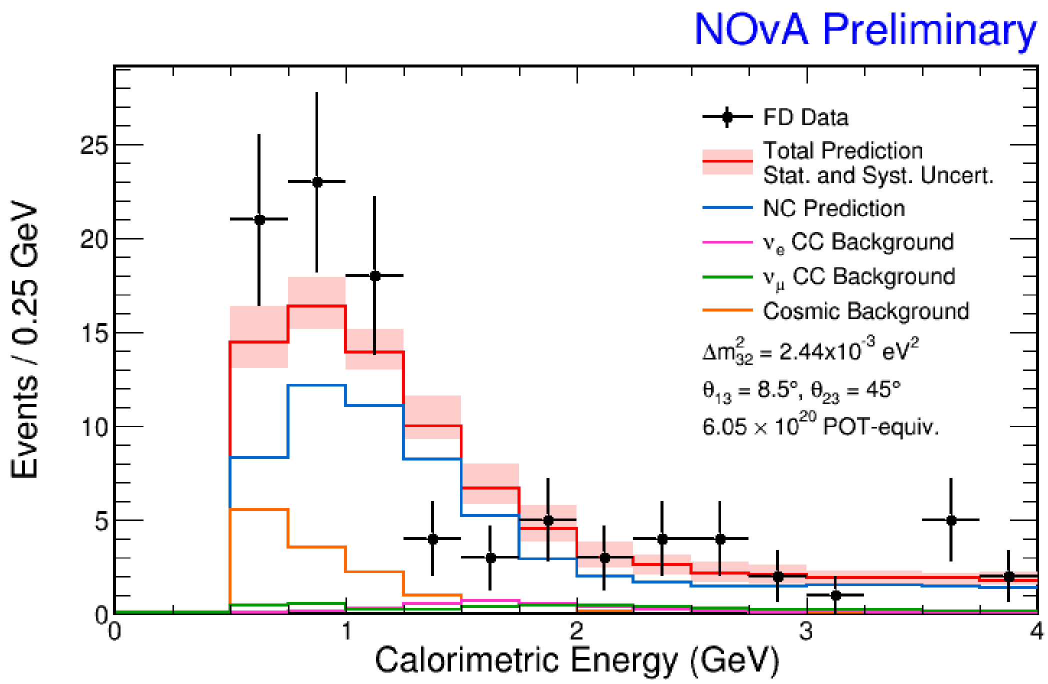

Figure 9.9: Calorimetric energy distribution of events predicted and observed in the FD.

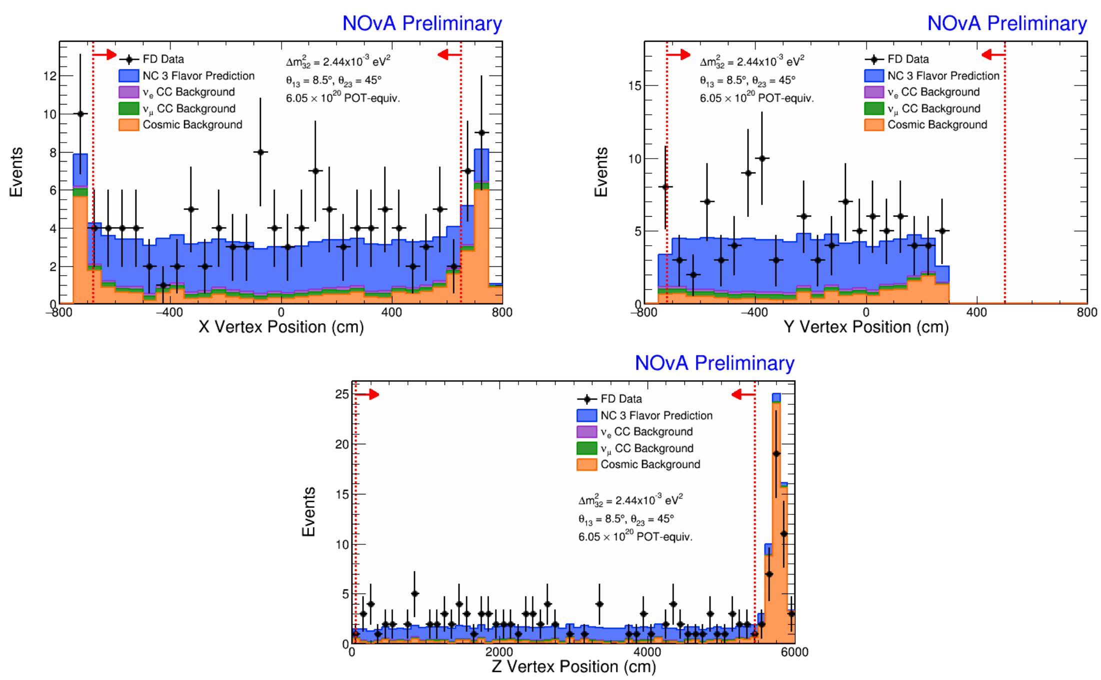

Figure 9.10: FD data/MC comparison of the reconstructed vertex position distributions. The dashed lines and arrows indicate the regions kept for the analysis.

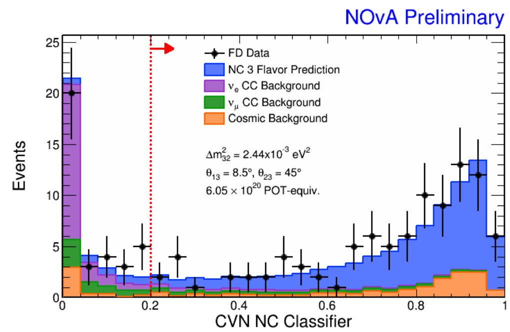

Figure 9.11: FD data/MC comparison of the CVN distribution. The dashed line and arrow indicate the region kept for the analysis.

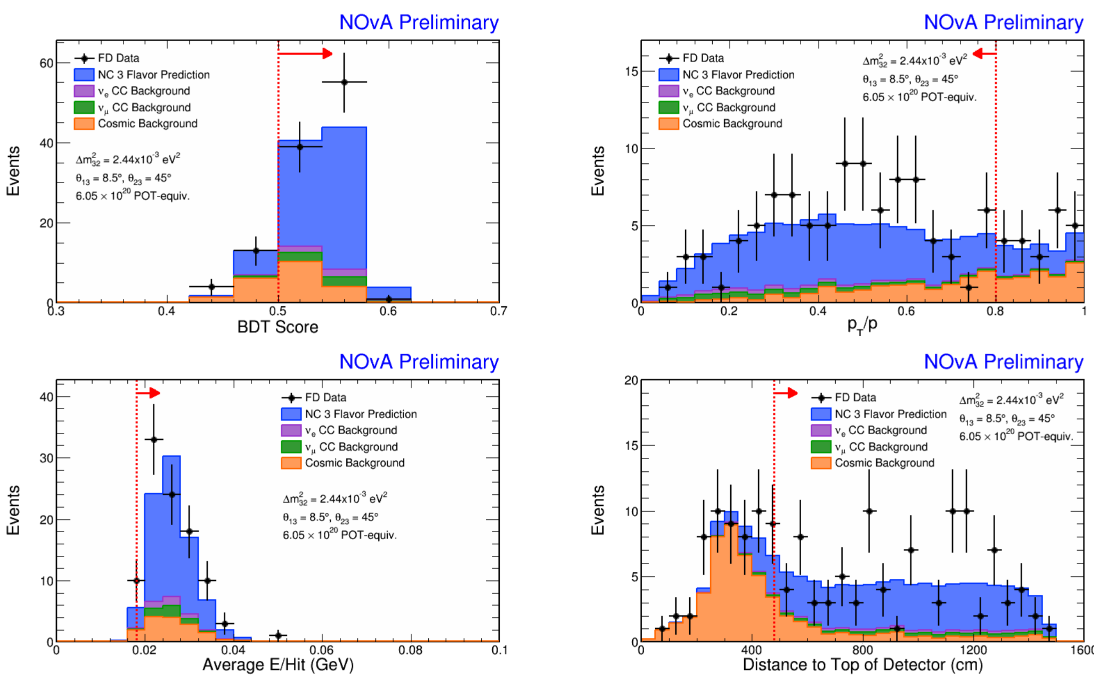

Figure 9.12: FD data/MC comparisons of the variables used for cosmic rejection. The dashed lines and arrows indicate the regions kept for the analysis.

10
Conclusions and Future Improvements

10.1 Conclusions

The results of this analysis are consistent with no sterile neutrinos.

10.2 Future Improvements

References

[1] W. Pauli. Letter to a physicists' gathering at tubingen, 1930.

[2] J. Chadwick. Possible existence of a neutron. *Nature*, 192:312, 1932.

[3] E. Fermi. Versuch einer theorie der β-strahlen. *Zeitschrift für Physik*, 88:161–177, 1934.

[4] F. Reines and C. L. Cowan. Detection of the free neutrino. *Physical Review*, 92:830–831, 1953.

[5] C. L. Cowan, F. Reines, F. B. Harrison, H. W. Kruse, and A. D. McGuire. Detection of the free neutrino: A confirmation. *Science*, 124:103–104, 1956.

[6] G. Danby et al. Observation of high-energy neutrino reactions and the existence of two kinds of neutrinos. *Physical Review Letters*, 9:36–44, 1962.

[7] DONUT Collaboration, K. Kodama et al. Observation of tau neutrino interactions. *Physics Letters B*, 504:218–224, 2001.

[8] B. Pontecorvo. Mesonium and anti-mesonium. *Soviet Journal of Experimental and Theoretical Physics*, 6:429, 1957.

[9] R. Davis, Jr., D. S. Harmer, and K. C. Hoffman. Search for neutrinos from the sun. *Physical Review Letters*, 20:1205–1209, 1968.

[10] J. N. Bahcall, N. A. Bahcall, and G. Shaviv. Present status of the theoretical predictions for the ^{37}Cl solar-neutrino experiment. *Physical Review Letters*, 20:1209–1212, 1968.

[11] V. Gribov and B. Pontecorvo. Neutrino astronomy and lepton charge. *Physics Letters B*, 28:493–496, 1969.

[12] K.S. Hirata et al. Observation of B-8 solar neutrinos in the Kamiokande-II detector. *Physical Review Letters*, 63:16–19, 1989.

[13] A. I. Abazov et al. Search for neutrinos from the sun using the reaction ^{71}Ga (ν_e, e^-) ^{71}Ge. *Physical Review Letters*, 67:3332–3335, 1991.

[14] P. Anselmann et al. Solar neutrinos observed by GALLEX at Gran Sasso. *Physics Letters B*, 285:376–389, 1992.

[15] K.S. Hirata et al. Observation of a small atmospheric ν_μ/ν_e ratio in Kamiokande. *Physical Letters B*, 280:146–152, 1992.

[16] Y. Fukuda et al. Evidence for oscillation of atmospheric neutrinos. *Physical Review Letters*, 81:1562–1567, 1998.

[17] Q. R. Ahmad et al. Direct evidence for neutrino flavor transformation from neutral-current interactions in the sudbury neutrino observatory. *Physical Review Letters*, 89:011301, 2002.

[18] ALEPH Collaboration, DELPHI Collaboration, L3 Collaboration, OPAL Collaboration, SID Collaboration, LEP Electroweak Working Group, SID Electroweak Group, Heavy Flavour Group. Precision electroweak measurements on the Z resonance. *Physics Reports*, 427:218–224, 2006.

[19] C. Athanassopoulos et al. Candidate events in a search for anti-muon-neutrino –> anti-electron-neutrino oscillations. *Physical Review Letters*, 75:2650–2653, 1995.

[20] A. A. Aguilar-Arevalo et al. A search for electron neutrino appearance at the $\Delta m^2 \sim 1$ eV^2 scale. *Physical Review Letters*, 98:231801, 2007.

[21] A. A. Aguilar-Arevalo et al. Improved search for $\bar{\nu}_\mu \rightarrow \bar{\nu}_e$ oscillations in the MiniBooNE experiment. *Physical Review Letters*, 110:161801, 2013.

[22] B. Armbruster et al. Upper limits for neutrino oscillations $\bar{\nu}_\mu \rightarrow \bar{\nu}_e$ from muon decay at rest. *Physical Review D*, 65:112001, 2002.

[23] P. Astier et al. Search for $\nu_\mu \rightarrow \nu_e$ oscillations in the NOMAD experiment. *Physics Letters B*, 570:19–31, 2003.

[24] F. Kaether et al. Reanalysis of the GALLEX solar neutrino flux and source experiments. *Physics Letters B*, 685:47–54, 2010.

[25] J. Abdurashitov et al. Measurement of the response of a Ga solar neutrino experiment to neutrinos from an ^{37}Ar source. *Physical Review C*, 73:045805, 2006.

[26] B. Achkar et al. Search for neutrino oscillations at 15, 40 and 95 meters from a nuclear power reactor at bugey. *Nuclear Physics B*, 434:503–532, 1995.

[27] J. Ahn et al. Observation of reactor electron antineutrino disappearance in the reno experiment. *Physical Review Letters*, 108:191802, 2012.

[28] F. P. An et al. Search for a light sterile neutrino at Daya Bay. *Physical Review Letters*, 113:141802, 2014.

[29] K. Abe et al. Limits on sterile neutrino mixing using atmospheric neutrinos in Super-Kamiokande. *Physical Review D*, 91:052019, 2015.

[30] P. Adamson et al. Active to sterile neutrino mixing limits from neutral-current interactions in minos. *Physical Review Letters*, 107:011802, 2011.

[31] Z. Maki, M. Nakagawa, and S. Sakata. Remarks on the unified model of elementary particles. *Progress of Theoretical Physics*, 28:870–880, 1962.

[32] J. Rich. Quantum mechanics of neutrino oscillations. *Physical Review D*, 48:4318–4325, 1993.

[33] B. Kayser. On the quantum mechanics of neutrino oscillation. *Physical Review D*, 24:110–116, 1981.

[34] K. A. Olive et al. Review of particle physics. *Chinese Physics C*, 38:090001, 2014.

[35] O. Mena and S. Parke. Unified graphical summary of neutrino mixing parameters. *Physical Review D*, 69:117301, 2004.

[36] E. Niner. *Observation of Electron Neutrino Appearance in the NuMI Beam with the NOνA Experiment*. PhD thesis, Indiana University, 2015.

[37] L. Wolfenstein. Neutrino oscillations in matter. *Physical Review D*, 17:2369–2374, 1978.

[38] S. P. Mikheev and A. Y. Smirnov. Resonance enhancement of oscillations in matter and solar neutrino spectroscopy. *Soviet Journal of Nuclear Physics*, 42:913–917, 1985.

[39] H. Nunokawa, S. Parke, and J. W. F. Valle. CP violation and neutrino oscillations. *Progress in Particle and Nuclear Physics*, 60:338–402, 2008.

[40] F. P. An et al. Observation of electron-antineutrino disappearance at Daya Bay. *Physical Review Letters*, 108:171803, 2012.

[41] F. Capozzi et al. Status of three-neutrino oscillation parameters, circa 2013. *Physical Review D*, 89:093018, 2014.

[42] P. Adamson et al. First measurement of electron-neutrino appearance in NOvA. *Physical Review Letters*, 2016.

[43] P. Adamson et al. First measurement of muon-neutrino disappearance in NOvA. *Physical Review D Rapid Communications*, 93:051104, 2016.

[44] P. A. R. Ade et al. Planck 2015 results. XIII. Cosmological parameters. arXiv:1502.01589 [astro-ph.CO].

[45] J. Kopp, P. A. N. Machado, M. Maltoni, and T. Schwetz. Sterile neutrino oscillations: The global picture. *Journal of High Energy Physics*, 2013:050, 2013.

[46] A. Palazzo. Estimate of θ_{14} independent of the reactor antineutrino flux determinations. *Physical Review D*, 85:077301, 2012.

[47] L. Goodenough and S. R. Phan-Budd. Technical note on the NOvA beam monitoring for 2015 summer analysis. NOνA Internal Document 13572.

[48] X. Bu and K. Sachdev. Spill level data quality- technical note. NOνA Internal Document 12437.

[49] K. Bays. Livegeometry tech note. NOνA Internal Document 11470.

[50] S. Lein. DCM edge metric. NOνA Internal Document 13527.

[51] C. Backhouse et al. Near detector data/MC comparisons for the nue analysis. NOνA Internal Document 13587.

[52] J. Bian and T. Xin. Note of selection cuts for Nue first analysis. NOνA Internal Document 13592.

[53] K. Bays et al. Executive summary for the first numu CC analysis. NOνA Internal Document 13641.

[54] N. J. Raddatz. ReMID technical note. NOνA Internal Document 11206.

[55] K. Sachdev, J. Bian, and E. Niner. Likelihood based nue identifier (lid). NOνA Internal Document 13590.

[56] K. Bays. Cosmic rejection technical note. NOνA Internal Document 11205.

[57] H. Duyang et al. A technote describing the derivation and size of NuMI flux uncertainties used in the second NOvA analyses. NOνA Internal Document 15296.

[58] C. N. Chou. The nature of the saturation effect of fluorescent scintillators. *Physical Review*, 87:904–905, 1952.

[59] D. Pershey. Birks-chou parameter selection. NOνA Internal Document 13158.

[60] L. Vinton. First analysis calibration technotes. NOνA Internal Document 13579.

[61] D. Pershey. ME check with SA rock muons in ND. NOνA Internal Document 14959.

[62] G. Davies. pi0 invariant mass in SA files. NOνA Internal Document 15005.

[63] K. Matera et al. Calibration status for second analysis. NOνA Internal Document 15127.

[64] C. Andreopoulos et al. The GENIE neutrino monte carlo generator: Physics and user manual. http://arxiv.org/abs/1510.05494.

[65] H. Gallagher et al. GENIE tune and uncertainty band for second analysis. NOνA Internal Document 15214.

[66] A. Markowitz. Data MC comparison for NC analysis, updated with SA files. NOνA Internal Document 15151.

[67] N. Raddatz. Fiducial mass systematic. NOνA Internal Document 13237.

[68] A. Markowitz. Reconstruction efficiency study summary. NOνA Internal Document 15447.

[69] K. Abe et al. Measurement of neutrino oscillation in appearance and disappearance channels by the T2K experiment with 6.6×10^{20} protons on target. *Physical Review D*, 91:072010, 2015.